VILNIUS UNIVERSITY

Mindaugas
MORKŪNAS

Development of Tumor Microenvironment-Oriented Digital Pathology Methods for Whole Slide Image Segmentation and Classification

DOCTORAL DISSERTATION

Technological Sciences
Informatics Engineering (T 007)

VILNIUS 2021

This dissertation was written between 2016 and 2020 at Vilnius University.

Academic supervisor:
Assoc. Prof. Dr. Povilas Treigys (Vilnius University, Technological Sciences, Informatics Engineering – T 007).

Academic consultant:
Prof. Dr. Arvydas Laurinavičius (Vilnius University, Medicine and Health Sciences, Medicine – M 001).

VILNIAUS UNIVERSITETAS

Mindaugas
MORKŪNAS

Naviko Mikroaplinkai Pritaikytų Pilno Kadro Vaizdo Segmentavimo ir Klasifikavimo Skaitmeninės Patologijos Metodų Kūrimas

DAKTARO DISERTACIJA

Technologijos mokslai
Informatikos inžinerija (T 007)

VILNIUS 2021

3

Disertacija rengta 2016–2020 metais Vilniaus universitete.

Mokslinis vadovas:
doc. dr. Povilas Treigys (Vilniaus universitetas, technologijos mokslai, informatikos inžinerija – T 007).
Mokslinis konsultantas:
prof. dr. Arvydas Laurinavičius (Vilniaus universitetas, medicinos ir sveikatos mokslai, medicina – M 001).

ABSTRACT

To better serve cancer patients, diagnostic and digital pathology methods focus on more novel targets. One of such targets is the tumor microenvironment. The increasing significance of the tumor microenvironment in cancer biology has caused a major shift of cancer treatment and research from a tumor-centric model to a tumor microenvironment-centric one. However, machine vision-dependent digital pathology methods are still very tumor cell-centric and largely ignore the tumor microenvironment. This work has set the aim to investigate and propose new histopathology image segmentation and classification methods by targeting tumor microenvironment-related histologic tissue components. Firstly, convolutional neural networks were identified as a group of state-of-the-art methods of sufficient capacity to handle multiple histologic object segmentation. Then, the existing tumor cell segmentation method was adapted and extended for lymphocyte segmentation and identification. Next, fibrous collagen was identified as a novel tumor microenvironment-borne target for segmentation in bright-field images of tumorous tissue. To address the collagen fiber segmentation task, a fully convolutional neural network-based approach was developed. Finally, an approach integrating knowledge gained in previous experiments was proposed enabling segmentation of lymphocytes, tumor cell nuclei, stromal cell nuclei, collagen fibers, and major tissue compartments. Additionally, by the engineering of image features, a whole slide image transformation was introduced, enabling the prediction of therapeutic biomarker status for individual breast cancer patients from complete tumor tissue whole-slide images. Proposed methods were extensively tested in an experimental setup on private in-house annotated histologic image datasets and public datasets and a competition challenge. The proposed methods were comparable to the state-of-the-art methods while at the same time providing special additional features.

SANTRAUKA

Siekiant didesnės naudos onkologiniams pacientams sukurti diagnostiniai ir skaitmeniniai patologijos metodai, daug dėmesio skiriantys naujiems tyrimo taikiniams. Vienas iš tokių taikinių yra naviko mikroaplinka. Ryškėjanti naviko mikroaplinkos svarba vėžio biologijoje lemia akivaizdų vėžio gydymo ir tyrimų posūkį nuo naviko ląstelėms pritaikyto link naviko mikroaplinkai pritaikyto modelio. Tačiau nuo kompiuterinės regos priklausomi skaitmeninės patologijos metodai vis dar yra stipriai orientuoti į naviko ląsteles ir iš esmės ignoruoja naviko mikroaplinką. Šiame darbe užsibrėžtas tikslas ištirti ir pasiūlyti naujus histopatologijos vaizdo segmentavimo ir klasifikavimo metodus, skirtus su naviko mikroaplinka susijusiems histologiniams audinių komponentams. Pirma, konvoliuciniai neuroniniai tinklai identifikuoti kaip pažangiausių metodų, pakankamai pajėgių daugeliui histologinių objektų segmentuoti, grupė. Tada limfocitams segmentuoti ir identifikuoti pritaikytas ir išplėstas esamas naviko ląstelių segmentavimo metodas. Toliau skaidulinis kolagenas identifikuotas kaip naujas iš naviko mikroaplinkos atsirandantis taikinys, kurį galima segmentuoti naviko audinių šviesinės mikroskopijos vaizduose. Kolageno skaidulų segmentavimo užduočiai spręsti sukurtas visiškai konvoliucinis neuroninių tinklų metodas. Galiausiai pasiūlytas integruotas metodas, sujungiantis ankstesniuose eksperimentuose įgytas žinias ir leidžiantis segmentuoti limfocitų, naviko ląstelių, stromos ląstelių branduolius, kolageno skaidulas ir pagrindinius audinių tipus. Be to, vaizdo požymių inžinerijos būdu įvestas patologijos pilno kadro vaizdo transformavimas, pritaikytas nuspėti krūties vėžiu sergančių pacientų terapinio biožymens būseną. Siūlomi metodai išbandyti eksperimentais, naudojant tiek privačius, tiek viešus anotuotų histologinių vaizdų duomenų rinkinius bei tarptautinio iššūkio varžybose. Siūlomi metodai buvo sulyginami su susijusiais pažangiausiais metodais, tuo pat metu suteikdami papildomų specialių funkcionalumų.

List of Abbreviations

AE	Autoencoder
ANN	Artificial Neural Network
AUC	Area Under the Receiver Operating Characteristic Curve
CNN	Convolutional Neural Networks
CSM	Collagen Segmentation Map
DL	Deep Learning
ECM	Extracellular Matrix
FA	Factor Analysis
FCNN	Fully Convolutional Neural Networks
GT	Ground Truth
H&E	Hematoxylin and Eosin
HOG	Histogram of Oriented Gradients
IM	Invasive Margin
IoU	Intersection Over Union
MIL	Multiple Instance Learning
ML	Machine Learning
MLP	Multilayer Perceptron
nits	Number of Iterations
RDF	Random Decision Forest
ROC	Receiver Operating Characteristic
SHG	Second Harmonic Generation
SVM	Support-Vector Machine
TCGA	The Cancer Genome Atlas
TMA	Tissue Microarray
TME	Tumor Microenvironment
WSI	Whole Slide Image

Glossary of Biomedical Terms

Histology	Histology is the study of the microscopic anatomy of body tissues.
Histopathology	Histopathology is the branch of histology that includes the microscopic identification and study of diseased tissue.
H&E	Hematoxylin and Eosin staining is a technique to stain otherwise transparent tissue sections. It is the most widely used staining in medical diagnosis - H&E is applied to almost every sample of tissue being assessed by a medical pathologist.
IHC	Immunohistochemistry (immunostaining, IHC) is a special tissue staining technique requiring special machinery and skilled technicians. The technique leverages the interaction of antibody and antigen (hence the "immuno-"). IHC tests are very specific and can inform where exactly an assay target is located in the tissue.
ECM	The extracellular matrix is the material filling space in between cells. ECM is critical for human physiology by providing such functions as passive structural support, cell mobility regulation by adhesion, cell-to-cell signaling mediation, mechanical-to-molecular signal conversion, material storage.
Collagen	Collagen is the most abundant protein in the human body. It is a major structural component of the extracellular matrix. Collagen molecules form fibers that interconnect to form a supportive environment for growing cells and tissues. Within the tumor microenvironment, specifically aligned collagen has been shown to stimulate tumor progression by directing the migration of metastatic cells along its structural framework.
Stroma	Stroma is a tissue type providing a structural or connective function and protects other functional tissues. Stroma is made of stromal cells and largely ECM.

Epithelium	The epithelium is a thin layer of epithelial cells. This layer forms a tissue type that makes the surface of organs. It covers the outside (e.g., skin) and the inside (mouth) surfaces of the body and acts as a barrier between the body and the world. Therefore, the epithelium is the first line of protection from mechanical, chemical, and biological damage and has a high renewal capacity. Epithelial cells reproduce and divide more rapidly than others and give rise to cancer more often.
Tumorigenesis	Tumorigenesis (oncogenesis, carcinogenesis) is the process of tumor development.
TME	The tumor microenvironment is the most proximal microscopic environment of the tumor – an interface where tumor cells interact with the patient's body.
DNA	Deoxyribonucleic acid is a long polymer molecule made from repeating units called nucleotides. In living organisms, it serves as a storage of genetic information. In our bodies, DNA molecules can be damaged and repaired by a variety of mechanisms. Cancer occurs when DNA repair fails.
RNA	Ribonucleic acid is another long polymeric molecule with an important role in biology. Its primary role is to convert the information stored in DNA into proteins.
Biomarkers	Biomarker (biological marker) is a measurable indicator of biological state or condition. Typically biomarkers are examined to assess the disease. Biomarkers can be molecular (DNA, RNA, protein), cellular, and digital (e.g., medical imaging derived measurements that allow disease detection).

TABLE OF CONTENTS

1. INTRODUCTION

1.1. Research Context

As humanity dwells in the age of data, a considerable part of our daily activities is captured digitally and gets analyzed. A vast amount of digital information is acquired in a clinical setting as image data using well-established medical imaging techniques such as X-ray, magnetic resonance imaging (MRI), computed tomography (CT), ultrasound, and many more. Digital image analysis (DIA) is used to extract meaningful information contained in images. When applied to medical images, DIA informs treatment decisions and directly affects patients' lives. Therefore, DIA algorithms particularly those based on machine learning (ML) whose use is intended for specific medical purposes qualify as medical or diagnostic devices and have to undergo regulatory clearances. There are hundreds of DIA-based medical devices cleared for clinical use worldwide for automated labeling, visualization, and quantification of organ (brain, lung, breast, prostate, cardiovascular system, thyroid) structures, documentation of abnormalities, tumor contouring for therapy planning from CT scans, X-ray or MR images, retinal diseases diagnosis from ophthalmic images, assistance in the analysis of ultrasound images.

In this context, cancer diagnoses often rely on analyzing visual information contained in the microscopic anatomy (histology) of surgically removed tumor tissues. In a standard diagnostic workup, laboratory-processed tissue specimens are placed on glass slides and routinely stained with hematoxylin and eosin (H&E) stains to color otherwise transparent tissue sections [1]. Alternative staining techniques are available and commonly are referred to as "special stains". Stained slides are presented for patologist manual review under an optical microscope (see Fig. 1.1). Differential diagnosis of tumors aims to classify a malignancy into clinically relevant categories. Hence, a pathology diagnosis implies a label that is applied to a patient and enables further decisions about treatment and prognosis in the context of other clinical information. To arrive at a diagnosis, pathologists must consider many biological factors of pathology, usually presented as manual or digital assessment endpoints such as qualitative or quantitative evaluation of the size and shape, density, and alignment of tumorous tissue components. Objective, accurate, and standardized phenotyping of microscopic manifestations of the disease (histopathology) is a convenient system to guide treatment decisions.
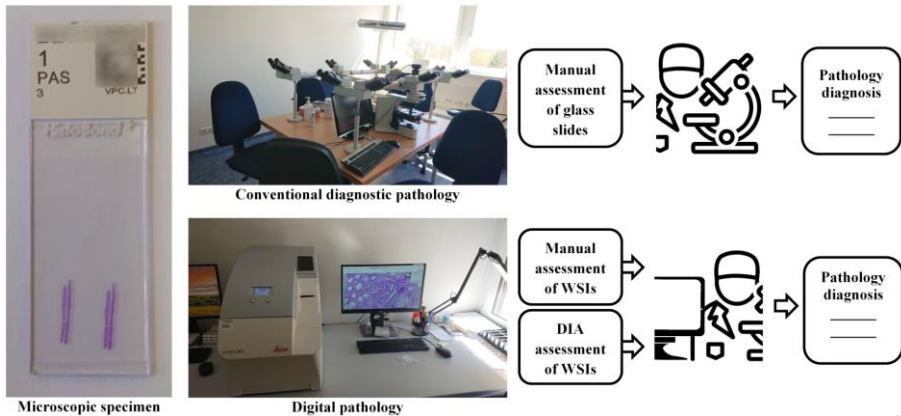
Figure 1.1 Tissue specimen histology analysis. Currently, there exist two approved ways for a pathologist to arrive at a pathology diagnosis. A conventional way is a manual assessment of glass slides under an optical microscope. A "digital" way is an assessment of WSIs, whether manually or with the assistance of approved pathology DIA tools.

Specialized hardware (high-capacity high-resolution bright-field microscopy scanners) can digitize a glass slide into a virtual slide or Whole-Slide Image (WSI). DIA-driven assessment of a pathology starts with pixel-level data of a tissue specimen image. It expands to object-level data by aggregating similar pixels into biologically meaningful and recognizable tissue components (see Fig. 1.2). Finally, object-level endpoints are employed to suggest an opinion at a patient level, be it a probability of disease recurrence or susceptibility to a specific treatment, or even a genetic condition.

Digitizing histopathology offers faster and more precise analytical approaches, also free from known sources of visual bias (optical illusions of size, color, hue, and shadow; inattentional blindness). Few digital slide scanners have been marketed in Europe under the Conformité Européenne (CE) mark since 2014, and in 2016 WSI technology was approved for primary diagnosis in the USA. Concordantly, in Europe, several ML-based pathology-specific DIA algorithms are already marked CE; however, to date, there are no regulatory clearances for pathology-related ML-based medical devices in the USA.
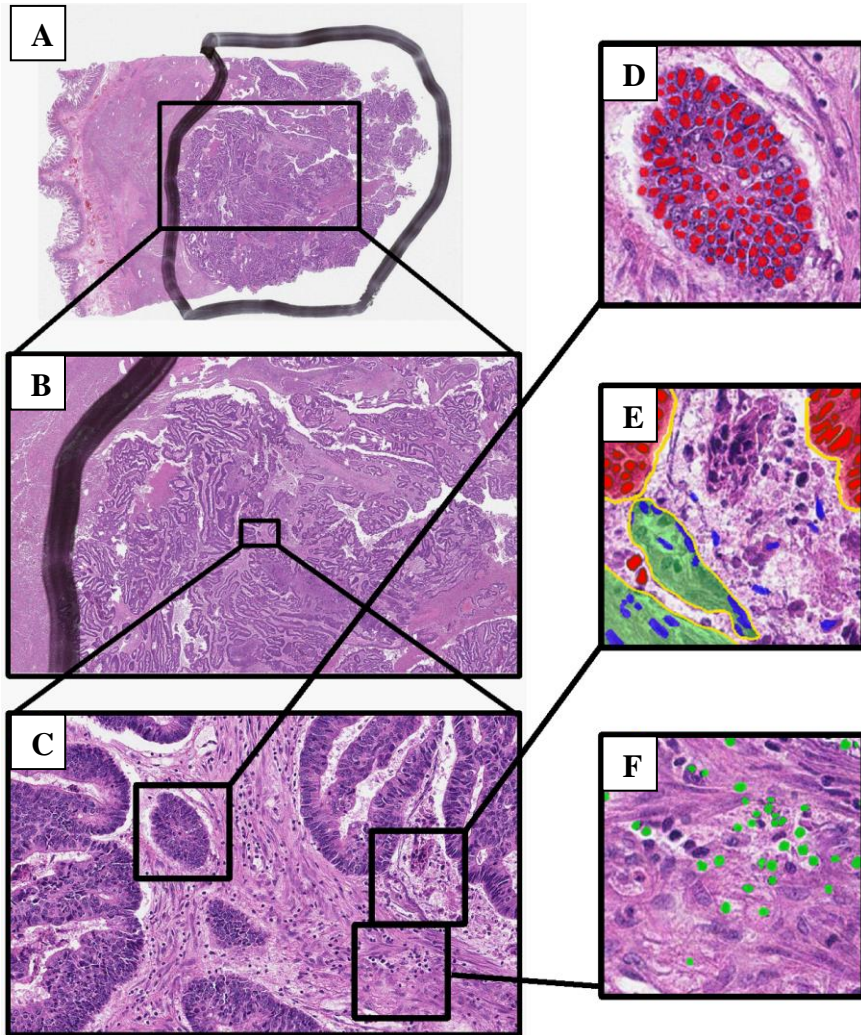
Figure 1.2 Whole-slide image of H&E-stained colorectal cancer tissue. The tissue specimen visible in panel A is approximately 2 cm in width and 1.3 cm in height. Pen markings were made on a glass slide by a pathologist to indicate tumorous tissue. WSI was scanned at a standard 0.5 microns per pixel resolution (corresponding to 20× optical magnification) and yielded a final image of 41,832×32,763 pixels size. B, C – low magnification sections of WSI. D, E, F – high magnification image excerpts of WSI showing tissue objects detected by DIA methods developed in this thesis. D is segmented tumor cell nuclei. E is tumor cell nuclei and tumorous tissue are highlighted in shades of red, connective tissue highlighted in green, cells of connective tissue are given in blue, and the remaining is dead tumor tissue. F is segmented immune cells (in green) surrounded by connective tissue.

1.2. Relevance of the Research

Advanced comprehensive analysis of solid tumors brings benefits to cancer patients. Tumor profiling by DNA, RNA, and protein biomarkers leads towards personalized curative decisions in oncology [2]. Targeted medications are proving invaluable for precisely pre-selected groups of patients. Therefore, medical pathologists use well-established methods to analyze solid tumor histology under an optical microscope to define groups of susceptible patients.

For a long time, diagnostic pathology was mainly focused on tumor cells. Tumor cell genetics explains many aspects of cancer development, but a growing tumor progresses while closely interacting with the patient's body (host). The tumor microenvironment (TME) can be understood as an interface of this interaction (the most proximal microscopic environment of the tumor) together with the host-allied interacting counterparts – cells of the inner and outer surface of organs and blood vessels, cells of connective, muscle, fatty, and neural tissues, cells of immune origin, and the material filling space in between cells (extracellular matrix (ECM)). Aggressive tumors exploit these interactions to benefit their growth by ensuring the supply of oxygen and nutrients, creating favorable conditions for the movement and spread of metastatic cells. TME has become a special topic in oncology due to our growing understanding of its function and role in tumor development. It is undisputed that TME assessment can provide critical therapeutic information [3-5], especially when dealing with tumors with ambiguous histology. Recent research reveals TME as an emerging target for personalized anti-cancer therapy [6-9].

In fact, digital pathology is even more tumor cell-centric than diagnostic pathology and largely ignores the TME. A plethora of DIA methods is available for tumor cell detection, segmentation, and classification. Nevertheless, methods targeting TME cells are being researched. For example, tumor-infiltrating immune cells (particularly lymphocytes) are important TME-born targets that can efficiently be detected, counted, and their density in tissue can be estimated by existing DIA methods [10-13]. However, lymphocyte segmentation is merely mentioned in a few research papers. Similarly, connective tissue cells (stromal cells) are often mentioned in the context of cell segmentation problems not as a primary target but rather as hard-to-recognize cells negatively impacting the segmentation of tumor cells [14, 15]. Therefore, DIA methods specifically targeting TME-born cell types need to be developed.

Expert annotations drive cell detection (segmentation and classification) methods; however, the ECM component of TME is hard to annotate if at all possible. Although specialized imaging modalities (second harmonic generation microscopy [16], polarized light microscopy [17], fluorescent microscopy [18]) have been used to image ECM at high resolution and can be used as a source of ground truth, their capacity is limited. Meanwhile, more accessible bright-field microscopy methods cannot offer comparable precision. Therefore, robust and affordable methods for assessing biological information contained in ECM need to be developed for standard and readily available H&E-stained histology images.

The endpoints of pathology DIA (typically continuous variables) are further used by pathologists to profile individual patients and to stratify them into clinically relevant categories (by disease severity, adequacy of therapy, or treatment plan). There is accumulating evidence of successful application of unsupervised or weakly supervised methods for predicting patient therapeutic biomarker status, susceptibility to treatment, and disease recurrence [19-21]. Unsupervised ML promises to improve pathology DIA development by reducing heavy dependency upon experts' manual input. For example, a model predicting patient survival times with greater discriminatory power than an optimal combination of all classical domain expert-provided features (explicit features) offers a unique opportunity to standardize the diagnosis. However, building completely human-independent pathology DIA comes at the cost of reduced transparency and interpretability of predictions and accompanying ethical and professional issues. This motivates to explore an interplay between tumor-oriented and TME-oriented digital methods to improve the efficiency of explicitly developed methods, and at the same time, to avoid the lack of explainability of unsupervised techniques.

Diagnostic pathology mainly focuses on tumor cells. Inherently, pathology DIA (and, in a broader sense, digital pathology as a research field) is even more tumor cell-centric, with the methods targeting TME cells being underresearched. A considerable part of this dissertation is designated to develop and analyze DIA methods targeting TME-borne tissue objects traditionally not covered by existing pathology DIA methods and even by human pathologists.

The dissertation introduces digital pathology by a literature review of DIA methods in pathology, both historically important and state-of-the-art ones. The research part of the dissertation considers problems of tumor tissue classification into compartments, segmentation of cell nuclei,

classification of segmented nuclei, segmentation of tissue collagen carcass, and feature space engineering to detect tissue characteristics indicative of pathologic condition.

1.3. Object of the Dissertation

The object of this dissertation is tumor microenvironment compartment analysis in the whole-slide routinely stained histopathological images.

1.4. Aim and Tasks of the Dissertation

The aim of this dissertation is to investigate and propose new histopathology image segmentation and classification methods by targeting tumor microenvironment-related histologic tissue components.

With the view of realizing this aim, the following research tasks must be completed:

1. Develop and evaluate a colorectal tumor epithelium-stroma compartment classification method.
2. Propose a lightweight state-of-the-art tumor cell nuclei segmentation and classification method for the analysis of the microenvironment of breast and colorectal tumors.
3. Inspect existing collagen framework analysis methods and network features and develop a method to capture fibrous tumor microenvironment collagen framework in bright-field histopathological microscopy images and investigate whether obtained framework quantitative features can be used to predict differences in survival between different groups of breast cancer patients.
4. Develop and generalize a deep convolutional neural network method enabling simultaneous segmentation and classification of tumor microenvironment tissue compartments of the varying input WSI sizes for breast cancer patient therapeutic biomarker status classification.

1.5. Bioethics

The results obtained in Chapter 5 involved analysis of patient follow-up data, therefore the Lithuanian Bioethics Committee approved this study

(reference number: 40, date 2007-04-26, updated 2017-09-12). Other studies did not require bioethics approval.

1.6. Scientific Novelty of the Research

1. It was experimentally demonstrated that a convolutional neural network (CNN) based model trained directly on image data classifies colorectal tumor tissue more accurately than a support vector machine (SVM), random forest classifier (RDF), or multilayer perceptron (MLP) models trained on color and texture features of the same images.

2. Extensive research provides unequivocal evidence of fully convolutional neural networks (FCNN) being a state-of-the-art method for cell nuclei segmentation tasks. A novel modified FCNN-based algorithm for cell nuclei segmentation and a consecutive lymphocyte identification using MLP was developed and evaluated. The method performs comparably to state-of-the-art methods in terms of lymphocyte detection while at the same time enabling lymphocyte segmentation, which, in the case of lymphocytes, was previously not considered.

3. Theoretical analysis identified fibrous TME-collagen as a novel target for segmentation in bright-field images of tumorous tissue. An FCNN-based approach to segment collagen was developed and applied to capture collagen in breast tumor tissue images. It was experimentally demonstrated that the prognostic power of morphometric TME-collagen features is significantly higher than conventional clinical indicators. To the best of our knowledge, this has been the first method to capture collagen compartments in bright-field microscopy images.

4. The theoretical analysis revealed that FCNN could address the simultaneous segmentation of multiple object classes. Therefore, the approaches considered previously were aggregated into a single model capable of segmenting both tumor-related and TME-related objects of breast tumor tissue. Subsequently, segmentations were employed to engineer morphometric tissue image features to build and evaluate a breast tumor tissue component spatial relationship preserving WSI projection. WSI projections provided transformation of a tissue image into a fixed-size representation allowing classifier training on complete whole-slide images and enabled accurate predictions of breast cancer patients' therapeutic biomarker status.

1.7. Defended Statements

1. A CNN trained for segment-based colorectal cancer tumor tissue compartment classification directly from image data is more accurate on HE stained histopathological images than other ML approaches trained on engineered segment-level features.
2. An FCNN-based approach for cell nuclei segmentation and lymphocyte identification in breast and colorectal tumor images performs comparably to state-of-the-art methods in terms of lymphocyte detection at the same time enabling lymphocyte segmentation, is lightweight and shows good generalization properties.
3. An FCNN-based method is suitable for collagen framework segmentation from routinely stained bright-field microscopy images. Segmented collagen possesses indicative information of differences in survival between distinct groups of breast cancer patients.
4. Aggregated segmentation of tumor-related and TME-related components in routinely-stained WSI is possible in an FCNN-based model utilizing multi-layer annotation masks while treating each class segmentation as a binary pixel-level classification problem and providing a basis for spatial relationship preserving WSI projection. The proposed WSI projection built upon morphometric tissue features enables ML classifier training on complete whole-slide images and allows accurate breast cancer patient therapeutic biomarker status predictions from routinely stained pathology images.

1.8. Approbation of Research

The results of the thesis were published in the following peer-reviewed periodicals:

1. M. Morkūnas, P. Treigys, J. Bernatavičienė, A. Laurinavičius & G. Korvel. "Machine Learning Based Classification of Colorectal Cancer Tumour Tissue in Whole-Slide Images". Informatica 29, 75-90, doi:10.15388/Informatica.2018.158 (2018).
2. E. Budginaitė, M. Morkūnas, A. Laurinavičius & P. Treigys. "Deep Learning Model for Cell Nuclei Segmentation and Lymphocyte Identification in Whole Slide Histology Images". Informatica 32, 23-40, doi:10.15388/20-INFOR442 (2021).

3. M. Morkunas, D. Zilenaite, A. Laurinaviciene, P. Treigys, A. Laurinavicius. "Tumor Collagen Framework from Bright-Field Histology Images Predicts Overall Survival of Breast Carcinoma Patients". Scientific Reports, accepted on 2021-07-18, doi:10.1038/s41598-021-94862-6 (2021).

The results of the thesis were presented at the following international conferences:

1. M. Morkunas, A. Rasmusson, A. Laurinavičienė, P. Treigys, A. Laurinavicius. "Quantitative Analysis of Tumor Collagen Fiber Features in Histology Images Predicts Overall Survival of Breast Carcinoma Patients". ECDP 2019: 15th European Congress on Digital Pathology, 2019, Warwick, UK. Poster presentation.
2. M. Morkūnas. "Tumor Microenvironment – Learning from Collagen Framework". Innovative Pathology, September 20, 2018, Vilnius, Lithuania. Oral presentation.
3. M. Morkūnas. "Intra-tumor Genetic Heterogeneity of Lung Adenocarcinoma as Investigated by Next Generation Sequencing". 9th European Regional Conference on Thoracic Oncology. 2017-06-16/17, Vilnius, Lithuania. Oral presentation
4. M. Morkūnas, P. Treigys, A. Laurinavičius, J. Bernatavičienė. "Whole-slide Pathology Images Spatial Mapping of Intra-tumor Genetic Heterogeneity". NEUBIAS2020: Network of European bioimage analysts, Lisbon, Portugal 2017-02-15/17. Poster presentation.

The results of the thesis were presented at the following national conferences:

1. M. Morkūnas, P. Treigys, A. Laurinavičius. "Deep learning-based method for quantitative collagen framework analysis in routine pathology images". 10th international workshop on Data analysis methods for software systems (DAMSS), November 29 - December 1, 2018, Druskininkai, Lithuania, Oral presentation.
2. M. Morkūnas, P. Treigys; J. Bernatavičienė, A. Laurinavičius. "Impact of colour on colorectal cancer tissue classification in hematoxylin and eosin stained histological images". 9th International workshop on Data Analysis Methods for Software Systems (DAMSS), November 30 - December 2, 2017, Druskininkai, Lithuania. Oral presentation.

3. M. Morkūnas, P. Treigys, A. Laurinavičius. "Machine Learning Based Classification of Colorectal Cancer Tumor Tissue in Whole-Slide Images". Kompiuterininkų dienos – 2017. 2017-09-21/22, Kaunas, Lithuania. Oral presentation.
4. M. Morkūnas, P. Treigys, A. Laurinavičius. "An Overview of Methods to Spatially Map Intra-tumor Genetic Heterogeneity in Whole Slide Pathology Images". 8th International Workshop of Data Analysis Methods for Software Systems, 2016-12-01/03, Druskininkai, Lithuania. Poster presentation.

2. LITERATURE REVIEW OF DIGITAL IMAGE ANALYSIS METHODS IN PATHOLOGY

Two important domains frame the scientific grounds of the results in this dissertation. The first domain is cancer research (briefly introduced in Chapter 2.1), which defines the aim of this thesis. The second domain is machine vision (covered in Chapter 2.2) that provides technological solutions and informatics applications to complete tasks that arise from cancer research and, principally, its sub-domain histopathology.

Machine vision will be introduced from a pathologist-centered perspective:

- Historically important approaches to automating pathologist workflows (various tumor grading and scoring systems providing endpoints applicable at the patient level) will be introduced in Chapter 2.2.1.
- The majority of now-existing digital pathology methods (and use-cases applicable at the object level) developed specifically for tumor cells (hence, tumor cell-centric or tumor cell-oriented) will be covered in Chapter 2.2.2 focusing on how cancer research benefits from advanced ML-driven computer vision applications in digital histopathology.
- Chapter 2.2.3 aims to highlight TME-born objects of tumorous tissue and existing digital pathology methods approaching TME-oriented computational problems.
- Chapter 2.2.4 will touch upon the problematics of the availability of labeled data for digital pathology methods and how the lack of objective ground truth shifts the digital pathology research from straightforward (based on explicit rules) supervised DIA methods to less supervised computational techniques.
- Methods leveraging mostly or entirely unlabeled image data will be covered in Chapter 2.2.5.
- Related works being conducted in Lithuania will be covered in Chapter 2.2.6.

2.1. Cancer Biology, Tumor Evolution, and the Tumor Microenvironment

Cells in our bodies grow and divide to support the needs of the organism, and unnecessary or malfunctioning cells are removed from the body via a precisely controlled mechanism. However, this order breaks down when malignancy develops. Virtually anywhere in our bodies, tumors can form

when cell division and death slip out of control and the abnormal growth of cells starts and spreads into surrounding tissues. The ability to foresee and predict the behavior of individual cancer is essential for precision cancer medicine.

Several decades ago, Peter Nowell proposed to view cancer as an evolutionary process [22]. To date, the extensive evidence of complex adaptations ongoing in tumors [23] and the discovery of genetically divergent populations of tumor cells has confirmed the evolutionary driving force of cancer [24-27]. Over the past several decades, researchers proposed different models to explain tumor progression. According to these models, the tumor is subject to selective pressure while evolving to acquire distinctive capabilities. In 2000 Hanahan and Weinberg listed six cancer hallmarks comprising six biological properties acquired during normal-to-malignant transformation [28]. Namely, the ability to auto-generate growth signals, block anti-growth signals, invade tissue and spread, replicate endlessly, secure blood supply, and escape cell death. In such a tumor cell-centric approach, tumor evolution begins when a single cell in the normal tissue transforms and expands to form a tumor mass. Yet, now it is undisputed that tumors are more than detached blocks of immortal cells.

Like all evolutionary processes, tumor evolution is also shaped by the environment. As cancer cells divide, advance in size, number, and capability, they also induce heavy modifications on the tissue they grow in [29]. The next generation of cancer hallmarks published in 2011, besides two new tumor cell-related properties (altered energy metabolism and genome instability), also includes two properties attributed to non-tumor cells – abilities to evade organism immunity and promote self-advancement by inflammation of surrounding tissue [30]. A decade later, yet new evidence demonstrates that developing tumors attract, reorganize, and incorporate stromal cells, immune cells, vascular cells, and extracellular matrix (ECM) to condition the tissue for tumor progression [4, 31]. Collectively, this is referred to as the tumor microenvironment. Often, TME comprises the larger part of the overall tumor mass. In 1889 Steven Paget proposed that the "soil" (organ tissue) supports the "seed" (tumor) growth due to specific interaction and cooperation [32]. Accumulating evidence shows that TME controls tumor initiation, growth, invasion, metastasis, and response to therapies.

The increasing significance of TME in cancer biology has caused a major shift of cancer research from a tumor-centric model to a TME-centric one. The advancement in our understanding of the TME has led to the discovery of effective anti-cancer therapies. A connection between inflammation and

cancer was first noted by Rudolf Virchow back in 1863 with the discovery of immune cells in neoplastic tissue at sites of chronic inflammation [33]. Recruiting a patient organism's immunity for therapeutic purposes in cancer has long been a goal in immunology and oncology and became a reality with the emergence of such cancer treatment strategies as cancer vaccines [34], immune checkpoint blockade [35], and direct infusion of tumor-fighting immune cells into the body [9]. Moreover, therapies targeting TME components other than immunity-related are also developed. These include agents degrading or deconstructing TME [7] (improving the delivery of drugs to tumor cells), preventing blood vessel development around the tumor [8] (cutting off energy and oxygen resources), interrupting cell-to-cell signaling [36] (cutting off growth stimulation), and co-targeting tumor cells and their non-tumor neighbors [37].

As of 2019, there are 47 approved cancer immunotherapies and more than 5,000 being actively tested [38]. Enrolling in such trials can be of utmost importance for cancer patients since trials provide the opportunity to receive the newest treatments. The fact that only less than 5 percent of cancer patients participate in clinical trials indicates the presence of certain barriers, and success greatly depends on a timely and accurate diagnosis.

2.2. Machine Vision for Digital Pathology

Most often, solid tumor cancers are diagnosed by a medical pathologist, visually inspecting tissue slides. Tissue samples are obtained surgically in a diagnostic workup, sectioned and placed on a glass slide, and stained to highlight specific biomarkers. Pathology slides contain important features – spatial information of the tumor cell morphology and tumor microenvironment that cannot be captured by other routinely used diagnostic methods. The confirmation of the presence of disease, outcome prediction, and therapy choice explicitly rely on information present in pathology slides. Computational tools embedded in an image-based environment extract clinically actionable knowledge from pathology information. Computational techniques serve malignancy identification, disease prognosis, treatment plan selection and prediction of response to treatment, patient inclusion in ongoing clinical trials, and cancer research in general [39-42]. Constant discovery of new tumor tissue biomarkers, the introduction of whole-slide imaging systems, active development of the computer vision field guarantees substantial interest in advanced digital pathology algorithms that would accomplish highly specific research tasks.

Qualitative and quantitative analysis of histology objects in a typical pathology image is a complex task that, most simply, may be viewed as consisting of image segmentation step, feature measurement, and ML-based classification of segmented image primitives. ML methods can be subdivided into traditional and "deep" learning methods. ML methods already widely used in the 1980s and 1990s (decision tree learning [43], MLP [44, 45], support-vector machines (SVM) [46], random decision forests (RDF) [47, 48]) can be considered traditional ML methods. While deep learning (DL), as a concept of a multiple-layer artificial neural network (ANN) trained by backpropagation [45], has also been known for decades, its widespread use began quite recently with a GPU implementation of a CNN in 2011 [49, 50]. As input, both approaches take large amounts of labeled data to learn features with a certain degree of interpretability (such as texture or color) and adapt model parameters according to the distance between the produced and the desired outputs. Finally, predictions on new instances of the same data type have to be made. Typically, detection and identification are needed to count histology primitives, while for inference of morphology one needs to perform precise segmentation. Morphological features that pathologists conventionally assess, such as the degree of structural differentiation, and cell nuclei pleomorphism indicate the presence of malignancy and determine tumor grade.

Most cancer grading systems consider the resemblance between neoplasia and its tissue of origin, size, shape, staining variation of tumor cell nuclei compared to normal nuclei, and the abundance of mitotic figures. When deciding on therapy, the level of expression of specific biomarkers in tumorous tissue is a crucial indicator for patients that may respond to targeted treatments. Biomarkers are assessed differently with additional and special tissue stainings, often yielding quantitative results and requiring the interpretation of expression patterns and intensities. The result of the immunohistochemistry assay is one important criterion of eligibility for therapy. There are many ways to cure cancer, but the rate of success varies. Depending on the cancer type and stage, the recurrence rate can be as high as 100%. Moreover, at the time of diagnosis, a significant proportion of patients with cancer already have their disease spread into secondary locations in their bodies. In such a scenario, pathologists have to evaluate the tissue for metastasis (frequently micrometastasis) to confirm recurrent cancers.

If viewed from a computational perspective, tumor grading merges estimating object counts, color, size, orientation, perimeter, convexity, area,

and distance to the neighbors. On the other hand, biomarker assessment involves identifying appropriate tissue areas to analyze, object segmentation (often smaller than the cell – nuclei, membranes, cytoplasm), object classification, distribution profiling, hotspot detection. Metastasis detection poses different challenges – often, a few objects (tumor cells) have to be detected in several WSIs in a bulky and crowded background (lymph node tissue). Both tumor grading and biomarker assessment results usually are presented as scores.

2.2.1. Digital Pathology Grading Systems

The early attempts to introduce computational tools into pathology workflows were the automation of various scoring systems. A digital tool can provide a second opinion, alert when particular actions are needed, thus reducing human workload. Good examples are Nottingham and Gleason scoring systems. Pathologists use the Nottingham system [51] to grade breast tumors and the Gleason score [52] to grade prostate cancer.

The three qualitative components of the Nottingham system are – nuclear pleomorphism, tubule formation, and mitotic count. The system produces three grade scores that are of recognized prognostic usefulness. Since its introduction in 1991 by Elston and Ellis, multiple research teams have attempted automation of the Nottingham system or suggested better alternatives [53]. In 2006, Petushi et al. [54] explored tissue micro-textures to quantitatively evaluate two Nottingham system components (nuclei and tubules). Their algorithm included grayscale conversion, object segmentation with adaptive thresholding and morphological operations, object labeling, feature (area and intensity-based) extraction, object classification using a decision tree classifier. The procedure could detect nuclei-rich areas, segment nuclei, classify nuclei into three classes (immune-origin, epithelial-origin regular, epithelial-origin irregular). The authors could measure nuclei density and abundance of higher histological structures – tubules defined as high-intensity blobs surrounded by a nuclei-rich area. The quadratic statistical classifier [55] trained on these two features could distinguish high-grade and low-grade tumor images (with 91.45% classification accuracy).

In 2008, Doyle et al. [56], in their attempt to grade breast tumors, used an overwhelming engineered (also called "hand-crafted") 3468-dimensional feature space. Texture-related features were extracted by image processing techniques (Gabor filters [57], and Haralick second-order co-occurrence matrix features [58]) directly from images. The authors did not present a

nuclei segmentation method and instead used manual marking of nuclei centroids to build graphs and extract structure-related features (Voronoi diagram [59], Delaunay triangulation [60], and Minimum spanning tree [61]). The final feature space was reduced by spectral clustering and images classified by SVM into low- and high-grade classes with 93.3% classification accuracy.

The first work thoroughly implementing the Nottingham system was published in 2008 by Dalle et al [62]. The proposed method utilized multi-resolution images. Tumor area and histological structures were detected within low-resolution images, while high-resolution images were used to segment and classify cells and mitotic figures. The authors applied Otsu thresholding in color space to localize the tumor and corrected small artifacts by morphological closing and opening operations. The detection of histological structure formation was adopted from Petushi et al. [54] (discussed above). Cells were segmented by the Gaussian color model [63] followed by two-stage classification based on modeled color distributions, where the first classification stage selects for candidate mitotic figures and epithelial cells. The second classification stage assigns epithelial cells to one of the three classes based on the distribution of color in the nucleus (homogeneous, moderate, and clumped). True mitotic figures are selected from candidates by roundness, eccentricity, area, and color intensity. Overall grading mimics the pathologist's routine where each of the Nottingham system's components produces a score based on accepted rules and aggregates these scores into the final grade.

In the 1960s and 1970s, Donald Gleason [52] developed a grading system for prostate tumors. While the Nottingham and Gleason systems grade different types of cancers, the latter is also based exclusively on histological structures. The Gleason system has undergone several revisions regarding score interpretation, yet its principle has never changed. Numerous works on Gleason scoring (grading) automation have been published. In 2007, Naik et al. [64] published a method to segment histological structures (glands) for prostate tumors. The authors succeeded in finding specific shared characteristics for all gland regions. Each gland's nature has underlying sequential architecture – the lumen surrounded by the cell cytoplasm and outlined by a ring of cell nuclei. Color values allowed identifying the components of a structure by training a Bayesian classifier [65] on a set of manually denoted pixels. The geometric active contour is initiated on the identified lumen border (central component) and evolves to capture the whole structure. Regions too large to contain histological structures are

removed by applying size constraints. A feature vector describing a segmented gland contains 16 shape-related measurements such as the area, perimeter, compactness, smoothness of both lumen contour and the gland defining contour. The authors apply manifold learning to reduce the dimensionality of the dataset and train an SVM classifier to discriminate the grade of prostate tumors. The proposed method was compared to the previously developed approach utilizing manual gland delineation. Even though automatic and manual segmentations often differ, a fully automated algorithm produces comparably accurate grading.

The purpose of the cancer biomarker assay is to highlight the enhanced property of the tumor. Immunohistochemistry assay targets a specific subcellular location, and depending on the level of trait manifestation, produces varying staining intensity and continuity (typically of brown color). Often, objects not expressing targeted traits are stained in a different color (typically blue color). Digital image analysis for biomarker assessment requires identifying the region of interest, segmenting targeted objects (cell nucleus, membrane, or a cytoplasm), and quantifying positive (property-expressing) objects against negative (non-expressing) objects. In general, the digital assessment of biomarker assays is highly specialized, with many proprietary tools available [66]. In 2018, Bankhead et al. [67] published a quantitative evaluation of five immunohistochemical tissue biomarkers through the open-source pathology image analysis platform QuPath. Virtual stain space is produced by color deconvolution and allows identifying and simultaneously separating positive and negative cell nuclei. Oversegmentation artifacts are solved by morphological processing, and the areas of each cell are approximated by propagating nuclei area with distance-to-neighbor constraint. The specifics of an assay restricts biomarker analysis exclusively to tumor cells. Therefore, multi-dimensional (>100) feature space is derived from segmented nuclei morphometry and staining intensity measurements, and the expert annotation-guided random decision forest classifier is trained to retain only tumor nuclei. The staining intensity and the proportion of positive nuclei yield assay scores (according to different accepted pathology guidelines). Digital image analysis achieved similar scoring results when compared to manual scoring by an experienced pathologist.

The examples discussed above employ DIA to more or less mimic a pathologist workflow by summarising tumor grade (or score) from predefined quantitative pathology endpoints (inspired by classification systems used in manual tumor scoring). However, more recent and more

advanced approaches to grade and score tumors or produce other patient-level predictions are most often based on tumor compartment-agnostic techniques employing weak labels with models trained directly from image data where feature engineering is not needed. These methods are discussed in more detail in Chapter 2.2.5. On the other hand, when desired pathology DIA endpoints are at the tissue object level, for example, when validation of detection (e.g., metastasis, biomarker status, prognostic pattern) is intended by visualization, feature engineering is still feasible.

2.2.2. Tumor Cell-Oriented Computational Techniques

Example methods discussed above demonstrate that a typical pathology image analysis workflow can be broken into three main steps: image preprocessing (usually pixel labeling), feature extraction, and diagnostic decisions, with a wide variety of well-known methods available to complete individual step.

Relatively simple image histogram-based thresholding has been historically used to segment cell nuclei directly or as a preprocessing step before applying more sophisticated algorithms. The segmentation task utilizes both global and local (adaptive) thresholds, yet in general thresholding approach is most suitable for high contrast images. To reduce segmentation artifacts or to capture large composite structures such as glands and tubules, binary segmentation maps produced by thresholding can further be modified by morphological erosion, dilation, closing, and opening operations [68].

Utilizing thresholding as a preprocessing step for the watershed [69] algorithm is yet another practical segmentation approach. Watershed assumes an image as a topographical surface where a similar group of pixels makes up a sort of drainage basin to capture the rainfall. The watershed algorithm often suffers from over-segmentation and has limited applicability for objects with weak boundaries but can be improved by eliminating local minima in a preprocessing step by thresholding. Thresholding can also be coupled with an edge detector (e.g., the Canny [70], Hough transform [71]) or a shape-fitting algorithm and can produce contours of cells and histological structures [68].

Deformable models are a group of more advanced methods to acquire cell boundaries that utilize energy minimizing frameworks [72, 73]. These methods attempt to deform and push a shape prior following an image gradient towards points located on a homogenous object's contour.

Initialization of a shape requires proximity of the object of interest and often leads to under-segmenting overlapping structures. The watershed algorithm has been used to identify the candidate regions to place the initial seeds for the active contours. Both parametric and geodesic active contours are used to segment histology objects.

Groups of similar pixels can be segmented out by clustering. Both hard and soft clustering can be utilized for segmentation. A pixel is associated with the cluster by distance metrics, although, in the case of soft clustering, it can belong to more than one class (fuzzy membership), so an optimum (minimum) number of clusters has to be found. Adaptations of the Fuzzy C-means approach incorporating pixel's spatial and neighborhood information proved to be noise-resistant and more accurate than traditional K-means [74].

The Markov Random Field model is often applied to refine initial segmentation [75-78]. Segmentation is modeled as an optimization problem with prior knowledge of pixel neighborhoods. The neighborhood principle suggests representing an image as a graph, and the segmentation then can be understood as a graph-cutting algorithm that effectively breaks the edges connecting objects to the background. Initial coarse segmentation sets the seed points to select objects, and the cuts are made by minimizing energies often used in computer vision (preserving coherence and smoothness of segmented objects).

Pixel labeling in a digital pathology image through segmentation is the process of partitioning a large digital image into small but more meaningful segments. Most of the above methods will produce image segments already capturing desired shapes (nuclei, histologic structures). When the object of interest is relatively large (e.g., whole tumor tissue in an image), approaches as simple as image partitioning into small, rectangular, possibly overlapping, or multiresolution patches are suitable for segmentation by classification. Typically, a set of image patches is systematically sampled from WSI. Each patch receives a prediction of belonging to a class by analyzing its content. All patches from WSI are sorted as being of background or foreground class with a certain probability. Patches reassembled into a single likelihood map provide a rough segmentation mask of WSI. In theory, it is possible to target only a central pixel of a patch, thus retaining the greatest detail of the segmentation but bearing in mind the size of a typical WSI, this approach would be extremely computationally intensive.

Segment-based classification often relies on image features such as color, intensity, coarseness, contrast, directionality, regularity, and roughness.

Local binary patterns [79-81], Gabor filters [82, 83], Haralick texture [84, 85], Tshebicheff moments [86], and responses to filter banks [87-89] (such as textons) are extracted from image segments and build up a feature space. However, training a classifier requires a certain amount of prelabeled data (often done manually). ML methods follow a supervisory signal to separate clusters of similar points in constructed feature space. SVMs, RDFs, MLPs, and different flavors of Manifold learning approaches successfully classify histologic objects.

Engineered feature space-dependent ML classifiers often require intense domain knowledge and suffer from a demand to extract more and more information from each tissue sample. For several years, solutions for a segment-based classification problem were evolving towards increasing the number and complexity of features extracted. Sethi et al. [90] report the use of the Wndchrm [91] software to build 93 features space to discriminate between epithelium and stroma compartments of prostate cancer tumors. As described in the same study Wndchrm can automatically extract up to 3,000 predefined image features. In a slightly different tumor classification task, generally relating to normal-malignant breast cancer tissue classification 256 handcrafted features extracted per superpixel were described [92].

Recent years witnessed the dominance of DL-based solutions in computational pathology. A wide variety of DL models (built upon convolutional, recurrent, and autoencoder neural network architectures) are available for all kinds of histologic object detection, segmentation, and classification. Artificial neural networks do not require feature extraction but instead can solely rely on end-to-end feature learning directly from images.

CNN in digital pathology was primarily adopted for segment-based classification [91, 93-95]. Although CNN models proved applicable in pixel-level classifiers [96, 97], in which each pixel is assigned a class label of its enclosing segment, they suffer apparent limitations. The patch size and sampling density imply a heavy computational load. Single-pixel segmentation accuracy requires single pixel sampling strides, thus to maintain reasonable computational speed, the patch size has to be relatively small, and the context information cannot be fully utilized. Due to the same reasons, models were usually built with relatively shallow architectures, typically contracting kernel size closer to the output.

In 2015 a fully connected CNN architecture was introduced, enabling predictions at every pixel by training a model pixel-to-pixel [98]. An approach is based on replacing fully connected layers of a CNN classifier with convolution layers and applying an up-sampling strategy to obtain

31

spatial output maps. An introduced skip-connection element combines the final prediction layer with lower layers to reduce segmentation coarseness. The FCNN architecture was quickly adopted for computational pathology tasks, and some prominent CNN architectures were even born from the field of medical imaging. The U-Net built upon FCNN introduced a cascade of up-sampling layers connected by skip-connections to the convolutions on the down-sampling path of the architecture [99]. The FCNN architecture was adopted and intensively modified in different research areas for particular tasks. In 2017, Xu et al. [100] introduced a deep multichannel neural network for simultaneous gland detection and segmentation. The proposed model achieves foreground segmentation via an FCNN channel extracting high-level features. The boundaries between glands are found in a multi-scale CNN channel. The region proposal channel based on Faster R-CNN detects glands and their locations, and shallow CNN then aggregates the output of previous channels to produce the final result. Similarly, multi-channel FCNN learning was utilized to refine foreground segmentation boundaries by parallel segmentation of both foreground and background. The approach was tested on the radiograph, ultrasound, and colorectal cancer histology datasets [101].

In 2018, Gecer et al. [102] used multiple separately trained FCNN models to discriminate irrelevant areas in whole slide breast histopathology from diagnostically relevant regions by selecting optimal image magnification and provides a saliency map for WSI. Similarly, Rawat et al. [103] applied FCNN to produce a spatial heatmap of predictions depicting areas in breast tumor images characteristic of tumor biomarker status.

In 2019 a heavy modification (in terms of architecture complexity) to the U-Net architecture was introduced – Micro-net, FCNN utilizing multiple parallel operations (multi-scale CNN concept) applied to the same input [104]. The Micro-Net outperformed U-Net on various tasks, however, it took considerable time to train. Bandi et al. [105] constructed a tissue detector based on FCNN capable of tumorous tissue discrimination from the background at multiple WSI resolutions. The authors demonstrated that a single FCNN model trained to detect tissue at a range of image resolutions performed comparably to multiple FCNN models trained for a specific resolution. Pontalba et al. [106] employed FCNN paired with a segment-classifying CNN in an ensemble as weak predictors to produce the final segmentation of cell nuclei of various tumors in histology images.

In 2019 the results were reported for the Kaggle 2018 Data Science Bowl, which challenged participants to segment cell nuclei in a variety of

microscopy images. The majority of participants used CNNs, and unequivocal evidence of FCNN being a state-of-the-art method for cell nuclei segmentation tasks could be concluded [107].

In 2020 a U-Net++ [108] was introduced – a multiple U-Net ensemble. Modifications included a built-in ensemble of various depth U-Net architectures, redesigned skip connections, pruning scheme for trained models to speed up inference. U-Net++ models significantly improved results over several biomedical image segmentation datasets. In 2021, Tran et al. introduced TMD-Unet, another modification of U-Net architecture employing densely connected convolutions [109] at each U-Net node and a multi-scale input. TMD-Unet was tested on several datasets, including a cell nuclei segmentation challenge of Data Science Bowl 2018 [107].

Various approaches utilizing region proposal network (R-CNN [110]) and its extensions (Fast R-CNN [111], Faster R-CNN [112], Mask-RCNN [113]) have proven successful in pathology object detection (mitosis [114], tumor cells [115], regions containing specific histologic structures [116]) applications. R-CNN contains a region proposal network (RPN) and a CNN classifier for proposed regions. An RPN employs a selective search algorithm to generate initial candidate regions and a hierarchical grouping [117] to merge candidates into final region proposals. CNN is then used to detect the object within the proposed regions. Moving CNN before RPN to produce convolutional feature maps directly from the input image increases the speed of region proposal significantly [111, 112]. Using FCNN instead of CNN enables object segmentation within the proposed region [113].

Inspired by the ways humans perform visual recognition tasks, Momeni et al. [118] proposed a hard attention model to predict brain tumor grade and molecular characteristics. The authors build their model on a recurrent neural network that is generally used to model sequential data by a non-linear mapping from its input to the hidden state regarding the previous hidden state. WSIs are modeled as a sequence of patches, and the proposed 2D spatial recurrent neural network model analyses a patch through glimpses into miniature regions within the patch. The network has separate channels for analyzing the contents and the location of a glimpse, and the glimpse network output is produced by passing an element-wise multiplication of both channels' outputs through a relu activation. The model's core is a two-layer recurrent neural network followed by fully connected layers that predict the next glimpse's location and produce the classification. This model's unique feature is the visual attention gate that eventually enables the

visualization of image regions that have the highest impact on classification decisions.

DL methods are, to some extent, limited by a complicated annotation of WSIs since they rely on pixel-level ground truth (GT) images. Autoencoders (AEs) are unsupervised learning methods that provide an opportunity to train models without labeled GT. The first part of AE is designed as CNN encoding input image into a compact feature vector through 2D convolutions. The second part of AE is designed to recover the original input from the encoded state through transposed convolutions. Trained AEs are used for staining normalization and have proven reliable feature extractors, cell, nuclei, and metastasis detectors [119-123]. Staining normalization, data augmentation, and harmonization can be crucial parts of many digital pathology workflows, especially when multiple sources of images are concerned. In recent years generative adversarial networks have been successfully applied to alleviate these tasks [106, 124-127]. A generative adversarial network aims to learn a generator distribution that matches the real data distribution in a minimax game between a generator and discriminator networks.

Regardless of its underlying architecture, the DL model is usually trained by optimizing a loss function. Models are optimized in an end-to-end fashion using stochastic gradient descent, and the iterative backpropagation algorithm is used to allow the information from the loss function to flow backward. Various domain-specific loss functions can be equipped to ensure models learn an objective accurately. FCNN is generally trained with a per-pixel cross-entropy-based loss function [128], possibly balanced or weighted to suit specific cases (e.g., data skewness). The focal loss [129] emphasizes learning hard examples by down-weighting easy examples. Dice coefficient-based losses are used to evaluate FCNN segmentations, with the ability to focus on challenging cases (e.g., small regions of interest). The shape-aware loss [130] calculates per point distance between contours of predictions and GT. Topology-aware loss [131] is designed to evaluate curvilinear structures. Hard-to-segment boundaries are targeted by distance map-based losses [132]. Custom combinations of multiple loss functions are possible (e.g., cross-entropy and Dice). When global image-level predictions are cast, patient survival data is usually targeted, and the loss function based on survival time [133] can be used.

2.2.3. TME-Oriented Computational Techniques

While most of the studies have focused on the tumor cells, the TME compartment, defined as all non-tumor components of cancer tissue, moves into the focus of biomarker research in oncology. Most, if not all, tumor-oriented computational techniques can be applied to specialized TME compartments. TME comprises blood vessels, nerve fibers, stromal cells, immune cells, and ECM that can (to some degree) be segmented, classified, and quantified. While tumor cell-centric computational tasks are clearly defined and well explored, only a few aspects of TME are researched in greater detail through computational pathology.

The number of vessels, size of the vessels and lumens, the distance to biomarker-positive or negative tumor cells were quantified and studied using image analysis. Vascular measurements of the TME correlate with estrogen receptor status. In 2017, Ing et al. [134] applied machine learning for vascular morphometry in hematoxylin and eosin (H&E) stained slides. In 2018, Yi et al. [135] applied FCNN and manually labeled microvessels in H&E images to produce tumor microvasculature segmentation.

It was previously shown that signaling by the parasympathetic nerves could suppress the growth of pancreatic cancer. Nerve fibers were highlighted via a biomarker analysis with QuPath [136]. A single digital image was acquired from a sample and evaluated by counting the nerve fibers in 20 continuous fields at 200× magnification. High nerve fiber density was associated with better overall survival in pancreatic cancer.

A host-tumor immune conflict is a well-known process happening during tumorigenesis. It is now clear that tumors aim to escape host immune responses by a variety of biological mechanisms [6, 137, 138]. Immune component detection often involves tissue epithelium-stroma classification reducing the noise irrelevant for the lymphocyte nuclei detection. It is common practice that one of the first computational tasks and an intermediate goal in comprehensive pathology image analysis is malignant (or tumor) tissue classification into the epithelium and stroma compartments. The reasoning behind this specific task is that it helps to build a picture of where and to what extent a particular cancer biomarker is present in the tissue. Modern prognostic and predictive stratification methods of cancer patients evaluate biomarker positive cells' distributions in each tissue compartment [139, 140]. Also, for certain types of cancer, the tumor epithelium-stroma ratio alone is recognized as an independent prognostic indicator [141]. The very recent rise of cancer immunotherapy research also

requires precise tumor microenvironment compartmentalization algorithms to identify and analyze tumor tissue infiltrating immune cells that are known to kill cancer cells [142]. The majority of publications in the field are focused on breast or prostate cancers. Multiple works explore traditional ML methods to achieve classification based on handcrafted features extracted from pathology images [91, 143-147]. Pathology image segmentation is performed by employing rectangular image blocks [143], overlapping square patches [144], multi-resolution square image blocks [145], various superpixel approaches - Normalized Cut, Simple Linear Iterative Clustering, Hierarchical Fuzzy C-Means, and also Multiresolution Superpixels [91, 146]. Recently, methods employed to classify tumor tissue have shifted from traditional ML approaches to deep convolutional neural networks [91, 93-95].

Many studies have demonstrated the importance of a specific tumor tissue area - the invasive margin (IM). By definition, it is a 1-mm-wide area around the border separating the normal tissue from malignant tissue. However, automatic IM detection is not straightforward, and research still uses manual IM delineation in WSIs. In 2018, Harder et al. [148] published a Tissue phenomics tool that employs biomarker analysis to detect tumor and stroma areas. Morphologic operations and network statistics in a post-processing step are applied to discriminate IM. In 2020, Rasmusson et al. [149] proposed automated extraction of IM. The authors applied explicit mathematical modeling of tissue compartment gradients in tumor-stroma-background classifier masks of colorectal and breast tumors overlayed with a hexagonal grid.

Precise analysis of the spatial distribution of different cell types in the tumorous tissue and are necessary to select patients who would best respond to various anti-cancer treatments. Specifically, anti-cancer immunotherapy offers an opportunity to dramatically change the clinical management of many types of tumors towards less harmful and more personalized treatment plans than conventional chemotherapy or radiation. Quantification of the immune infiltrate along tumor margins in the tumor microenvironment has gathered researchers' attention as a reliable prognostic measure for a growing number of cancer types [10, 12, 149, 150].

In 2016, Turkki et al. [151] and similarly, in 2018, Saltz et al. [11] proposed quantifying immune cells within the TME by identifying immune cell-enriched areas rather than stand-alone lymphocytes. In a study by Saltz et al., the authors have developed a CNN classifier capable of identifying immune infiltrate-enriched areas in WSI slides from The Cancer Genome

Atlas (TCGA) database. Turkki et al. detected lymphocyte-rich areas by training an SVM classifier on a set of features extracted by the VGG-F neural network from CD45 biomarker immunohistochemistry-guided superpixel-level annotations in digitized H&E specimen. Specifically, for lymphocyte detection, approaches utilizing FCNNs on the digital H&E slides were proposed [13, 152]. Both approaches investigate convolutional AE using histology sample patches with annotated lymphocyte nuclei. Detection and classification, but not segmentation of nuclei in H&E images, were done using spatially constrained CNN [153]. Notably, the classification into four cell types (epithelial, inflammatory, fibroblast, and miscellaneous) was performed on patches centered on nuclei considering their local neighborhood. The Hover-Net model published by Graham et al. enables simultaneous cell nuclei segmentation and classification by three dedicated branches of the model - segmenting, separating, and classifying [154]. In 2016 Janowczyk and Madabhushi employed an AlexNet model to identify centers of lymphocyte nuclei [155]. They trained the network on cropped lymphocyte nuclei as a positive class and sampled the negative class from most distant regions with respect to the annotated GT. Their trained network produces posterior class membership probabilities for every pixel in the test image. The authors identified potential lymphocyte nuclei centers by disk kernel convolution and thresholding. In 2019 Alom et al. utilized the same dataset to evaluate different advanced neural networks for various digital pathology tasks, including lymphocyte detection [156]. The authors proposed a densely connected recurrent convolution network to directly regress the density surface with peaks corresponding to lymphocyte centers. When compared to AlexNet, the densely connected recurrent convolution network improves the F1-score by 1%, yet it is worth mentioning that both discussed studies [155, 156] do not demonstrate method generalization - in the respective studies, the same dataset was used for training and testing.

Additional features bright-field images provide within WSIs originate from an arrangement of stromal collagen fibers. Collagen is a principal structural component of the extracellular matrix (ECM); its fibers connect to form a supportive environment for growing cells and tissues and thus have an essential role in tumorigenesis. A collagen-dense microenvironment has multiple roles:

- It acts as a static, space-filling material embedding tumor cells.
- It directs the migration of malignant cells along the straightened and aligned ECM structure towards the blood vessels.

- It interacts with specific cellular receptors and triggers various signaling pathways.
- Its' biochemical and biomechanical properties facilitate barrier formation and alter drug diffusion through the tumor tissue.

Progression of breast tumors has been reported [157] to pass evolutionary steps characterized by specific collagen organizational patterns.

Although collagen-dense stroma is distinguishable in routine tissue staining, some special histochemical techniques can be used to highlight collagen. Specialized imaging modalities exist to increase the precision of collagen framework assessment in tissue pathology samples. Birefringent collagen fibers can be visualized using polarized light microscopy or by the second harmonic generation (SHG) microscopy [16-18]. These techniques became reliable tools applicable to unstained tissue specimens.

A spectral phasors approach applied to multispectral fluorescence images of H&E stained tissue slides enables straightforward collagen segmentation [158]. A collagen-specific signal cluster in the phasor space could be identified and mapped to the corresponding H&E image resulting in a synthetic image mimicking Masson trichrome staining. Phasors were even more precise than SHG or polarized light microscopy since they could capture non-birefringent collagen. Image-based collagen biomarkers and the potential clinical value of this technique remain to be explored.

Although SHG, polarized light microscopy, and some other techniques, have been used to image collagen at high resolution, specialized imaging modalities are generally limited to the research due to the relatively high cost of equipment and lack of whole slide imaging capacity. Meanwhile, more accessible bright-field microscopy methods cannot offer high precision. There are few approaches like manual thresholding of hue, brightness, saturation, or stain separation using color deconvolution [159, 160]. However, these collagen detecting and segmenting methods are sensitive to day-to-day laboratory variation of the staining quality. Previous studies employed measurements of collagen fiber angles by hand and showed that collagen organization could be adequately measured by human observers and associated with chemotherapy response [161].

A few studies explored the feasibility of neural networks to detect and segment tissue collagen in bright-field microscopy images. Jung et al. presented deep convolutional neural networks applied to tissue collagen detection [162]. Graph analytics was applied to collagen deposits segmented by a neural network from histopathology images of simian

immunodeficiency virus-infected rhesus monkeys to detect collagen morphological changes in the course of infection. In a more recent study, Keikhosravi et al. [163] proposed the deep CNN-driven bright-field H&E to SHG image transformation and were able to produce synthetic SHG-like images of remarkably high detail level.

2.2.4. Ground Truth for Digital Pathology

Highly specialized techniques require carefully designed and realistic ground truth (GT) data depicting various classes of objects to build training datasets or evaluate algorithm performance. Ideally, DL algorithms should train on pathologists' systematically annotated image collections. Annotating pathology images is an extremely labor-intensive task involving the manual delineation of many objects. Skilled experts are not always available for the time needed to perform precise pixel-level annotations. Such a way of obtaining GT data comes with a tradeoff between quantity and accuracy. In 2014 Cruz-Roa et al. noticed that majority of tumor-stroma misclassifications produced by their model were mainly due to the pathologists' imperfect annotations [164]. The process of generating GT data is neglected in research papers with short descriptions, commonly referring to skilled specialists' manual work [143-145]. The GT data mining draws more and more attention with the increasing use of deep classification algorithms requiring significantly larger datasets to train. Studies often refer to commercial software used to delineate regions serving as GT for training and testing classifiers [91, 146, 165]. Models are trained interactively in a human-in-the-loop setting to reduce the domain experts' hands-on time.

Given diagnostic images, an artificial neural network adaptively learns to extract highly predictive features. Particular learning objectives may involve time-to-event prediction, including accurate prediction of overall survival and time to disease progression. Patient follow-up data is often readily available, and it is relatively easy to acquire diagnosis from the pathology report or pathologists' recordings in a laboratory information system. However, local tissue features that attracted the pathologist's attention and led to that particular diagnosis are not known or not used, and the diagnosis casts a label on an entire image. In such a case, WSI can be modeled as a bag of instances from the candidate patches, and multiple instance learning (MIL [166]) aggregates patch-level inferences into a global image-level classification. When supplemented with a visual attention mechanism model is then able to discriminate diagnosis-causing regions of WSI. The coupling

of MIL and visual attention for pixel-level (or segment-level) classification enables weakly supervised segmentation [165, 167-169].

2.2.5. Tumor Compartment-Agnostic Techniques

Deep learning approaches have been applied to various computational pathology tasks, with machine perception comparing and competing to that of a human. Recent years evidenced the undoubtful benefit from the insights that computational techniques can extract from pathology images. The accelerated evolution of modern histopathology image analysis was inspired by the generation of public collections of pathology images. However, the most significant additions came with methods to leverage mostly or entirely unlabeled image data. Inference of histomorphologic features informative of disease outcomes without pixel-level labels provided is a high-level task requiring understanding complete scenes. A model predicting survival with greater discriminatory power than an optimal combination of all classical domain expert-provided features offers a unique opportunity to standardize the diagnosis.

In 2020 Saillard et al. published research focused on automating the prognosis prediction of hepatocellular carcinoma patients after surgery [19]. The authors proposed a two-stage workflow employing a pre-trained model for patch-by-patch feature extraction and MIL to retrieve the most survival-predictive regions of WSI and calculate the patient's risk score. Interestingly, a feature-extracting model was not shown histology images during training. Instead, the authors used a ResNet50 model [170] pre-trained on the ImageNet [171] dataset. AE was then used to embed the 2,048 ResNet features in 256 dimensions. The MIL model then takes input batches of embedded per-patch features and selects the highest and lowest scorers to be transformed into risk prediction. When supplemented with a visual attention branch, MIL could focus patch selection on a pathologist annotated tumor compartment.

Yamashita et al. [20] proposed a similar approach to predict the prognosis of post-surgical HCC patients. They built the workflow on two DL models stacked to perform patch-by-patch tumor-normal classification followed by patch-level risk scoring. The authors trained the tumor detector on pathologists' annotations and used 100 tiles with the highest tumor probability to predict the patient's risk score in a MIL-like second model. This approach does not rely on a model pre-trained on unrelated images, yet to train the tumor detector, pixel-level annotations are needed.

Rawat et al. [21] published a tissue fingerprints concept. The authors trained the Resnet34 network [170] to match paired tiles from the same patient. The pair-matching model served as a feature extractor and MIL as a predictor of breast cancer clinical subtypes. Pairs of patches were sampled from the same WSI and were constrained to have a common border. The model was supposed to learn patterns of cells and tissue visible on both patches to achieve high pairing accuracy. Resnet34 produces a 512-dimensional tissue fingerprint for each patch analyzed. Given 120 patches from each WSI, MIL would then learn to classify cases according to clinical subtype defined by multiple biomarker assays. No labeled data is required to train a feature-extracting model.

Bulten et al. [172] proposed a fully automated method to grade prostate tumors. A high-level, complex workflow included a tissue detector, tumor detector, epithelium detector, and a scoring model. Amazingly, three out of four DL models used in the study were based on U-Net architecture. The tumor detection model is a shallow CNN architecture developed for patch-by-patch prostate tissue classification into malignant and benign. The epithelium detector was trained on H&E images annotated by mapping from preprocessed biomarker immunohistochemical assay images to epithelium binary mask. Semi-supervised labeling of segmented epithelium masks was applied by automated reading from digital patient records. The final model was trained on biopsies preselected (automatically from patient records) to contain pure tumor grades. In this step, a trained U-Net model produces a per-pixel classification into six classes. The volume percentage of each class label then defines the biopsy score. In a final evaluation, the proposed model outperformed 10 of 15 pathologists in an expert panel.

2.3. Related Research in Lithuania

Both local research groups, as well as those involved in international collaborations, have applied pathology DIA methods for quantification of histologic objects (microvessels [173], biomarker-positive and negative tumor cells [174-177]), evaluation of tissue morphology [178-181], assessment of sampling, and statistical analysis of tissue biomarkers [182-184]. There is ongoing research dedicated to cell culture modeling [185-187]. Few studies to develop and implement cell detection and segmentation methods in histology images have been published [188, 189].

Specifically, TME-related digital pathology studies focused on tumor invasive margin detection and quantitative biomarker assessment in tumor tissue compartments [149, 190, 191].

2.4. Chapter Conclusions

TME-related object segmentation from commonly H&E-stained tissue WSIs produced in routine pathology diagnostics is somewhat neglected in digital pathology.

CNN is at the core of most state-of-the-art methods for solving segmentation and classification problems in digital pathology. While traditional ML is still relevant for the same problems, its usage is somewhat limited because it is applicable to a feature space that needs to be defined by a domain expert. Similarly, CNN can learn predictions from engineered image features, but it has the advantage of learning directly from image data.

FCNN is a special case of CNN that can be considered a state-of-the-art pixel-level segmentation approach based on a literature review. It is relevant to explore FCNN applicability in digital pathology further.

The lack of available high-quality annotated datasets for digital pathology facilitates unsupervised or weekly supervised classification methods. However, unsupervised ANNs have unquestionable shortcomings in terms of decision clarity. In this context, feature engineering is still feasible for specific needs e.g., to enhance decision clarity. The overall process is burdened by the fact that input image data can be produced by different scanning equipment and prepared by a variety of available tissue staining. Therefore, there is a need to explore and apply methods leveraging common pathology practices.

3. ANALYSIS OF ML METHODS FOR EPITHELIUM-STROMA CLASSIFICATION

This chapter explores the segment-based classification of colorectal tumor histology images into two main compartments - tumor epithelium and stroma. The boundary between the tumor epithelium cell-containing tissue compartment and the surrounding stromal tissue defines the TME (as discussed in Chapter 2.2.3). Tumor epithelium-stroma classification is often fine-tuned to adapt to highly specific end-goals of comprehensive pathology research. Therefore, the field holds the capacity for developing new algorithms and analyzing existing methods to precisely classify tumor tissue. This chapter presents an experiment to analyze two competing approaches for tumorous tissue classification by available supervised ML methods - firstly, classification by RDF, SVM, MLP, and a fully connected CNN (deep MLP) classifier by learning from an engineered superpixel feature space, and secondly, classification by CNN by direct learning from image data. The goal is to propose an architecture with better generalization properties.

3.1. Experiment Design

Two matched datasets are generated from H&E stained colorectal tumor tissue WSIs - the dataset of WSI excerpts pre-segmented into superpixels and a dataset of WSI patches produced by cropping out small rectangular image fragments from WSIs. Patch cropping is guided by superpixel centroid coordinates in a WSI image plane. Therefore, the patch dataset exactly matches the superpixel dataset. Additionally, the third dataset is generated by densely sampling image patches around superpixel centroids to explore dataset augmentation's influence on classifier performance. GT for an experiment is acquired by assigning tissue compartment labels to superpixels by an expert, and each cropped patch inherits its corresponding superpixel label.

Feature space for supervised learning is built in a two-step procedure. In the first step, color and image texture descriptors are extracted from tissue class-assigned superpixels. Then dimensionality reduction is applied to factorize image descriptors.

The classification by RDF, SVM, MLP, and deep MLP classifiers is achieved by inferring factorized image descriptor feature space, and classification by CNN is achieved directly from image patches.

In the process of pathology tissue slide production, often complicated manual procedures are involved. Therefore, some amount of variation in slide staining quality is expected. Bearing in mind this fact, to reduce expected inter-slide color variability, grayscale superpixels experimental design is considered. To further analyze classifiers, both superpixel and patch datasets are converted from RGB color to grayscale.

Classifier performance is compared by the area under the ROC curve metrics [192].

3.1.1. Datasets

Images. Three WSIs of H&E-stained colorectal cancer tissues were used (see Figure 3.1). Specimens were produced in the National Center of Pathology, Lithuania. Tumor-containing zones were manually marked by a pathologist on tissue slides directly before scanning. Digital images were captured using the Aperio ScanScope XT Slide Scanner (Aperio Technologies, Vista, CA, USA) under 20× objective magnification.

Superpixels. From each tumor zone in WSIs, a total of 284 RGB tiles of 1,000×2,000 pixels from the highest magnification layers were manually selected for analysis.
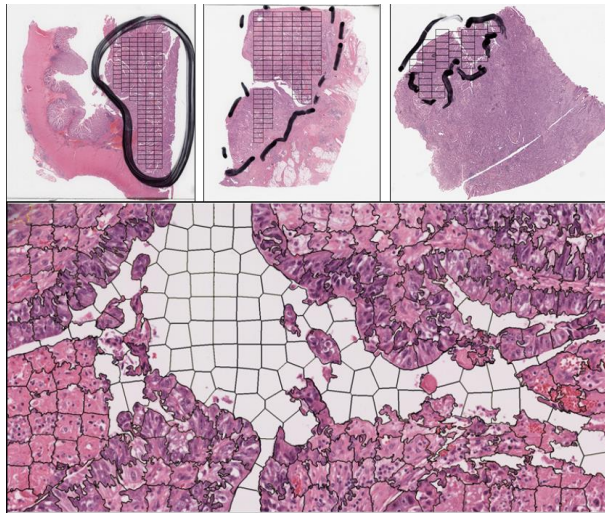

Figure 3.1 Top row: Macro-scale annotated WSIs. Tiles selected for analysis are shown inside tumor-containing areas marked by a pathologist. Bottom row: One segmented tile represents 1,000×2,000 pixels region in WSI.

Consecutively each tile was segmented using the Simple Linear Iterative Clustering (SLIC) algorithm [193] into approximately 350 superpixels (see the bottom row in Fig. 3.1). As an input, SLIC is given the image and a desired number of superpixels to be produced. SLIC returns a single-layer superpixel segmentation mask with a size corresponding to the image plane size, which contains superpixel labels for each pixel of an original image.

All 284 tiles were segmented, and tiles with boundaries between the resulting superpixels highlighted were subjected to micro-scale annotation by the pathologist. Annotation was performed by assigning each superpixel to the tumor (epithelium), stroma, or background classes. The whole process of tissue annotation was strictly limited to superpixel selection and label assignment. No manual outlining/boundary drawing was required. A total of 70,997 superpixels were assigned, whether tumor (epithelium) or stroma class. Background (or otherwise called "glass") is a non-informative part of WSI, so it was removed from all datasets.

Table 3.1 Datasets of superpixels and image patches used. Each data subset corresponds to an individual tumor sample WSI.

Data subset	No. of tiles	Training split		Validation split		Testing split	
		Tumor	Stroma	Tumor	Stroma	Tumor	Stroma
Sample1*	125	10,000	10,000	750	750	9,416	1,205
		Total superpixels/patches: 32,121. Train. / Valid. / Test.: 0.62 / 0.05 / 0.33					
Sample2	125	10,000	10,000	750	750	533	8,699
		Total superpixels/patches: 30,732. Train. / Valid. / Test.: 0.65 / 0.05 / 0.30					
Sample3	34	2,200	2,200	150	150	3,269	175
		Total superpixels/patches: 8,144. Train. / Valid. / Test.: 0.54 / 0.04 / 0.42					
General	284	28,000	28,000	2,000	2,000	7,068	3,929
		Total superpixels/patches: 70,997. Train. / Valid. / Test.: 0.79 / 0.06 / 0.15					

* - used for all ML model's parameter search.

All superpixels mainly representing background could be effectively filtered by the mean and standard deviation of pixel values in a green color channel of a superpixel (background superpixels identified with mean pixel value greater than 190, and standard deviation less than 30 in a green color channel). Also, any multi-class or no-class assigned superpixels were excluded, and the remaining superpixels were used to construct the three subsets corresponding to each tumor WSI (see Table 3.1 *Samples* 1 to 3).

The fourth subset was produced by combining all superpixels from all smaller subsets (ref. Table 3.1 *General* subset). For all data subsets, equal class proportions were maintained in training and validation splits, and the testing split was composed of the remaining superpixels.

Image patches. A dataset of WSI patches was produced by cropping out 72×72 pixel-sized rectangular image patches from WSIs. Patch cropping was guided by superpixel centroid coordinates in a WSI image plane.
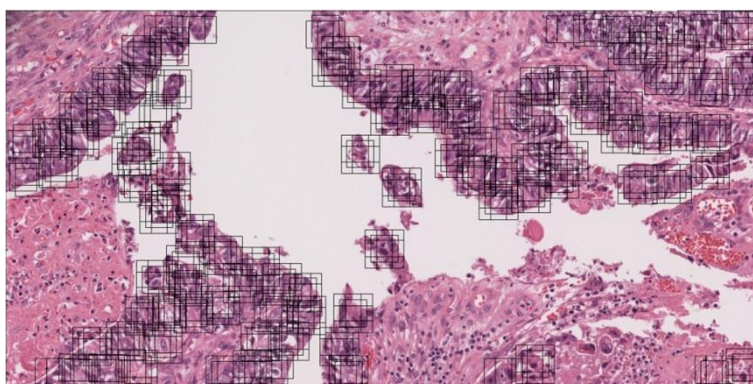

Figure 3.2 Dense sampling of tumor-class patches.

Therefore, the patch dataset used to evaluate CNN classifier performance precisely matches the superpixel dataset (Table 3.1).

Table 3.2 Dataset of densely sampled image patches. Each subset was designed to approximately match Tumor/Stroma class balance in a corresponding subset in the superpixel dataset.

Subset	No. of tiles	Training split		Validation split		Testing split	
		Tumor	**Stroma**	**Tumor**	**Stroma**	**Tumor**	**Stroma**
Dense Sample1*	125	40,000	40,000	25,000	5,000	26,000	6,000
		Total patches: 142,000. Train. / Valid. / Test.: 0.56 / 0.21 / 0.23					
Dense Sample2	125	38,000	38,000	4,000	25,000	4,000	27,000
		Total patches: 136,000. Train. / Valid. / Test.: 0.56 / 0.21 / 0.23					
Dense Sample3	125	10,000	10,000	6,500	1,000	7,500	1,000
		Total patches: 36,000. Train. / Valid. / Test.: 0.56 / 0.21 / 0.24					
Dense General	125	90,000	90,000	40,000	24,000	45,000	25,000
		Total patches: 314,000. Train. / Valid. / Test.: 0.57 / 0.21 / 0.22					

* - used for CNN parameter search.

Additionally, annotated superpixel centroids were used to densely sample data and generate patches for CNN classification on the augmented dataset (given in Table 3.2). Five overlapping 72×72 pixels RGB patches were selected in the original image around each superpixel mass centre by shifting the frame in each of the four directions (0°, 90°, 180°, 270°) by 15 pixels (Figure 3.2).

3.1.2. Superpixel Descriptors

RGB superpixels. Superpixels in each subset were bound in a rectangle minimum bounding box, keeping the three color channels. Pixels inside the bounding box, but outside the superpixel area were assigned zero values in each color channel.

Grayscale superpixels. Superpixels in each subset were bound in a rectangle minimum bounding box. Zero values were assigned to the pixels inside the bounding box, but outside the superpixel area, and converted to grayscale. A color-to-grayscale transformation that retains the Luminance of the original image was chosen. A detailed review of color-to-grayscale transformations frequently used in computer vision emphasizes that Luminance is considered a good choice for texture recognition [194].

Color-based descriptors. For each grayscale superpixel, two statistics were calculated – mean and standard deviation of the pixel value. For an RGB superpixel, eight statistics were calculated – mean and standard deviation of the pixel value for each color channel separately and also all RGB color channels.

Image texture-based descriptors. The texture of a grayscale superpixel has been measured by calculating the spatial gray-level co-occurrence matrix [58] for four directions (at 1 px displacement vector). The 13 directions for an RGB superpixel were used. From each of the resulting co-occurrence matrices, 13 parameters were calculated as follows: angular second moment, contrast, correlation, the sum of squares, inverse difference moment, sum average, sum variance, sum entropy, entropy, difference variance, difference entropy, information measure of correlation 1, and information measure of correlation 2. For each parameter mean value was obtained from all directions, thus resulting in the final 13 descriptors. To extract texture descriptors Python computer vision and image processing library Mahotas [195] was used.

Both the color and texture descriptors calculated for each superpixel were combined to form an array in which rows correspond to superpixels and columns to descriptors.

Dimensionality Reduction and Feature Space. The superpixel dataset (Table 3.1) was subjected to factor analysis (FA). FA was performed as described in [196] with the principal component method using a covariance matrix of Pearson's correlations of the variables. Varimax rotation was applied to simplify the structure of factors for further use of factorized color and texture descriptors in classification tasks. The number of components to be obtained in FA (see Table 3.4) was selected from the principal component analysis [196] and was defined as the number of components explaining more than 99% of the variance in the dataset.

Table 3.4 Number of components retained in FA.

	Color features	Texture features	Combined features
RGB superpixels	4	8	8
Grayscale superpixels	2	8	8

The resulting factor scores were normalized to have zero mean and unit variance per extracted component. Normalized factor scores resulting from color descriptors are referred to as "color features". Similarly, the normalized factor scores resulting from texture descriptors are referred to as "texture features". The "combined features" were produced by combining color and texture descriptors and applying a similar factorization procedure. The normalized factor scores (features) were used as the input data for classification using the ML approaches described in Chapter 3.1.3.

3.1.3. Machine Learning Models

Since background containing superpixels were removed from all datasets (described in Chapter 3.1.1.), thus the epithelium-stroma classification problem can be defined as binary. SVM, RDF, and MLP were implemented using the scikit-learn Python package [197]. Deep MLP and CNN algorithms implemented by the TensorFlow and Keras libraries in Python [198, 199] were employed to solve the classification problem.

The C-Support Vector Classification algorithm (also called type 1 classification SVM) with radial basis function kernel (implementation in the scikit-learn Python package assumes gamma parameter is equal to 1/number

of features) was used [200]. With SVM classification is achieved by constructing hyperplane in multidimensional space to separate instances of different classes. Error minimization is employed in an iterative algorithm to find optimal hyperplane. Nonlinear classification is achieved by using kernel functions of which radial basis function is the most common choice [201].

An RDF classifier is a perturb-and-combine technique specifically designed for classification trees [48]. The principle is based on randomization – a bootstrap sample is drawn from a training set to build each of the trees, and the split on the node is chosen as the best split among a random subset of the features. A predictor of RDF can be selected in a voting procedure or by averaging individual tree probabilistic predictions. Methods that use averaging are known to have relatively high variance due to feature subsetting at the base level. Thus, after classification with RDF, a separate calibration of predicted probabilities was performed as post-processing using the sigmoid method and validation datasets (disjoint data used for training and calibration). In the RDF classifier, 25 estimators (base-level trees) were selected by calibration (no observed significant difference in performance between 25 and 1,000 estimators used) and the maximum number of features to be used with an individual tree was defined to be integer square root of the total number of features. The nodes were expanded until all leaves had at least two samples. All the input samples had equal weight.

MLP is a feedforward neural network (a network whose neurons are connected only in a forward manner to form layers) that is trained by backpropagation [45]. Neurons in the network consist of the linear combiner and an activation function. In the model the rectifier activation function [202] was used – a function whose output is equal to the input if the input is positive, otherwise, the output is set to 0. The network was constituted of one input layer containing inputs corresponding to the features in the dataset, of two hidden layers with 1,000 and 40 neurons respectively, and of an output layer with a single neuron. The number of neurons in hidden layers was selected empirically. Network performance was tested increasing number of neurons in both hidden layers from 100 and 10 up to 1,000 and 40 respectively. Classifier performance was stable among all tested architectures with a mean variation of the area under the receiver operating characteristic curve (AUC) being less than 0.0003. Connections between layers are defined by weights assigned in the learning process, and each neuron in a layer is connected to every neuron in the next layer. In a training phase, an output of the network (a probability matrix instead of discrete

49

predictions) in an iterative manner is compared to GT labels of the input data, and a cross-entropy loss is computed as a negative log-likelihood of a classifier. The model uses the limited-memory Broyden–Fletcher–Goldfarb–Shanno (LBFGS) method to optimize log-loss function with respect to the network parameters as a default optimizer. LBFGS is an optimizer in the family of quasi-Newton methods [203]. The training phase is ended if the validation log-loss is not improving by at least a predefined amount (here 0.0001) for two consecutive iterations, or when a predefined number of iterations (here 200) had been reached.

The deep MLP is a feedforward neural network with multiple hidden layers between the input and output layers that is trained by backpropagation. The basic difference between deep MLP and MLP used in this chapter is that the deep MLP network is constructed of more hidden layers and more neurons per layer. The deep MLP network was constructed with three fully connected layers (with the corresponding number of neurons – 1,024, 512, 128). Neurons in the network use the rectifier activation function (the same as in MLP). Between the last hidden layer and an output layer, a dropout layer was added. Dropout is a regularization technique for reducing overfitting in the model, by omitting a specified proportion (50% in this case) of random neurons output. An output layer has two neurons that use the softmax activation function – a function that given a vector outputs a probability distribution over all possible outcomes (in this case 2 – corresponding to two tissue classes). A number of neurons in all three hidden layers were selected by calibration. The network performance was tested for three configurations regarding the number of neurons in hidden layers (1,024 / 512 / 128, 2,048 / 1,024 / 256 and 5,120 / 2,560 / 640). Classifier performance was stable for both tested architectures with a mean variation of AUC being less than 0.002, therefore the network architecture with the lowest complexity was selected. Log-loss of the model is computed as described in MLP. The network is trained using the adaptive moment estimation (Adam [204]) method with an adjusted learning rate (0.000001) to minimize the cross-entropy loss function. The training phase is ended if the validation log-loss does not improve for ten consecutive iterations, or when a predefined number of iterations (here 200) had been reached.

CNNs are a variation of deep learning neural networks. They employ a local connectivity pattern in the data; thus, weight-sharing between neurons of adjacent layers becomes possible. Every convolutional layer of CNN transforms one volume of activations to another through a differentiable function. Neurons in a layer are only connected to a small

region of the layer before it (a tensor) through a set of weights (a filter) and are distributed along with the depth of a tensor. In a filtering operation the filter is slid over a tensor with a fixed size stride. Filtering inside a layer is a discrete convolution. Thus, the spatial output decreases with each layer. To reduce the number of parameters in the network a pooling operation is employed. Pooling combines the outputs of a group of neurons in one layer into a single neuron in the next layer. The output of the last convolutional layer is flattened and fed into the dense layers of the network. The dense layer or fully connected layer is similar to a hidden layer of an MLP. A relatively simple CNN was constructed to classify image patches. The prostate cancer detection study by Litjens et al. [94] introduced the deep learning techniques to digital pathology employing similar CNN architecture. The model consists of four convolutional layers, one fully connected layer and an output layer with two neurons and a softmax activation function (see Table 3.4). Filter sizes and strides were adjusted to accept 72×72 pixel patches and batch normalization layers were added after each conv2d layer. The Adam method with an adjusted learning rate (0.000001) was used to minimize cross-entropy loss function. The training phase is ended if the validation log-loss is not improving for ten consecutive iterations, or when a predefined number of iterations (here 200) had been reached. The network's width (number of neurons in hidden layers) was selected by calibration (see Table 3.4 for results) by training and evaluation using *Dense Sample1* data subset (see Table 3.2).

Table 3.4 Parameters of CNN tested. Number of feature maps. The best performing model configuration is bolded in the table and was used in further analyses.

Number of neurons in hidden layers					Performance metrics	
conv2d 1	conv2d 2	conv2d 3	conv2d 4	fully connected	Mean AUC	std AUC
32	32	64	64	384	0.9704	0.0007
32	32	64	64	1024	0.9667	0.0005
64	64	128	128	384	0.9726	0.0004
64	64	128	128	1024	0.9687	0.0008
96	**96**	**192**	**192**	**384**	**0.9745**	**0.0003**
96	96	192	192	1024	0.9721	0.0003

Ten iterations were used to train and test CNN, each time randomly assigning the data to the training, validation and testing splits with exactly the same proportions of class labels.

3.2. Results

Typically, classifier prediction is a numeric value on a continuous scale. A class label is produced by comparing a prediction (or a score) to a threshold value. After training ML classifiers on training and validation splits, the testing split was used to evaluate each model performance by calculating AUC. An SVM, RDF, MLP, and deep MLP models were trained and evaluated using color and texture features (factorized descriptors described in Chapter 3.1.2) produced from the superpixel dataset (see Table 3.1). CNN was trained on a matched image patches dataset as well as a densely sampled image patches dataset (see Table 3.2).

Ten iterations were used to train and test all the classifiers, each time randomly assigning the data to the training and testing subsets with the same proportions of class labels. Mean AUC and the standard deviation of AUC were calculated for each of the classifiers. Both RGB and grayscale datasets were used to evaluate ML models. The results are summarized in Tables 3.5 and 3.6.

Superpixel dataset classification. In single *Sample* data subsets, ML classifier results on RGB superpixel features (Table 3.5) range from 0.9095 up to 0.9769 (by AUC). All ML models performed quite similarly - no particular model stands out as exceptionally better than others. However, MLP achieved the best generalization among traditional ML-based classifiers (AUC = 0.9666), also outperforming deep MLP (AUC = 0.9575).

Classification results for grayscale superpixels (Table 3.6) differ more substantially. For these experimental conditions, AUC scores achieved were in a range between 0.5533 and 0.9443. However, this difference was observed between the *Samples* data subsets, but not between the ML models.

Interestingly, data subset size did not affect classifier performance. Contrary to what was expected, classification accuracies on the *Sample3* data subset are comparable to the results of larger data subsets (e.g., the *Sample1* data subset is nearly four-fold larger than *Sample3*) for RGB superpixels (see Table 3.5) and even better for grayscale superpixels (Table 3.6). This finding suggests that individual characteristics of the tissue sample were the cause of the variation in the results.

Table 3.5 Classifier performance of RGB superpixels/patches. Results are given as mean AUC ± standard deviation of AUC acquired in 10 repetitions. Gray background marked cells indicate the best result for each data subset.

RGB	Sample1			Sample2			Sample3			General		
	Color	Combined	Texture	Color	Combined	Texture	Color	Combined	Texture	Color	Combined	Texture
RDF	**0.9453** ±0.0046	0.9413 ±0.0044	0.9095 ±0.0051	0.9609 ±0.0049	**0.9725** ±0.0058	0.9548 ±0.0077	0.9343 ±0.0057	**0.9473** ±0.0067	0.9427 ±0.0055	0.9466 ±0.0023	**0.9533** ±0.0022	0.9385 ±0.0035
SVM	**0.9534** ±0.0040	0.9505 ±0.0045	0.9265 ±0.0035	0.9695 ±0.0042	**0.9769** ±0.0025	0.9620 ±0.0029	0.9441 ±0.0073	**0.9534** ±0.0066	0.9483 ±0.0048	0.9515 ±0.0014	**0.9620** ±0.0024	0.9488 ±0.0021
MLP	**0.9526** ±0.0050	0.9387 ±0.0043	0.9107 ±0.0060	0.9683 ±0.0034	**0.9713** ±0.0039	0.9586 ±0.0040	0.9217 ±0.0071	**0.9333** ±0.0051	0.9282 ±0.0049	0.9577 ±0.0031	**0.9666** ±0.0026	0.9542 ±0.0031
deep MLP	**0.9535** ±0.0049	0.9480 ±0.0042	0.9105 ±0.0055	0.9701 ±0.0114	**0.9764** ±0.0148	0.9629 ±0.0145	0.9320 ±0.0060	**0.9392** ±0.0080	0.9345 ±0.0070	0.9556 ±0.0026	**0.9575** ±0.0019	0.9449 ±0.0040
CNN patches	0.8942 ±0.0067			0.9681 ±0.0028			0.9477 ±0.0093			**0.9895 ±0.0006**		

Table 3.6 Classifier performance of grayscale superpixels/patches. Results are given as mean AUC ± standard deviation of AUC acquired in 10 repetitions. Gray background marked cells indicate the best result for each data subset.

Gray-scale	Sample1			Sample2			Sample3			General		
	Color	Combined	Texture	Color	Combined	Texture	Color	Combined	Texture	Color	Combined	Texture
RDF	0.5533 ±0.0050	0.7748 ±0.0042	**0.7984 ±0.0032**	0.7991 ±0.0040	**0.9267 ±0.0094**	0.9257 ±0.0084	0.7690 ±0.0092	0.9317 ±0.0061	**0.9371 ±0.0062**	0.7083 ±0.0027	0.8553 ±0.0036	**0.8694 ±0.0033**
SVM	0.6457 ±0.0069	0.7958 ±0.0060	**0.8160 ±0.0052**	0.8466 ±0.0039	0.9268 ±0.0021	**0.9351 ±0.0019**	0.8588 ±0.0059	0.9366 ±0.0048	**0.9443 ±0.0043**	0.7817 ±0.0023	0.8688 ±0.0033	**0.8861 ±0.0033**
MLP	0.6507 ±0.0094	0.7614 ±0.0079	**0.7884 ±0.0054**	0.8586 ±0.0036	0.9258 ±0.0061	**0.9275 ±0.0036**	0.8639 ±0.0147	**0.9146 ±0.0043**	0.9140 ±0.0041	0.7967 ±0.0029	0.8765 ±0.0056	**0.8885 ±0.0034**
deep MLP	0.6507 ±0.0042	0.7923 ±0.0053	**0.8049 ±0.0062**	0.8575 ±0.0125	0.9261 ±0.0133	**0.9273 ±0.0222**	0.8668 ±0.0107	**0.9322 ±0.0068**	0.9321 ±0.0074	0.7967 ±0.0030	0.8694 ±0.0043	**0.8777 ±0.0039**
CNN patches	**0.8706±0.0073**			**0.9594±0.0040**			**0.9517±0.0052**			**0.9797±0.0022**		

The nature of the feature space has the largest effect on superpixel classification. Extracted color features proved to be exclusively valuable. For RGB superpixels (see Table 3.5), color or color combined with texture features provide the best results. The best AUC for individual *Samples* data subsets achieved were in the range between 0.9534 and 0.9769 (with AUC = 0.9666 under generalization conditions). Combining color and texture features increased classification accuracy for RGB superpixels (AUC = 0.9666) when compared to color features alone (AUC = 0.9577) or texture features alone (AUC = 0.9542) under generalization conditions.

Grayscale superpixels carry less color information. Therefore, in most cases, texture features of grayscale superpixels allow better classification (AUC in the range between 0.8160 and 0.9443) than color or combined features (see Table 3.6).

The best performance on the *General* data subset was observed with MLP and texture features (AUC = 0.8885), which is substantially lower when compared to the best result of RGB superpixels (with MLP and combined features, AUC = 0.9666). The results align well with results published by other groups for feature space-based ML classifiers: AUC 0.97 – 0.99 [144] and AUC = 0.98 [147] both targeting colorectal cancer, and AUC = 0.98 [91] on prostate cancer images.

Image patch CNN classification. CNN classifier trained on RBG image patches achieved 0.9895 AUC under generalization conditions. This result is comparable to results achieved by other groups for breast cancer (AUC = 0.9316) [95], and prostate cancer (AUC = 0.965 and AUC = 0.99) [91, 94]. Under these experimental conditions, CNN classification accuracy was significantly higher than other ML models trained on RGB superpixel features (AUC = 0.9895 against 0.9533 – 0.9666 achieved with other ML models).

However, for individual *Samples* data subsets CNN did not perform better than other ML models trained on RGB superpixel features (e.g., SVM achieved AUC 0.9534 – 0.9769 and CNN achieved AUC 0.8942 – 0.9681, see Table 3.6).

When trained on grayscale image patches CNN in all cases was more accurate (AUC in the range between 0.8706 and 0.9797) than other ML models trained on grayscale superpixel features (AUC in the range between 0.8160 and 0.9443), but less accurate than CNN trained on RGB patches (AUC in the range between 0.8942 and 0.9895).

Augmentation of the image patches dataset by dense sampling did not significantly improve the classification results. An improvement was observed for the *Sample1* data subset (AUC = 0.9745 for the dense RGB

dataset, AUC = 0.8942 for matched RGB subset; AUC = 0.9338 for the dense grayscale subset, AUC = 0.8706 for matched grayscale subset). However, no improvement was observed for the *Sample2* data subset, and a decrease in classification accuracy was observed for the *Sample3* data subset (AUC = 0.8939 for the densely sampled RGB patches, AUC = 0.9477 for matched RGB patches; AUC = 0.8993 for the densely sampled grayscale patches, AUC = 0.9517 for matched grayscale patches). Dense sampling by shifting around a superpixel centroid might have created an unwanted mixing of the classes. It can again be hypothesized that individual characteristics of the tissue sample were the cause of the variation in the results. This finding is concordant with the observed variation in results regarding the size of superpixels subsets.

3.3. Chapter Conclusions

The tumor tissue classification was approached by annotated superpixel classification using conventional classifiers, and the classification by CNN of patched image data. The following conclusions are drawn:

Superpixel color features allow better classification results (AUC 0.9217 – 0.9701) compared to texture features (AUC 0.9095-0.9629) in all data subsets. Under generalization conditions, combining color and texture features increased the classification accuracy of all ML models on RGB superpixels dataset (AUC = 0.9533 – 0.9666) when compared to color features alone (AUC = 0.9466 – 0.9577) or texture features alone (AUC = 0.9385 – 0.9542).

As expected, CNN achieved the best overall classification generalization (AUC = 0.9895). Interestingly, even when trained on grayscale image patches CNN achieved better generalization (AUC = 0.9797) than other ML models trained on RGB superpixel features (AUC 0.9533 – 0.9666). This suggests that by learning directly from image data CNN can build a diverse feature space in hidden layers of its architecture.

4. METHOD FOR CELL NUCLEI SEGMENTATION WITH LYMPHOCYTE IDENTIFICATION

The previous chapter focused on the identification of two major tumor tissue compartments – tumor epithelium and stroma. This chapter even further explores the H&E-stained tissue WSI analysis, i.e. the detection of lymphocytes – immune cells that often move along tumor compartment margins (TILS – tumor-infiltrating lymphocytes). Lymphocyte segmentation in a set of H&E-stained breast cancer and colorectal cancer tissue images is considered. The motivation to specifically target lymphocytes stems from the fact that lymphocyte segmentation in routine pathology images is a necessary but underresearched topic in digital pathology (reviewed in Chapter 2.2.3).

4.1. Experiment Design

This chapter introduces a model for cell nuclei segmentation. An extension of the FCNN-based state-of-the-art cell segmentation models is considered. The idea of a multiple-resolution image input architecture is adopted from the Micro-Net model [104] and the multi-level interconnected architecture of the U-Net [99] is used as a base model for the segmentation of all types of tissue nuclei. A new structuring element of the network architecture is introduced (named "texture block"). The texture block consists of 2 parallel chains of 3 convolution layers, which enhance image texture extraction. An increase in segmentation performance is expected. The segmentation performance of the proposed model is compared against higher complexity models such as U-Net and Micro-Net.

Additionally, the separation of clumped cell nuclei is considered. An active contour layer is added to the GT images, and the nuclei segmentation model is trained to output both segmented nuclei and the contour of each nucleus. Again, an increase in segmentation performance is expected.

After segmentation, lymphocyte identification in a set of segmented nuclei by an ML-based classification is considered. Classification accuracy, precision, recall, and F1-score of an RDF classifier, MLP, and CNN are compared.

The schema of the proposed method is summarized in Figure 4.1. After careful hyperparameter tuning and model training, the method assumes a trained nuclei segmentation model to accept new images and produce segmentation masks (Fig. 4.1 step 1B). The resulting segmentation masks

are used to crop out detected cell nuclei and feed them into the classifier to discriminate lymphocyte and non-lymphocyte nuclei (Fig. 4.1 step 2B). The complete method to segment and classify lymphocytes (Fig. 4.1 steps 1B→2B) is evaluated on a public dataset.
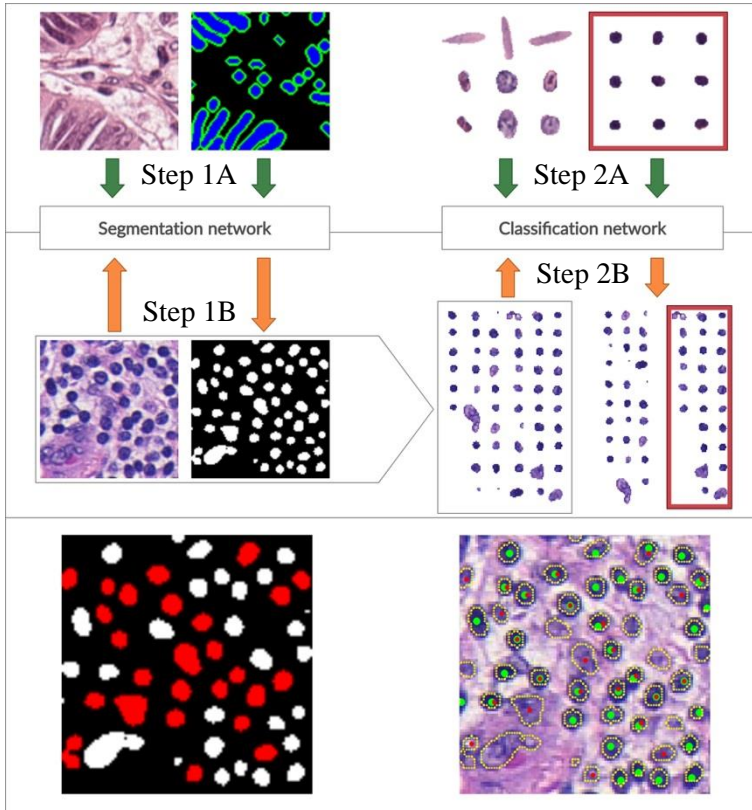

Figure 4.1 Overall schema of the proposed method. In step 1, the segmentation network is trained on original image patches and GT images (step 1A) and used to segment new images (step 1B). In step 2, the classification model is trained (step 2A) on cropped nuclei (produced in step 1B) to discriminate lymphocytes (in the red box) from other nuclei and is used to produce labels for segmented nuclei (step 2B). In the bottom panel, on the left, representative segmentation results are shown (lymphocyte nuclei are colored in red for clarity), and on the right, an original image with detected nuclei contours outlined and detected lymphocyte nuclei depicted with red dots is given. Green dots indicate lymphocyte GT.

4.1.1. Datasets

Images. In this experiment, 4 whole-slide histology sample images prepared with H&E staining were used (2 WSI slides from breast cancer patients and 2 WSIs from colorectal cancer). These slides were produced in the National Center of Pathology, Lithuania (NCP), and digitized with the Aperio ScanScope XT Slide Scanner at 20× magnification. 1 WSI slide was obtained from the TCGA database [205], tile ID: TCGA_AN_A0AM, and used for both segmentation and classification testing.

For the results and approach validation, two additional public collections of annotated histology images were used - the CRCHistoPhenotypes dataset [153] (CRCHP) and the breast cancer dataset [155] (JAN). CRCHP contains 100 H&E-stained colorectal cancer histology images (500×500 pixel-sized excerpts from WSIs) with identified cell nuclei. The CRCHP dataset entails broad cell type categories, where lymphocytes are annotated under the inflammatory label. The JAN dataset consists of 100 H&E-stained breast cancer histology images (100×100 pixel-sized excerpts from WSIs) with only lymphocytes annotated.

All images (both public and private) were acquired using 20× magnification and annotated by an expert pathologist marking lymphocyte nuclei centers.

The described images were used to generate two diverse datasets dedicated to segmentation and classification tasks. Both datasets are summarized in Table 4.1 and Table 4.3 and described in the following paragraphs.

Segmentation dataset. To train and validate the segmentation model, randomly selected 344 tiles of 256×256 pixel size were used. Dataset was split into training and validation sets, respectively. To test the segmentation model, 96 tiles from the breast cancer TCGA slide were produced. Both tiles generated from the TCGA slide and tiles generated from NCP slides were manually annotated. In the annotation process, each cell nucleus present in an image patch was manually outlined, and 2 pixel-wide active contour borders surrounding each nucleus were added as a second layer to the nuclei segmentation masks. Each outlined nucleus was assigned a class label (a lymphocyte or other).

Tiles generated from WSIs (NCP and TCGA) were converted into floating-point data type, and their values were scaled to the unit interval [0, 1] channel-wise. Various image augmentation methods (rotation, flip, transpose, RGB augmentation, brightness adjustment, CLAHE [206]) were

applied to the training set to obtain the final training set of 5,206 images (the techniques used to augment training patches are summarized in Table 4.2).

Table 4.1 Segmentation dataset. Segmentation experiments were performed on 256×256 pixel-sized image patches. BC - breast cancer, CRC - colorectal cancer, NCP - National Center of Pathology, Lithuania, TCGA - The Cancer Genome Atlas database.

Segmentation set	Tumor type	Raw set	Final augmented set	Origin
Training	BC	192	3,648	NCP
	CRC	82	1,558	NCP
	Total	274	5,206	NCP
Validation	BC	54	54	NCP
	CRC	16	16	NCP
	Total	70	70	NCP
Testing	BC	96	96	TCGA
	Total	96	96	TCGA

Table 4.2 Image augmentation techniques and parameters used for training dataset expansion

Augmentation	Parameters
Transposition	-
Rotation axis flipping	Perpendicular rotation angles (90, 180, 270)
CLAHE [206]	Cliplimit = 2.0, tilegridsize = (8, 8)
Brightness adjustment	HSV colorspace, hue layer increased by 30
RGB augmentation	Random pixel value adjustments up to 0.1
RGB2HED color adjustments [207]	Color values adjusted within range [0.02, 0.001, 0.15]

Classification dataset. Manually annotated segmentation masks were used to crop out all types of cell nuclei from raw images. Centroid coordinates were determined for each nucleus in a segmentation mask and a 32×32 pixel-sized image patch centered at the nucleus centroid was cropped from the original image. Pixels of a cropped patch outside the nucleus mask were set to zero. Each nucleus-containing patch inherited a class label (assigned manually to GT in an annotation procedure). Nuclei containing patches were further augmented by rotation and axis flipping. From CRCHP tiles 1,143 nuclei were assigned a lymphocyte class label, and 1,040 nuclei were labeled as the other class.

Table 4.3 Classification dataset. Classification experiments were performed on extracted cell nuclei embedded in blank 32×32 pixel-sized placeholders. BC - breast cancer, CRC - colorectal cancer, NCP - National Center of Pathology, Lithuania, TCGA - The Cancer Genome Atlas database, CRCHP - CRCHistoPhenotypes dataset [153], JAN - the breast cancer dataset [155].

Classification set	Nucleus type	Raw set	Final augmented set	Origin
Training	Lymphocyte nuclei	11,032	50,950	NCP
	Other nuclei	10,922	55,825	
	Total nuclei	21,954	106,775	
Validation	Lymphocyte nuclei	2,588	2,588	NCP
	Other nuclei	2,751	2,751	
	Total nuclei	5,339	5,339	
Testing	BC lymphocytes	903	903	TCGA
	CRC lymphocytes	1,143	1,143	CRCHP
	Total lymphocytes	2,046	2,046	TCGA + CRCHP
	BC other	1,195	1,195	TCGA
	CRC other	1,040	1,040	CRCHP
	Total other	2,235	2,235	TCGA + CRCHP
	Total nuclei	4,281	4,281	TCGA + CRCHP
Evaluation	BC lymphocytes	2,949	2,949	JAN
	BC other	1,921	1,921	
	Total nuclei	4,870	4,870	

4.1.2. Cell Nuclei Segmentation Models

Three FCNN-based models were implemented to achieve segmentation of all types of cell nuclei in H&E-stained images of tumor tissue - the U-Net, the Micro-Net, and the modified U-Net. The proposed nuclei segmentation model architecture is shown in Figure 4.2.
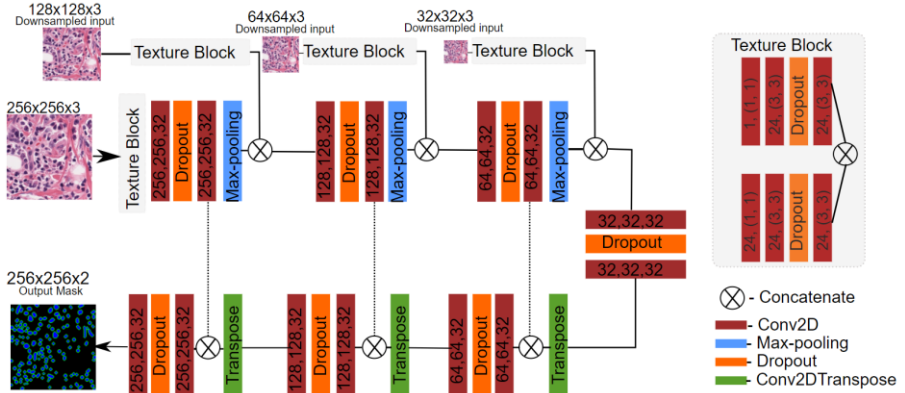

Figure 4.2 The architecture of the modified U-Net model.

The deeply layered architecture of the U-Net leverages skip connections between the many-layered encoder and decoder paths of the network to retain the spatial information of the input. The Micro-Net model further incorporates even additional layers - multiple input image down-sampling layers to compensate for information loss during max pooling. The proposed modification to the U-Net architecture limits encoder and decoder cascade to only 3 levels each consisting of 2 convolution layers (3×3 convolutional filters with stride 2), dropout (dropout rate 0.2), and max-pooling layers. The modification further adopts multiple down-sized image input layers after each max-pooling operation, which were originally proposed in the Micro-Net model [104]. An exponential linear unit (elu, [208]) activation function was used after each convolution layer and sigmoid activation [202] for the output layer.

The most important modification of the U-Net architecture is achieved by introducing a texture block after each image input layer. The texture block is designed to create two parallel flows in the computational graph of the model. One flow of the block is a chain of wide (standard) convolutional layers, and the other flow starts with a single neuron convolutional layer that

is expected to create a bottleneck in the architecture and force the propagation of different convolutional features.

Adam optimizer [204] was used with initial learning rate $lr = 0.001$, which was reduced by factor 0.1 if validation loss did not improve for 4 consecutive epochs (the lower limit of learning rate was set to 1×10^{-6}). Dice coefficient (4.1) in combination with binary cross-entropy loss (4.2) was used to quantify model metrics as a custom loss function (4.3) [209, 210].

$$Dice = \frac{2*TP}{(TP+FP)+(TP+FN)} \qquad (4.1)$$

where TP is true positive, FP is false positive and FN is false negative.

$$L(y,\hat{y}) = -(y * \log(\hat{y}) + (1 - y) * \log(1 - \hat{y})) \qquad (4.2)$$

where y is a binary class label and $\hat{y}$ is predicted probability.

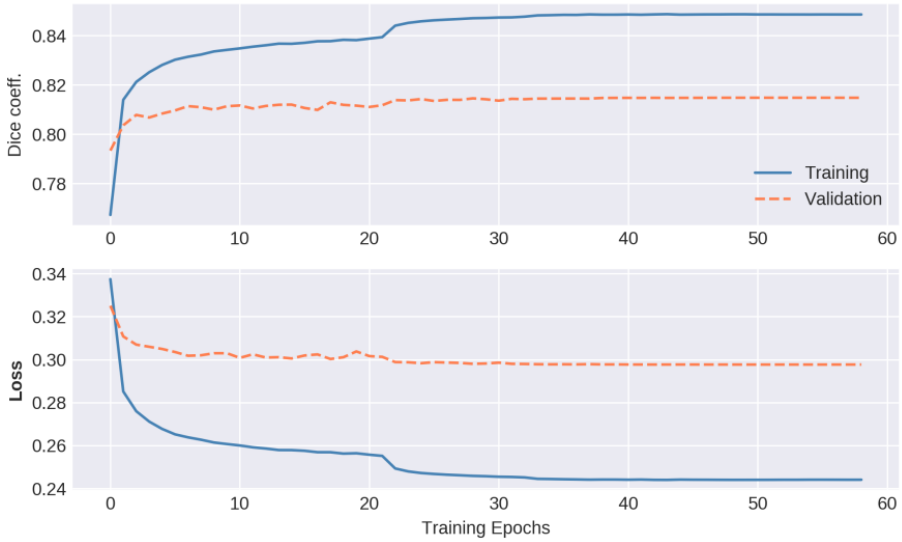$$CrossentropyDiceLoss = 0.1 * L(y,\hat{y}) + 0.9 * (1 - Dice) \qquad (4.3)$$

Figure 4.3 Training of the proposed U-Net architecture.

Model converged after 36 epochs (see Fig. 4.3) using a batch size of 1 (input image dimensions: 256×256×3) for training and validation.

4.1.3. Cell Nuclei Classifiers

The cell nuclei classification problem was approached with RDF, MLP, and CNN classifiers.

RDF was chosen as a baseline ML algorithm. RDF was used with the Gini impurity criterion as split quality measurement and 10 estimators. The RDF classifier was trained on linearized nuclei images (32×32 RGB-colored images linearized to 3,072-length vector), which achieved 0.77 testing accuracy.

The MLP model employed consists of three dense layers (number of nodes: 4096, 2048, 1024), with softmax as the output layer activation function. For each layer, relu activation was used, followed by batch normalization. The dropout layer (dropout rate 0.4) was used in the middle layer instead of batch normalization to avoid model overfitting. Adam optimizer was employed with initial learning rate $lr = 0.001$, which was reduced by factor 0.1 if validation loss did not improve for 6 consecutive epochs (the lower limit of learning rate was set to 1×10^{-6}). Accuracy was used as metrics with binary cross-entropy as a loss function. The model was trained until convergence using 64 and 32 batch sizes for training and validation, respectively.

A CNN consisting of 4 convolutional, 2 max-pooling, and 2 dense layers (see Table 4.7). Additionally, for each layer, relu activation was used, followed by batch normalization. The dropout layer (dropout rate 0.2) was used in between convolutional and dense layers. Adam optimizer was employed with initial learning rate $lr = 0.001$, which was reduced by factor 0.1 if validation loss did not improve for 6 consecutive epochs (the lower limit of learning rate was set to 1×10^{-6}).

Python implementation of the RDF classifier from the sklearn machine learning library [197, 211] was used. Neural network models for nuclei segmentation and cell-type classification were implemented using Tensorflow and Keras machine learning libraries [198] and trained on GeForce GTX 1050 GPU, 16 Gb RAM.

4.2. Results

The calibration of nuclei segmentation model hyperparameters, model training, and model comparison is evaluated by pixel-level (calculated for each pixel in the prediction masks) Dice coefficient, accuracy, precision, recall, and F1-score.

Additionally, in the segmentation experiments, when testing for better separation of touching cell nuclei, object-level (for each segmented object (nucleus) in the prediction masks) accuracy, precision, recall, and F1-score are calculated.

Classifiers (RDF, MLP, and CNN) are compared by classification accuracy, precision, recall, and F1-score.

The complete method to segment and classify lymphocytes is evaluated on a public dataset (JAN, see Table 4.2).

4.2.1. Nuclei Segmentation

Hyperparameter tuning. The optimal model architecture was experimentally evaluated by searching for the best performing hyperparameter combination. Segmentation model hyperparameter space was investigated by changing dropout rates, convolution filters (neurons) per network layer, and activation functions (elu, relu, sigmoid, and softmax). Results of hyperparameter tuning are provided in Table 4.4. Model evaluation was performed by Dice coefficient (4.1), accuracy, precision, recall, and F1-score at a pixel level [212].

Table 4.4 The comparison of nuclei segmentation models by aggregated pixel-level metrics. Each coefficient value was calculated as a mean of individual coefficients for each tile from the testing set. DO - dropout rate, BN - batch normalization, Act func - activation function.

Act func	Output act func	No. of neurons	DO	BN	Dice coefficient	Accuracy per pixel	Precision per pixel	Recall per pixel	F1-score per pixel
U-Net [99]									
−	−	−	−	−	0.78	0.59	0.66	0.84	0.74
Micro-Net model [104]									
−	−	−	−	−	0.79	0.66	0.75	0.85	0.80
Proposed model (modified U-Net)									
elu	**sigmoid**	**16**	**0.2**	**−**	**0.81**	**0.77**	**0.86**	**0.88**	**0.87**
elu	sigmoid	32	0.2	−	0.80	0.77	0.85	0.88	0.87
elu	sigmoid	48	0.2	−	0.80	0.76	0.85	0.87	0.87
elu	sigmoid	16	0.3	−	0.81	0.77	0.86	0.88	0.87
elu	sigmoid	32	0.3	−	0.80	0.76	0.85	0.88	0.87
elu	sigmoid	48	0.3	−	0.80	0.76	0.86	0.87	0.87
elu	sigmoid	32	−	+	0.80	0.74	0.84	0.86	0.85
relu	sigmoid	32	−	+	0.80	0.74	0.84	0.87	0.85
elu	softmax	32	−	+	0.73	0.58	0.63	0.87	0.73
relu	softmax	32	−	+	0.77	0.65	0.72	0.87	0.78

Experiments indicate that expansion of model layer width (16, 32, 48 neurons per convolutional layer) dramatically did not affect the segmentation performance metrics – which suggests that an introduced texture block component may ensure consistent feature extraction in a wide range of model width. Compared to the U-Net model, which reached 0.78 Dice coefficient for the testing dataset, the selected model achieved 0.81 Dice coefficient with lower model complexity.

Model performance speed. Optimal model selection rationale was based on pixel-level testing metrics, and additionally, loading and inference times relative to the original Micro-Net model were evaluated. Since no significant changes were observed between dropout rates, the dropout rate was set to 0.2, and an elu activation and sigmoid output functions with differing layer widths of 16, 32, and 48 kernels were selected. The testing results provided in Table 4.5 indicate that the lowest relative image prediction and model loading time was observed for the segmentation model consisting of 16 neurons per convolutional layer.

Table 4.5 A comparison table of loading and inference speeds of modified U-Net model versions. All times were obtained relative to the original Micro-Net model. The best-performing model is highlighted in bold.

Model	Relative loading time	Relative inference time
Micro-Net	1	1
Custom-16	**0.212**	**0.288**
Custom-32	0.212	0.314
Custom-48	0.268	0.359

Active contour layer. To evaluate the impact of the active contour layer on nuclei separation, a modified U-Net was trained using single-layered nuclei masks and compared the results with an identical model trained on two-layered annotations. During this experiment, the best-scoring model architecture from the hyperparameter search experiment was used.

To reveal the effect of training for nuclei contours on clumped object separation, both pixel-level and object-level metrics were employed. The Dice coefficient (4.1) was used to track pixel-level segmentation performance, while object-level segmentation quality was evaluated by calculating intersection over union (*IoU*), see Equation 4.4 [212, 213].

$$IoU = \frac{TP}{FP+TP+FN} \quad (4.4)$$

66

where TP is true positive, FP is false positive and FN is false negative.

For this comparison, accuracy, precision, recall, and F1-score metrics were calculated at an object level - i.e. only for nuclei having at least 50% of the predicted area overlapped with the GT nuclei mask (at least 0.5 by *IoU*). To prevent the mapping of multiple predicted objects to the same GT nucleus, the GT nucleus mask could only be mapped to a single predicted object.

The modified U-Net training strategy when nuclei segmentation was achieved using masks supplemented with the active contour layer outperformed the model with single-layered masks by all evaluation metrics (both on pixel-level and object-level measurements), as shown in Table 4.6.

Table 4.6 The active contour layer effect on nuclei segmentation performance. For pixel-level segmentation performance, the aggregated Dice coefficient was calculated as a mean of individual coefficients for each tile from the testing set (96 TCGA tiles, see Table 4.1). Object-level segmentation performance was evaluated by accuracy, precision, recall, and F1-score metrics for objects with at least 0.5 overlap between GT and *IoU* prediction.

Mask layers	Dice coefficient	Accuracy per object	Precision per object	Recall per object	F1-score per object
2-layered	**0.81**	**0.75**	**0.85**	**0.86**	**0.85**
1-layered	0.80	0.73	0.84	0.85	0.84

The best performing nuclei segmentation model (based on evaluation results provided in Tables 4.4 and 4.5) was achieved with elu activations in hidden layers of the network, sigmoid activation function in the output layer, 16 neurons per convolutional layer, and 0.2 dropout rate, with 2-layer GT training strategy.

4.2.2. Nuclei Classification

Hyper parameter tuning and model comparison. Model performance metrics were evaluated for several hyperparameter combinations, including a number of nodes per layer, activation functions, and a number of convolutional kernels. Hyperparameter search is summarized in Table 4.7.

Table 4.7 The hyperparameter search results for cell nuclei classifier (mean standard deviation). The model performance was evaluated on the testing set (Testing, see Table 4.3). Mean and standard deviation values were obtained by running each experiment five times.

Models	Accuracy	Precision	Recall	F1-score
Random decision forest				
	0.77±0.0020	0.69±0.0020	0.99±0.0020	0.82±0.0020
Multilayer perceptron				
2,048 / 1,024 / 512	0.78±0.0900	0.71±0.1000	0.99±0.0040	0.83±0.0600
4,096 / 2,048 / 1,024	**0.78±0.0030**	**0.71±0.0300**	**0.99±0.0003**	**0.82±0.0200**
Convolutional neural network				
conv2d: 32 / 32 / 32 / 32 dense: 256 / 64	0.76±0.0900	0.69±0.1000	0.98±0.0040	0.80±0.0600
conv2d: 16 / 16 / 16 / 16 dense: 256 / 64	0.76±0.0900	0.70±0.1000	0.98±0.0040	0.81±0.0600

During experimentations, MLP with 4,096 / 2,048 / 1,024 layer configuration and relu hidden layer activation functions, two batch-normalization layers, a 0.2 dropout rate, and a softmax output activation function achieved the highest testing accuracy score of 0.78 with 0.82, 0.71, and 0.99 F1-score, precision and recall values, respectively.
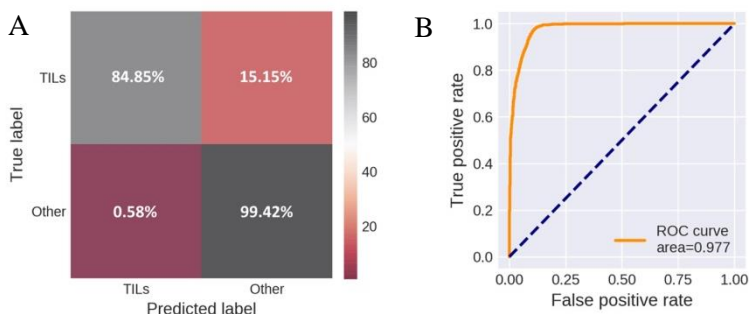

Figure 4.4 The performance metrics of MLP classifier. A - confusion matrix depicting cell nuclei classifier performance on the testing set (true positive lymphocyte predictions and true negatives marked in grey, false predictions – in red), B - ROC curve obtained from nuclei classifier testing data.

The confusion matrix for the MLP classification model demonstrates that out of 2,046 labelled lymphocytes, 310 were falsely misclassified as other cell types, while 13 false-positive observations were registered out of 2,235 nuclei labelled as other cell types as shown in Figure 4.4A.

4.2.3. Workflow Evaluation

The proposed lymphocyte identification method is a two-step algorithm - a nuclei segmentation model (the model with elu activations in hidden layers, sigmoid activation function in the output layer, 32 neurons per convolutional layer, and 0.2 dropout rate trained with 2-layer GT) and segmented nuclei classifier (MLP with 4,096 / 2,048 / 1,024 layer configuration, relu hidden layer activations, two batch-normalization layers, 0.2 dropout rate, and a softmax output activation function).

The proposed lymphocyte identification workflow has been tested on the lymphocyte dataset (JAN). The dataset is composed of 100 breast cancer images (100×100 pixel-sized) stained with H&E and digitized using 20× magnification. The lymphocyte centers were manually annotated by an experienced pathologist. The same dataset was used by other groups [156].

Each testing image was zero-padded to 256×256 pixel input size (to match the input size of the segmentation model) while preserving the original image scale. Each testing slide was first subjected to segment all cell nuclei, followed by nuclei cropping and subsequent classification of each cropped nucleus using MLP for lymphocyte identification. If the nucleus was classified as a lymphocyte, the cell center was marked with a green dot. The classifier's testing results were evaluated using dataset annotations as a reference.

Nuclei segmentation is shown in the second column of Figure 4.5. Nuclei segmentation masks demonstrate consistent cell nuclei detection efficiency regardless of image staining intensity. The confusion matrix in Figure 4.6 A shows a low false-positive lymphocyte misclassification rate. However, relatively high false-negative rate, as well as visual inspection of results suggests that the MLP lymphocyte classification model is sensitive to image stain intensity. This is well reflected in Figure 4.5 unmodified image column, where lymphocyte detection efficiency conspicuously decreases as image staining intensity fades. This is not a surprising result, given that MLP was trained on lymphocytes cropped from histology samples prepared in a different laboratory, where image staining is more consistent across different histology samples. This result illustrates the main limitations of the lymphocyte classification model: cropped nuclei images lose image background information, which otherwise could be leveraged in differentiating nucleus stain intensity versus its background color intensity.
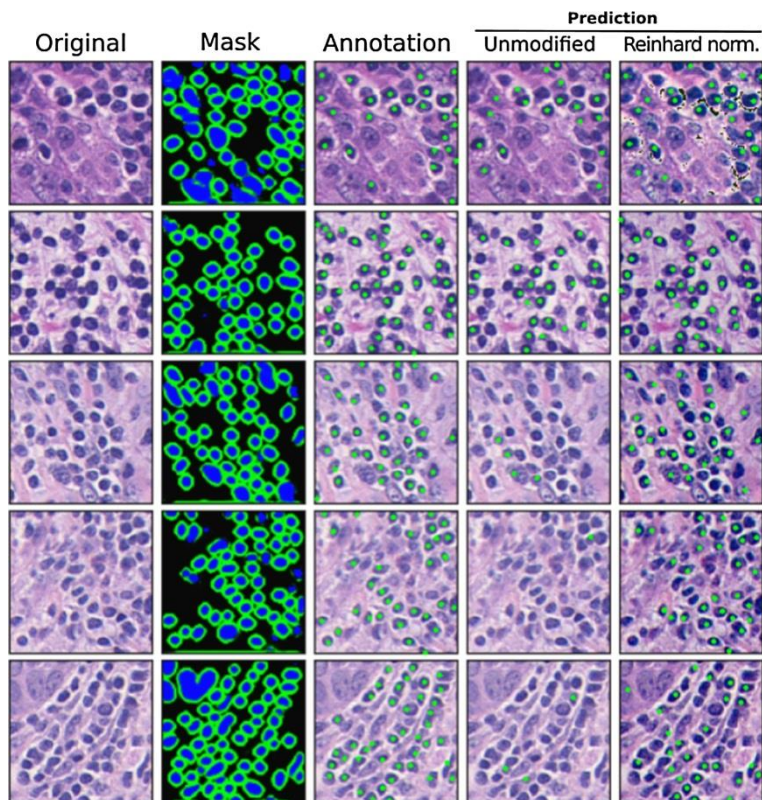
Figure 4.5 Examples of 5 testing images from breast cancer lymphocyte dataset (JAN) with corresponding lymphocyte identification model outputs. From left to right: 1st column- original testing image from the lymphocyte dataset. 2nd column: nuclei segmentation predictions by the modified Micro-Net. 3rd column: expert pathologist's annotation (marked lymphocyte centers) supplied in the dataset. 4th column: MLP lymphocyte classifier result (if the nucleus was predicted as a lymphocyte, its center was labelled with a green dot). 5th column: lymphocyte classifier results after the Reinhard [214] stain normalization.

The effect of color normalization on overall model performance. To address high staining variability between different histological samples, the lymphocyte testing dataset was normalized using the Reinhard stain normalization method. The Reinhard algorithm adjusts the source image's color distribution to the color distribution of the target image by equalizing the mean and standard deviation pixel values in each channel [214].

$$l_{mapped} = \frac{l_{original} - \bar{l}_{original}}{\hat{l}_{original}} \hat{l}_{target} + \bar{l}_{target} \quad (4.5)$$

$$\alpha_{mapped} = \frac{\alpha_{original} - \bar{\alpha}_{original}}{\hat{\alpha}_{original}} \hat{\alpha}_{target} + \bar{\alpha}_{target} \quad (4.6)$$

$$\beta_{mapped} = \frac{\beta_{original} - \bar{\beta}_{original}}{\hat{\beta}_{original}} \hat{\beta}_{target} + \bar{\beta}_{target} \quad (4.7)$$

where l, α, β are color channels in LAB colorspace, $\hat{l}, \hat{\alpha}, \hat{\beta}$ means standard deviation, $\bar{l}, \bar{\alpha}, \bar{\beta}$ stands for a mean value of all pixel values from the channel. The color normalization algorithm was implemented using openCV and Numpy python libraries [215] using representatively stained images from the training dataset as the target for stain normalization.
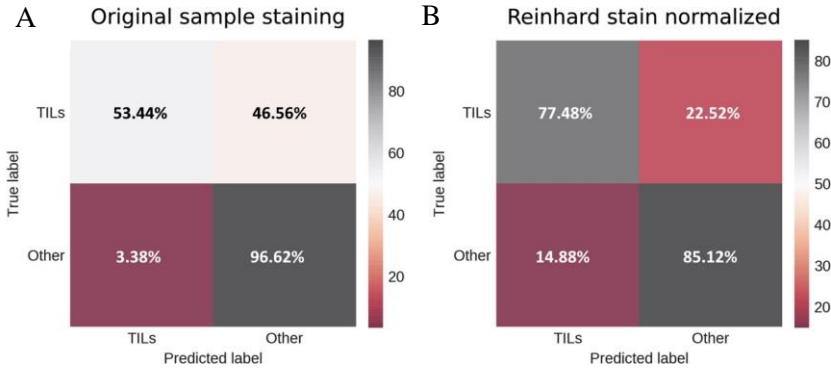

Figure 4.6 Testing metrics for breast cancer lymphocyte dataset. A: confusion matrix for testing images with original sample staining; B: confusion matrix for testing images with Reinhard stain normalization applied on image stain.

Stain normalization effect on cell lymphocyte detection was evaluated by comparing testing metrics before stain normalization and after Reinhard algorithm implementation. The confusion matrix in Figure 4.6B indicates a lower false-negative rate for lymphocytes. Stain normalization increased accuracy, precision, recall, and F1-score values by approximately 10%, as shown in Table 4.8. These results indicate that the stain normalization step is an effective pre-processing part that can mitigate high staining intensity variance between histology samples. Observed improvement of lymphocyte classification accuracy by applied relatively simple Reinhard stain normalization suggests this part of the workflow can be further explored.

Table 4.8 A comparison table depicting the effect of stain normalization on lymphocyte identification efficiency is presented. For comparison, we give here the results of the studies that utilized the same dataset. It is important to note that we only used this dataset to test our method, while studies referenced in the table used part of this dataset for training as well.

	Accuracy	Precision	Recall	F1-score
Proposed method, original staining	0.71	0.76	0.75	0.70
Proposed method, wt stain normalization	0.81	0.80	0.81	0.80
Janowczyk and Madabhushi (2016) [155]	–	0.89	–	0.90
Alom et al. (2019) [156]	0.90	–	–	0.91

Both previous studies used the same dataset to train and evaluate their proposed models; therefore, to deal with overfitting, authors had to apply some sort of cross-validation. 5-fold cross-validation was used by Janowczyk [155], and Alom [156] reserved 10% of the dataset for testing purposes. In contrast, in this experiment, the whole dataset was used exclusively for the proposed model evaluation. The achieved result (F1-score = 0.80) indicates good model generalization and comparable performance to both the above-mentioned methods.

4.3. Chapter Conclusions

An end-to-end DL-based method was proposed for cell nuclei segmentation and consecutive lymphocyte identification in H&E-stained breast and colorectal cancer WSIs. The suggested method shows good generalization properties. Conducted experiments suggest that:

The proposed FCNN structural component – convolutional texture blocks – can achieve Dice nuclei segmentation score similar to state-of-the-art models. The proposed model achieved a 1% higher testing Dice coefficient with lower model complexity. Moreover, an additional active contour layer in nuclei annotation masks increases both pixel-level nuclei segmentation performance (Dice coefficient with an active contour – 0.81, and 0.80 without) as well as object-level performance (F1-score with an active contour 0.85, and 0.84 without).

The proposed method achieves lymphocyte detection accuracy of 0.78 on the private dataset (TCGA+CRCHP), and 0.71 on the public dataset (0.81 with Reinhard stain normalization) which is comparable to the state-of-the-

art lymphocyte detection methods. The achieved result indicates good model generalization properties by providing lymphocyte segmentation capability as well.

5. COLLAGEN FRAMEWORK SEGMENTATION

This chapter explores the segmentation of collagen fibers from routine bright-field histology images of breast tumor tissue by an FCNN-based model. Collagen is the third TME compartment addressed in this thesis. Being a fundamental component of TME with massive potential in solid tumor diagnostics (as discussed in Chapter 2.2.3) collagen lacks assessment methods that would not heavily rely on specialized and expensive imaging techniques to the best of our knowledge. This fact inspires and motivates the development of a robust and affordable method for assessing biological information of collagen architecture from readily available bright-field microscopy images (routinely used in diagnostic pathology laboratories all over the world). Due to its complex structure and the abundance in the connective tissue, fibrous collagen is quite challenging to annotate by outlining manually. It is even complicated to define collagen as a target for segmentation tasks. Therefore this experiment utilizes another commonly used pathologic tissue staining method - Sirius Red (SR) to highlight collagen in breast tumor tissues. The knowledge gained in this experiment will be applied in Chapter 6 to further explore and test collagen segmentation on routine H&E-stained tumor tissue WSIs.

5.1. Experiment Design

The first task addressed in this chapter is the generation of ground truth for collagen segmentation. A set of 116 non-overlapping 256×256 pixel-sized image patches is randomly generated from 48 tumor images and subjected to expert annotation. GT is obtained from three different sources (fully manual and semi-automated). Human visual bias is revealed by Bland-Altman difference analysis [216, 217], and the consensual information in acquired GT is captured by the histogram of oriented gradients (HOG [218]).

To address the collagen segmentation task, U-Net is chosen as a base model. The fibrous tissue collagen structure forms distinctive textural patterns; therefore, to better capture mesh-like collagen, the U-Net architecture is modified by introducing the texture block (described in Chapter 4.1.2, also see Figure 4.2). Three models are trained on annotated image patches to segment collagen fibers in the entire collection of 92 tumorous tissue images. The effect of different model training modes on segmentation accuracy is evaluated by intersection, coverage, and ratio analysis [209]). Subsequently, features of collagen fiber morphometry,

density, orientation, texture, and fractal characteristics are defined and extracted from collagen segmentation maps (CSM). To gain an understanding of the general properties of collagen framework architecture, factor analysis [196] is performed.

Univariate prognostic modeling (Kaplan-Meier estimates [219]) is applied to reveal collagen fiber features indicative of patient prognosis. One-way ANOVA and Tukey's HSD post hoc test [220] are employed to uncover significant associations between collagen fiber features and tumor histology groups.

Finally, prognostic models for collagen fiber features (derived by each differently trained FCNN model) are obtained in multivariate Cox regression analysis [221], and significant and independent collagen features are identified as prognostic indicators.

5.1.1. Datasets

Patients. The Lithuanian Bioethics Committee approved this study (reference number: 40, date 2007-04-26, updated 2017-09-12).

Two hundred three patients involved in this and previous studies [175, 176] underwent surgery during 2007-2009 at the National Cancer Institute (Lithuania, Vilnius). During this period, tumor samples were collected prospectively, and the pathologist's examination of these samples was performed at the National Centre of Pathology (Lithuania, Vilnius). One hundred seven patients were diagnosed with an early-stage hormone receptor-positive invasive ductal breast carcinoma.

Samples. Tumor tissue samples from 92 patients were used for the analyses. Clinicopathological characteristics and follow-up data from these patients are reported as the mean and median values for continuous variables and the frequencies of categorical variables and are given in Table 5.1. Patients in this group were females at the age of 27 to 87 years followed for a period of 17 to 121 months after surgery. Hormone receptor positivity was defined previously [176] as estrogen receptor or progesterone receptor immunohistochemical positivity in at least 1% of tumor cells.
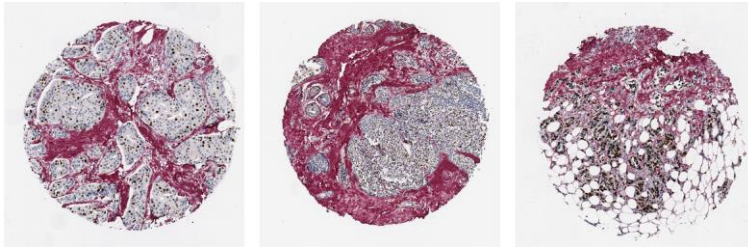
Figure 5.1 Tissue microarray (TMA) samples (each TMA spot has a 1mm diameter).

Table 5.1 Characteristics of patients with hormone receptor-positive breast carcinoma.

Clinicopathological parameters	Patients (%)
Total	92 (100%)
Age, years	
Mean	57.27
Median	59
Range	27-87
Gender	
Female	92 (100%)
Male	0 (0%)
Histological grade (G)	
G1	19 (20.65%)
G2	44 (47.83%)
G3	29 (31.52%)
Tumor invasion stage (T)	
T1	52 (56.52%)
T2	40 (43.48%)
T3	0 (0%)
T4	0 (0%)
Lymph node metastasis status (N)	
N0	48 (51.17%)
N1	30 (32.61%)
N2	11 (11.83%)
N3	3 (3.26%)
Intrinsic subtype	
Luminal A	49 (53.26%)
Luminal B, HER2 negative	26 (28.26%)
Luminal B, HER2 possitive	17 (18.48%)

Tissue microarray (TMA) samples (1 mm diameter spot per patient) randomly selected in intratumoral regions were used for the study. Ki67 immunohistochemistry slides were additionally stained with 0.1% Sirius Red in Picric acid. Images of single TMA cores were extracted from whole-slide images (scanned at 20x objective magnification) and centered in a 2,800×2,800 pixel image for further analysis (see Figure 5.1).

5.1.2. Generation of Ground Truth Masks

A set of 116 non-overlapping 256×256 pixel-sized image patches (see Figure 5.2) was randomly generated from 48 patient TMA images and subjected to expert annotation.
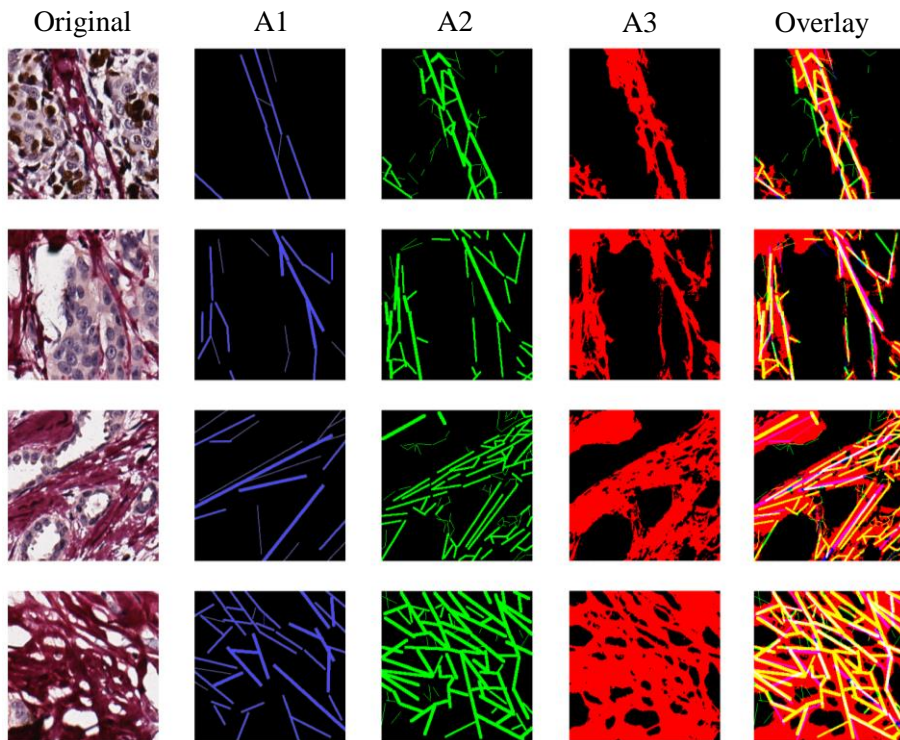

Figure 5.2. Examples of image annotation by different methods. The leftmost column contains 256×256 sized image patches of SR-stained breast carcinoma tissue, followed by binary annotation masks - low detail manual (A1), high detail manual (A2), semi-automated (A3). Annotations are colorized for better appreciation. The rightmost column contains combined annotations to provide a visual impression of agreement.

Two professionals, blinded to each other, were asked to give a rough estimation of the collagen structure motifs during the annotation process. The experts could place a set of straight lines of varying thickness on parts of image patches to capture the direction of collagen fibers (see Figure 5.2 columns A1 and A2). As an alternative, the third set of annotations was generated by image thresholding, followed by manual curation (see Figure 5.2 column A3). Augmentation transformations to annotated images, including horizontal and vertical flips, rotations by 90, 180, 270 degrees, were applied to expand the training image dataset to 696 patches.

5.1.3. Modified U-Net Model for Collagen Segmentation

Network architecture. ANN employed in this study is a fully convolutional encoder-decoder network U-Net developed for biomedical image segmentation [99]. This network architecture supports the pixel-level localization of detected objects by concatenating compact encoded feature maps with corresponding sparse decoded features at multiple scales inside the network's hidden layers. The original U-Net architecture was modified to accept input images of 256×256 pixels size. Rectified linear units in convolutional layers were substituted with exponential linear units and the input's padding was used to ensure that the output has the same shape as the original input. The network was composed of 64 convolutional layers, including five transposed convolutions in the up-sampling path. The last convolutional layer (output layer) maps the feature space of the final layer on the up-sampling path to a single class probability image representation via 1×1 convolution followed by a sigmoid activation function.

The texture block. An additional block was introduced to the original U-Net architecture (also discussed in Chapter 4.1.2, Figure 4.2). The block receives a tensor from the previous layer and passes it down the computational graph in two parallel flows, each composed of three 2D convolutional layers and one dropout layer. In its first internal layer, one flow has a single channel 2D convolution – a bottle-neck, and the parallel flow has a multichannel 2D convolution – an expansion layer. Output tensors from both flows have an identical shape; thus, after concatenation, they contribute equally to the network in terms of feature maps. These texture blocks are placed on the network's encoder path, after each max-pooling layer. The detailed model scheme is given in Figure 5.3.
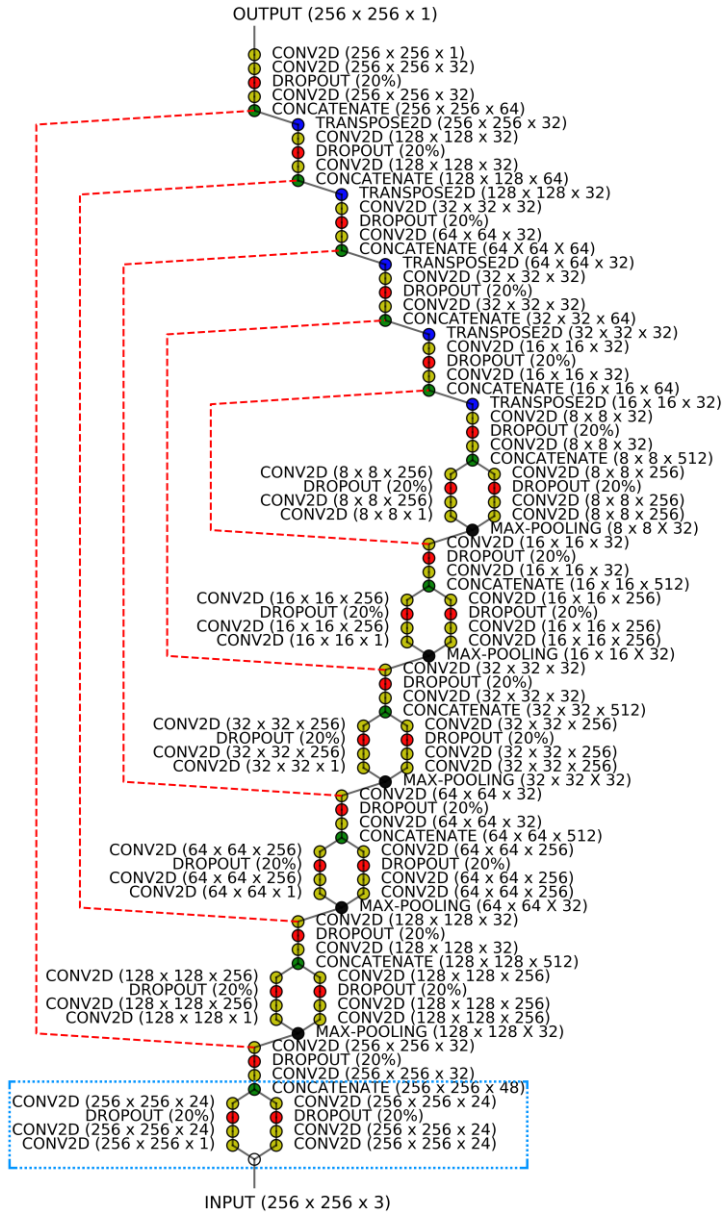
Figure 5.3 Detailed architecture of ANN. The network is a modified U-Net architecture composed of 58 multichannel convolutional layers (with 3×3 filters and relu activations), 23 dropout layers (set to randomly ignore 20% of outputs), 5 max-pooling layers (with 2×2 filters), 5 transposed convolution layers (with 2×2 filters), and a single-channeled convolutional layer (with 1×1 filters and sigmoid activation) for output. The first texture block on the encoder path is framed by a blue-dotted line.

79

Training the model. To minimize the binary cross-entropy loss function, the network was trained with adaptive moment estimation using default parameters provided in the original method [204]. The model trained on single patch batches, and the dataset of annotated patches (see Table 5.2) was split into training subset (80%) and validation subset (20%). The algorithm was set to save model weights after each improvement in validation loss, and terminate the training phase after validation loss did not improve for 20 consecutive epochs. FCNN was expected to learn the representation of human visual perception.
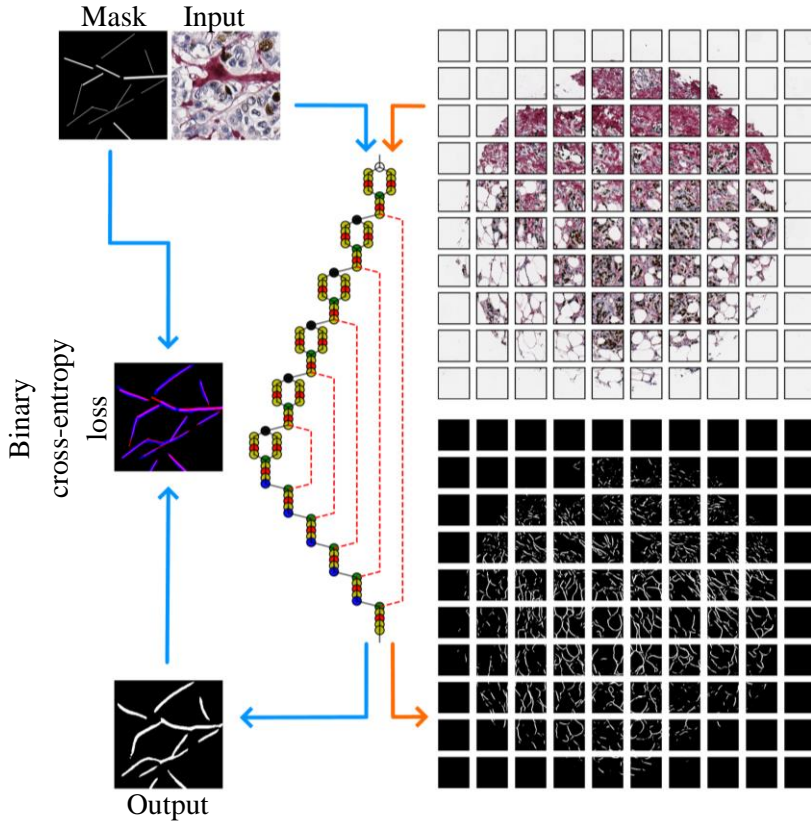

Figure 5.4 Principal workflow design. The modified U-Net (in the middle) is trained on annotated image patches. Training is guided by a binary cross-entropy loss and is evaluated by mean *IoU*. The training phase is indicated by blue arrows. When the training phase is over, the model accepts new images and produces segmentation masks. The testing phase is indicated by orange arrows.

Table 5.2 Three collagen segmentation models were trained on sets of different expert-provided annotations.

Model	Training images (256×256 pixel size)	Ground truth (256×256 pixel size)
M1	696 augmented (flip, rotation) image patches (see Figure 5.2 Original) 556 patches used for training 140 patches used for validation	696 low detail manual annotation masks (see Figure 5.2 A1)
M2		696 high detail manual annotation masks (see Figure 5.2 A2)
M3		696 semi-automated annotation masks (see Figure 5.2 A3)

Principle of collagen framework detection by a neural network. An overview of the workflow is given in Figure 5.4. To fit the model input shape, the TMA image is split into overlapping (128-pixel step-size in vertical and horizontal directions on an image plane) 256×256 pixel size patches. The trained model performs predictions patch-by-patch to produce probability maps that, in turn, are subjected to thresholding. Each pixel in a probability map receives a value of 1.0 if the probability of detecting collagen in that pixel is higher than 0.5. Otherwise, the pixel receives a value of 0.0

To avoid prediction artifacts at patch borders, predictions were taken into account only when present in both overlapping resulting patch analysis probability maps. The results were merged to form a binary collagen segmentation mask (CSM) of an original image of a single TMA spot. Lastly, the size filtering of detected objects was applied removing objects containing less than 50 pixels.

Model evaluation. During the training phase, model progress was monitored by prediction-annotation similarity. An intersection over union (*IoU*, see equation 4.4) metrics was employed.

For pairwise comparison of CSMs produced by different ANN models, similarity was aggregated as a mean ratio of non-zero pixel counts between CSMs, mean coverage, and mean *IoU* of all analyzed CSMs:

$$mean_{ratio} = \frac{1}{N} \sum_{i=1}^{N} \frac{CSM_{i,mod1}}{CSM_{i,mod2}} \ ,$$

$$mean\_coverage = \frac{1}{N} \sum_{i=1}^{N} \frac{CSM_{i,mod1} \cap CSM_{i,mod2}}{CSM_{i,mod1}} \ ,$$

$$mean\_IoU = \frac{1}{N} \sum_{i=1}^{N} \frac{CSM_{i,mod1} \bigcap CSM_{i,mod2}}{CSM_{i,mod1} \bigcup CSM_{i,mod2}}$$

where N is the number of images compared, and mod_i is an individually trained modified U-Net model.

Since no GT was available at a full image level, visual estimation of consensual information in segmentation masks resulting from different models was considered.

5.1.4. Collagen Fiber Morphometry

Quantitative feature extraction. The collagen fibers were analyzed by computing 37 features that fall into three major groups: pixel-level features such as angle and magnitude of the orientation of edges present in an area surrounding a pixel in CSM; fiber-level features include morphometric measures of each detected object (individual collagen fiber); image-level features such as fractal characteristics and texture descriptors of the pixel-level feature representation images. Since the study used a single TMA core image per patient, all image-level features also represent the single patient. Fiber-level and pixel-level features were extracted and aggregated by the mean, median, or standard deviation for each patient (see Table 5.3).

Pixel-level features. Fiber orientation features for each pixel in the target image were measured by a histogram of oriented gradients (HOG [218]). A bounding box (context area) of 18×18 pixels size for a pixel of interest was selected by calibration. Unsigned gradients (originating from edges present in an image) were summarized in 64 evenly spread histogram bins covering a range of 0 – 180 degree angles. A Sobel operator [222] was used in both x and y directions in an image plane to estimate gradients present in an image. HOG procedure then counts occurrences of gradient orientation in image patches and assigns the gradient magnitude of each pixel to the corresponding histogram bin covering a particular angle. Collagen framework orientation angle descriptors were summarized by the linear directional mean, circular variance, and circular standard deviation from the histogram. Since the fiber orientation angle is dependent upon tissue placement on the glass slide, the only meaningful fiber orientation angle related feature at the image level was the circular standard deviation (CSD, see Table 5.3). The magnitude of gradients was summarized by the mean and standard deviation (for histogram values where magnitude was not zero).

Table 5.3 Feature list.

Orientation (pixel-level features)		
LDM	Linear directional mean	
CV	Circular variance	
CSD	Circular standard deviation	
mMag	Mean magnitude	
stdMag	Standard deviation of the magnitude	
Morphometry (fiber-level features)		
mFL		Mean
mdFL	Length	Median
stdFL		Standard deviation
mFP		Mean
mdFP	Path	Median
stdFP		Standard deviation
mFS		Mean
mdFS	Straightness	Median
stdFS		Standard deviation
mFW		Mean
mdFW	Width	Median
stdFW		Standard deviation
Density (fiber-level features)		
FD	Density	Number of pixels in the mask
nENDP	Number of endpoints	
mD		Mean
mdD	Distance between endpoints	Median
stdD		Standard deviation
Texture (image-level features)		
Energy		
Contrast		
Correlation		
Inertia		
Homogeneity		
Sum average		
Sum variance		
Sum entropy		
Entropy		
Difference variance		
Difference entropy		
Informational measure of correlation 1		
Informational measure of correlation 2		
Fractal (image-level features)		
Fractal dimension		
Lacunarity		

Fiber-level features. Morphometric features of collagen fibers were computed treating each fiber as a separate object and subsequently aggregated for each patient by mean values. Fiber objects were bound in a minimum bounding rectangle, and a diagonal of this rectangle was used as a fiber length (FL) measure. The length of a fiber centerline, or the fiber path (FP - defined as a line that divides a fiber into two equal parts along its longer axis), was calculated as half of the total number of points in a fiber contour. The fiber width (FW) was computed as half the Euclidean distance between all opposing pairs of points in the fiber contour aggregated by the median. Fiber straightness (FS) was calculated as a ratio of FL over FP. Fiber density (FD) was computed as a mean Euclidean distance from each detected fiber endpoint to all neighbor endpoints in CSM.

Image-level features. Fractal characteristics and texture features of the collagen framework were computed from CSMs. Box counting procedure [223] was employed to compute the fractal dimension and the lacunarity. The spatial gray-level co-occurrence matrix calculated with a 1px displacement vector was used to derive image texture descriptors [58], including energy, contrast, homogeneity, and entropy. To extract texture descriptors Python computer vision and image processing library Mahotas [195] was used.

Statistical analysis. The consistency of expert annotations was evaluated by Bland-Altman difference analysis [216], a one-sample *t*-test on differences against the zero value, and an independent sample *t*-test on cases in a 95% agreement interval. In an exploratory analysis, Shapiro–Wilk and Levene's tests were used for data normality and homogeneity assumptions. One-way ANOVA and Tukey's HSD post hoc tests [220] were employed to assess differences between group means. FA was performed as described in [196] - with the principal component method using a covariance matrix of Pearson's correlations of the variables. Varimax rotation was applied to simplify the structure of factors and improve the interpretation. Cutoff points for variables were determined, and patients were stratified into groups based on statistical differences as assessed by a log-rank test. Kaplan-Meier estimates [219] were used to assess patient survival. Feature validation was performed following a leave-one-out strategy, as described previously [224]. Cox proportional hazards analysis [221] was applied to model the effect of multiple variables on patients' survival time. For all tests to prove the significance a *p*-value <0.05 was accepted.

Implementation. For DL TensorFlow framework in Python was used [198]. Full training (training from scratch) of the model was performed on a high-performance graphical processing unit (Nvidia GeForce GTX1080).

Feature extraction and quantification were implemented using the scikit-image image processing library in Python [225].

All statistical analyses were performed in the R statistical environment. The Cutoff Finder algorithm [226] was applied for univariate survival analysis and a survival package [227] for multivariate statistical modeling.

5.2. Results

Expert annotation consistency. Regions containing fibrous collagen can be appreciated visually in SR-stained bright-field microscopy images; also, the histogram of oriented gradients procedure enables reliable detection of the fiber orientation (see Figure 5.5).
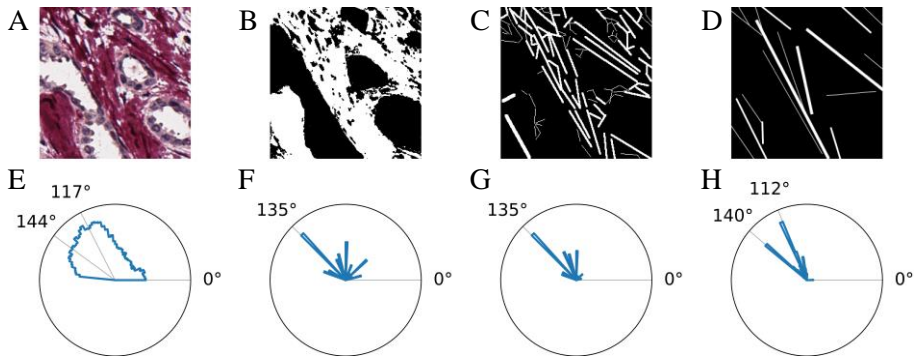

Figure 5.5 Annotation consistency. (A) SR stained breast carcinoma tissue. 256×256 pixel-sized excerpt from original image. (B) binary annotation mask produced by a semi-automated method. (C and D) binary annotation masks (of the same image patch) produced manually. (E, F, G, H) polar projections of histograms of orientations captured by HOG procedure from corresponding (A, B, C, D) images. Note that all annotations differ by the level of detail but basically agree on orientation.

The consistency of the collagen framework annotation procedure was evaluated by Bland-Altman difference analysis [216, 217] of the two "manual" approaches focusing on differences in the count of annotated objects, average object size (in pixels), and the dominant orientation of annotated objects (in degrees).

Table 5.4 Annotation consistency between experts

	Parameters of annotated objects		
	Count	Size	Orientation
Mean difference	-25.303	151.485	2.184
One-sample *t*-statistics	-13.860	5.718	2.052
p-value	7.914×10^{-25}	1.170×10^{-7}	0.043
95% limits of agreement	± 35.423	± 514.076	± 20.652
Independent sample *t*-statistics	-13.603	6.897	0.4851
p-value	1.059×10^{-29}	7.641×10^{-11}	0.628

The analysis revealed significant differences in the level of detail the experts put into their annotations, as well as the orientation of marked objects. The one-sample *t*-test on differences against the zero value shows the presence of fixed bias for all parameters evaluated (*p*-value >0.05 for all estimates). However, in the 95% agreement interval, the differences in annotation orientations are not significant (*p*-value = 0.628, see Table 5.4).
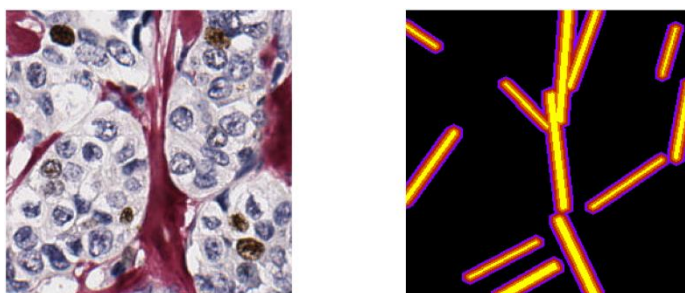

Figure 5.6 Annotation dilation. A different amount of morphological image dilation was applied to annotation masks using a 5×5 elliptic structuring element (number of dilation iterations *nits* = 1, 2, 3). On the left, nondilated annotations are colored in yellow and every additional dilation iteration gets a different color.

Model prediction consistency. Before training, different morphological image dilation amounts were applied to annotated patches using 5×5 square kernel (number of iterations - *nits* = 0, 1, 2, 3 see Figure 5.6). The impact of dilation on model predictions was analyzed by visual comparison as well as by ratio of areas, intersection and coverage. When raw annotations were used (*nits* = 0), models did not produce meaningful results (by visual assessment), except for M3. Annotation dilation did not affect M3 but

significantly pushed M1 and M2 towards M3, and each other. By varying the amount of dilation, it was possible to reach a model agreement over 0.6 for M3 versus M2, 0.5 for M3 versus M1, and 0.4 for M2 versus M1 (as evaluated by mean *IoU*, see Figure 5.7 B). With an increasing amount of dilation, CSMs from M2 even outgrow those from M3 by area (reaching a mean ratio of 1.17, Figure 5.7 A) but target different parts of test images because mean coverage drops below 80% (Figure 5.7 C). Mean coverage analysis quantifies the proportion of one CSM incorporated in the other. In this context, M1 is included in both M2 and M3 to a great extent (over 95%).
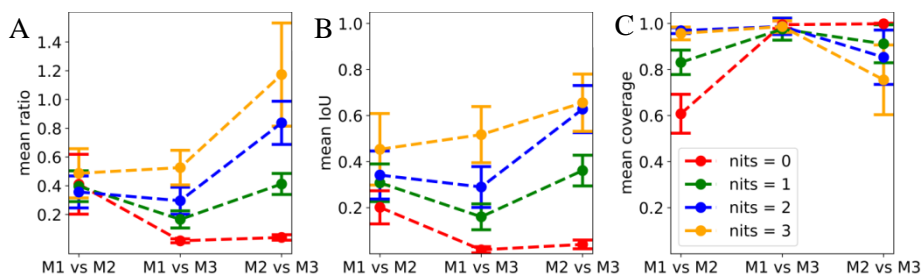

Figure 5.7 Segmentation consistency between trained ANNs. The agreement between CSMs from different models was measured by the ratio of areas, intersection over union, and coverage. Error bars represent standard deviation, and the points are connected to better visualize the trend.

Visual motifs of the predicted collagen framework. On the largest scale, the predicted collagen framework resembles a web-like structure. While CSMs from the M3 ANN model mostly capture bulk collagen, those from M1 and M2 are composed of disconnected structural elements that vary greatly in number and appearance. The smallest components of the framework (typically in CSMs of M1) arise from tissue image parts containing fragmented, fibrous stroma. Most often, these fiber-like objects are present in highly cellular tumor samples and are of simple geometry, scattered, and disconnected from the larger structures.. Fibers spanning sparse intercellular space appear longer and tend to curve around cell islets. Longer fibers extend through regions of well-defined oriented collagen despite SR staining intensity. In CSMs from M1 and M2, intense staining often yields few, relatively short, and disordered branches. In contrast, fibrotic stroma regions yield notably longer fibers. In fibrosis, we can observe fibers branching, merging, and forming loops – these dense and more complex structures form fiber bundles – homogeneous motifs of long, parallel, interconnected branches, outlining large clusters of neoplastic cells

(well represented in CSMs from all models, see Fig. 5.8). In most extreme cases, fibers bundle into complex textures, almost complete circles, mesh-like structures.
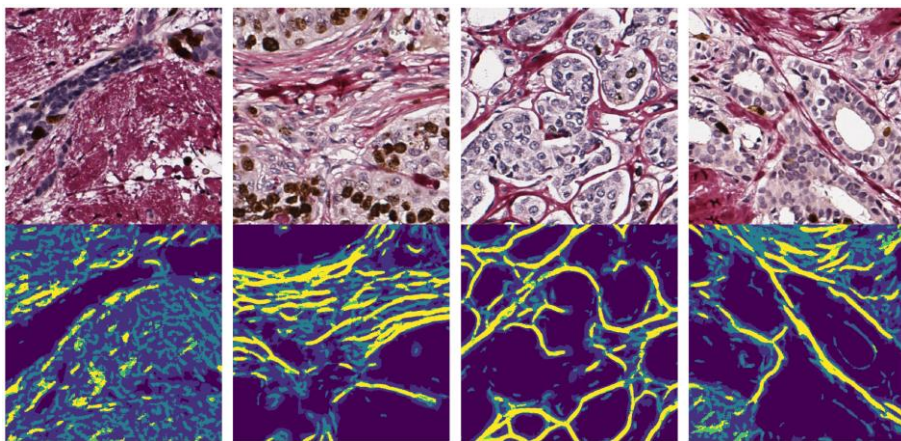

Figure 5.8 Examples of CSMs. Collagen segmentation masks (bottom row) extracted from TMA images (top row). In an overlay of CSMs from different ANN models, the bright yellow color indicates regions where all models agree, and darkest blue color indicates the background. Lighter shades of blue indicate M2 and M3. The yellow-colored area covers over 80% of M1.

Factor analysis of computed collagen framework features. To gain an understanding of the general properties of collagen framework architecture, three models trained with annotations by different experts and the least amount of processing applied (*nits* = 1 of morphological dilation) were evaluated. A set of textural, morphometric, orientation, and density descriptors of CSMs were selected. The factor analysis was performed to uncover latent relationships governing collagen arrangement in breast cancer. Eight independent factors (with eigenvalues ≥ 1) explain 86.2% of the variance in the data. Corresponding patterns are visualized in Figure 5.9.

With rare exceptions, similar features from all three different models form independent factors. Strong loadings of density (FD, nENDP) and texture (image entropy) from all three models combine in Factor 1. The variance of orientation magnitude (stdMag) from M1 and M2 and the mean and variance of the fiber length (mFL, stdFL) from M3 also contribute to Factor 1. Factor 2 is mainly composed of the morphology features of M1 (FS, FW, FL). Densities measured as the mean and variance of the distance between fiber endpoints (mD, stdD) from all models form Factor 3.
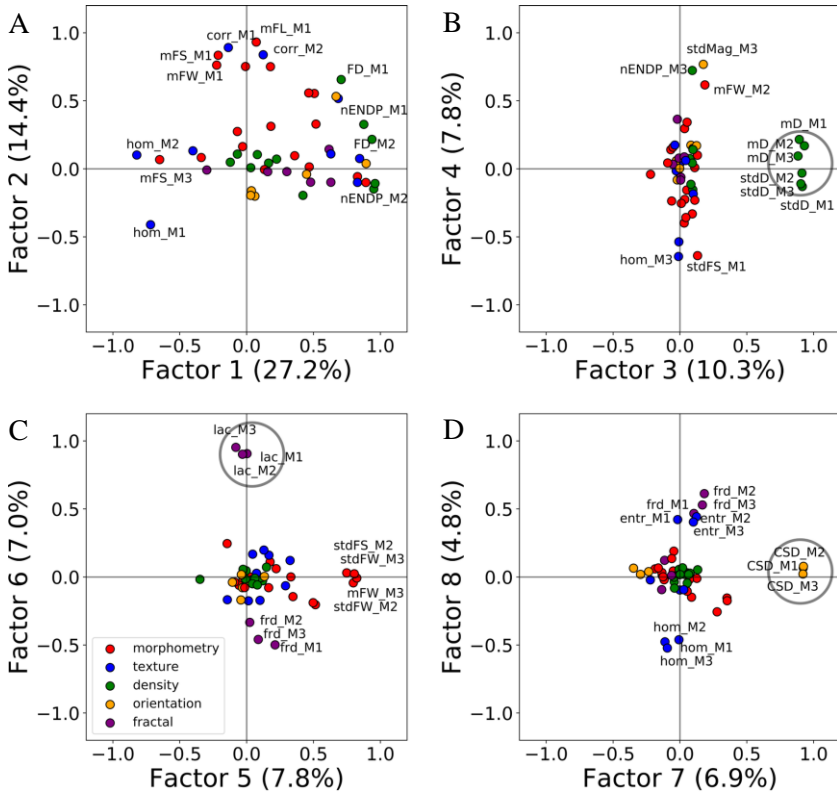
88

Figure 5.9 Rotated factor patterns. Factors 3, 6 & 7 - density (B), lacunarity (C), and orientation (D) features from all ANN models aggregate in orthogonally independent factors (circled). The proportion of variance explained by the factor is given on axes next to corresponding factor names. In total, 8 factors explain 86.2% of the variance in the data.

Density (nENDP) and the variance of orientation magnitude (stdMag) from M3 form Factor 4. The variance of the fiber width and straightness from M2 and M3 represent Factor 5. Factors 6, 7, and 8 are respectively composed of the lacunarity (lac), the variance of orientation angle (CSD), and fractal dimension (frd) from all three models.

Association of collagen features with tumor grade. The one-way ANOVA revealed statistically significant differences of means of collagen framework features between tumor grade groups (see Table 5.5). In M1 CSMs, lower packaging dimension (frd↓) distinguished high-grade (G3) from low-grade (G1, G2) tumors. More homogenous (homogeneity↑), less densely arranged (FD↓, nENDP↓, frd↓) collagen framework, and less

scattered fibers (stdMag↓) in M2 CSMs were more indicative of a high-grade tumor.

Table 5.5 Significant (*p*-value <0.05) feature differences (mean per patien/tumor image) between tumor grade groups.

		Low grade (G1, G2)	High grade (G3)
N		63	29
M1	***p*-value**	**difference (High - Low)**	
frd	0.027	-0.009	
M2	***p*-value**	**difference (High - Low)**	
mFS	0.025	-0.008	
mdFS	0.013	-0.009	
FD	0.011	178782.182	
nENDP	0.005	-3442.911	
Energy	0.016	0.039	
Contrast	0.012	-357.176	
Inertia	0.017	-1094.767	
Homogeneity	0.012	0.005	
Sum average	0.018	-10.439	
Sum variance	0.018	-4021.892	
Sum entropy	0.014	-0.095	
Entropy	0.014	-0.101	
Difference entropy	0.012	-0.030	
mMag	0.008	-33410.597	
stdMag	0.040	-15691.956	
frd	0.028	-0.009	
M3	***p*-value**	**difference (High - Low)**	
mFS	0.004	0.041	
mdFS	0.001	0.043	
FD	0.020	-386653.367	
Sum average	0.031	-22.110	
Informational measure of correlation 1	0.014	0.014	

Higher fiber straightness (mFS↑) and lower fiber density (FD↓) in M3 CSMs were characteristic of high-grade tumors.

Survival predictors. To predict patient survival, candidate features were selected in Kaplan-Meier univariate analysis.
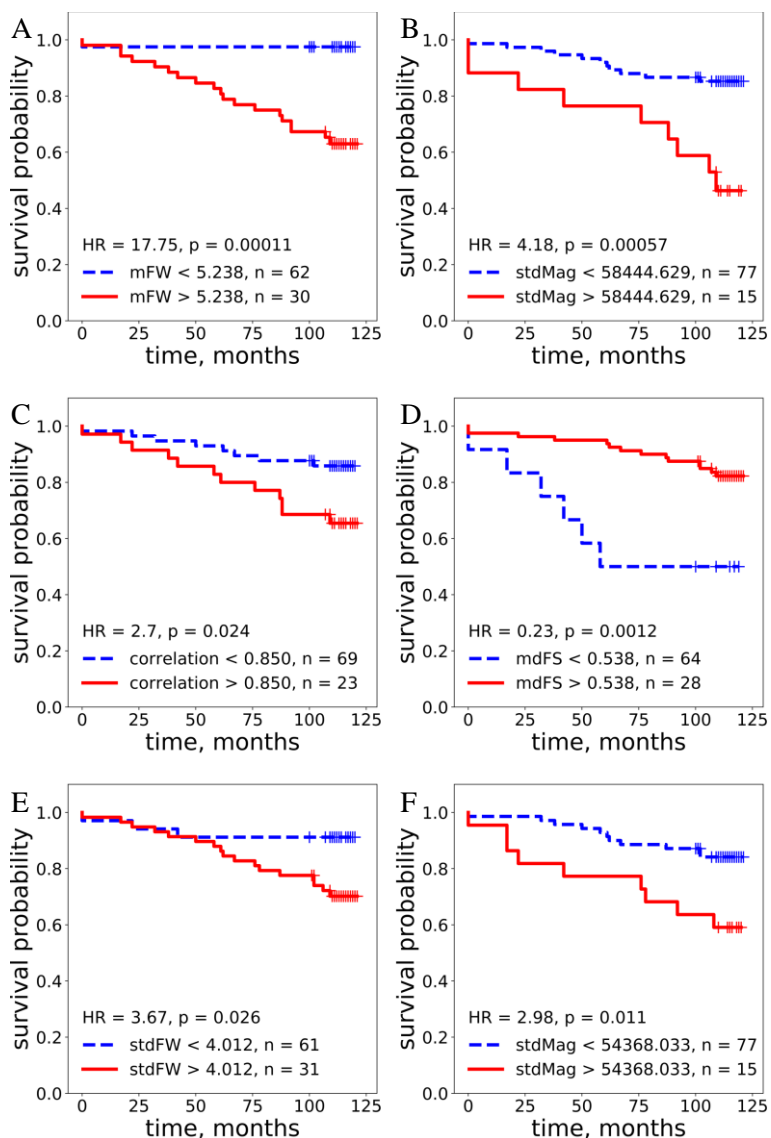
Figure 5.10 Kaplan-Meier survival plots with hazard ratio and log-rank test for correlation of collagen features with overall survival. Mean fiber width (A) and variance of orientation magnitude (B) from M1, median fiber straightness (C) and texture correlation (D) from M2, variance of fiber width (E) and variance of orientation magnitude (F) from M3.

Variables extracted from CSMs of all models (M1, M2, and M3) allowed prognostic dichotomization of the patients (see Table 5.6).

91

Table 5.6 Univariate analysis

Clinicopathological indicators	*p*-value	HR
T category (T1 vs. T2)	0.645	0.81
N category (N0 vs. N1-3)	0.200	1.79
Histological grade (G1 vs. G2-3)	1.000	1.00
Subtype (LumA vs. LumB-LumBHER2+)	0.630	1.24
Age (≤59 vs. >59)	0.062	2.62
M1	*p*-value	HR
mFW	<0.001	17.75
mdFW	<0.001	9.87
mFS	0.002	5.67
correlation	0.012	5.31
mdFP	<0.001	5.12
mdFS	0.001	4.66
mdFL	0.001	4.48
stdMag	0.001	4.18
mFP	0.022	3.79
mFL	0.031	3.14
FD	0.025	2.74
mMag	0.026	2.62
M2	*p*-value	HR
mFS	0.010	3.08
correlation	0.024	2.7
informational measure of correlation 1	0.015	0.35
mdFS	0.001	0.23
M3	*p*-value	HR
sdFW	0.026	3.67
mFW	0.007	3.14
mdFW	0.010	3.06
stdMag	0.011	2.98
sdD	0.019	2.86
mFP	0.031	2.74
mdD	0.025	2.64
mD	0.038	2.56
mdFS	0.031	0.35
CSD	0.004	0.27
CV	0.004	0.27

Subsequently, in a leave-one-out cross-validation procedure (see Table 5.7), sets of highest-ranking features were selected. They were used together with conventional pathological-clinical indicators (T and N categories, tumor grade, patient age - please reference Table 5.1) in the Cox proportional-hazards modeling.

Table 5.7 Feature selection

	N Obs	ChiSq	p >ChiSq
M1			
mFW, stdMag	85	4.749	0.030
M2			
mFS, correlation, mdFS	72	7.263	0.007
M3			
stdFW, stdMag	61	9.513	<0.001

Table 5.8 Multivariate Cox regression analysis. Each Cox regression model was obtained from the features of differently trained U-Net models and was named accordingly

Prognostic model 1 (likelihood ratios: 22.99, p-value = 1×10^{-5})			
	HR	**p-value**	**95% confidence**
stdMag	2.69	0.029	1.11 - 6.55
mFW	14.25	0.010	1.88 - 108.20
Prognostic model 2 (likelihood ratios: 16.21, p-value = 3×10^{-4})			
	HR	**p-value**	**95% confidence**
mdFS	0.12	<0.001	0.04 - 0.37
Correlation	4.54	0.003	1.65 - 12.49
Prognostic model 3 (likelihood ratios: 14.11, p-value = 9×10^{-4})			
	HR	**p-value**	**95% confidence**
stdMag	4.07	0.002	1.66 - 9.97
stdFW	5.01	0.011	1.44 - 17.43

Each resulting Cox regression model contained features of CSMs of different U-Net models. At least one fiber morphometry feature was present in all models - mFW in M1 (HR = 14.25), mdFS in M2 (HR = 0.12), and stdFW in M3 (HR = 5.01). The variance of orientation magnitude (stdMag) appeared in two models (M1, HR = 2.69 and M3, HR = 4.07) and texture correlation once (in M2, HR = 4.54). In any scenario, no clinicopathological

indicators entered the models (see Table 5.8 for prognostic model details and Figure 5.10 for Kaplan-Meier plots of prognostic features).

Discussion. In this chapter, the informative value of segmented collagen framework features was evaluated. It was found that independently trained U-Net models learned common aspects of tissue collagen architecture, although all models inherited expert comprehension of collagen representation via scarce, detailed, or semi-automated annotations. The trained models generated sets of collagen features that outperformed conventional clinical indicators in all prognostic models obtained. In general, it was demonstrated that FCNN-based models can extract essential information embedded in bright-field pathology images and provide prognostic value in BC patients.

For ANN to learn representations of collagen organization in a tissue image, the algorithm needs GT to compute the cross-entropy loss, and guide the training process. However, collagen, as an annotation object, is of a complex nature. Dekker et al. [161] assessed breast tumor stromal organization by manually drawing straight lines along stromal fibers. To segment collagen deposition in histology images, Jung et al. [162] generated annotations for ANN semi-automatically by image thresholding and subsequent manual refinement. To train the M3 ANN model, annotations similar to Jung et al. [162] were adopted. The approach by Dekker et al. [161] was expanded to train M1 and M2 ANNs and investigate the influence of cognitive bias on collagen perception by a human expert. It was experimentally demonstrated that human visual perception of tissue collagen framework is highly subjective, as experts' annotations did differ significantly by all aspects evaluated (see Table 5.4).

Interestingly, it was noted that ANNs inherited experts' level of detail. For example, the means of 10 of 13 Haralick texture features from M2 were significantly different between tumor grade groups, but only two from M3, and none from M1 differed significantly. M2, which trained on detailed, texture-rich annotations, produced collagen framework representations that reflect tumor growth patterns by the texture features. In contrast, in M1, which was trained on scarce annotations, the tumor grade is associated with fractal dimension – a less intuitive and more complex feature that describes pattern space-filling property. In M3, tumor cell clusters disrupt dense collagen landscapes and alter the basic geometry of bulk collagen mass; thus, collagen density and straightness features define tumor shape and are associated with histological grade.

94

Multiple studies based on second harmonic generation microscopy quantify local and global tumor collagen arrangement linking it with patient outcome. High orientation variance, local radial alignment of collagen fibers, and increased local collagen density were associated with invasion [228] and poor patient outcomes in breast carcinoma [161, 228-231]. Similarly, collagen alignment is suggestive of the worse prognosis in pancreatic ductal adenocarcinoma [232]. In gastric cancer, increased collagen fiber width was associated with reduced patient survival [233]. Experiments conducted in this research showed that similar features extracted from bright-field data allow significant patient stratification into prognostic groups in univariate analysis. The variance of orientation magnitude (M1: HR = 2.69, *p*-value = 0.029 & M3: HR = 4.07, *p*-value = 0.002), mean fiber width (M1: HR = 14.25, *p*-value = 0.010), the variance of fiber width (M3: HR = 5.01, *p*-value = 0.011), median fiber straightness (M2: HR = 0.12, *p*-value <0.001) and texture correlation (M2: HR = 4.54, *p*-value = 0.003), after cross-validation, serve as independent indicators in multivariate analysis. It is remarkable that the collagen framework data were extracted from a 1 mm diameter TMA spot per patient while no conventional clinicopathologic parameters were needed for the prognostic models (see Table 5.8).

TACS studies [157, 228] revealed exceptional prognostic information embedded in the collagen framework. The results presented here are in line with the concept of TACS. Latent correlations characterizing collagen arrangement in our CSMs were highly concordant between ANN models. Four factors were noted where the same features from all trained models combined (Factors 3, 6, 7, 8 see Figure 5.9). TACS-1 (increased collagen deposition) resembles Factor 3, where means and standard deviations of distances between collagen endpoints (a measure of density) accumulated. Similarly, TACS-2 (straightened fibers aligned to the tumor boundary) can be observed in Factor 6 (and less clearly in Factor 8), formed by lacunarity, a measure of gappiness. Finally, TACS-3 (radially aligned collagen fibers) can be assumed in Factor 7, represented by standard deviations of orientation angles.

5.3. Chapter Conclusions

A novel FCNN-based approach for TME collagen segmentation was developed. Differently trained models produced highly concordant collagen segmentation masks. *IoU* of collagen segmentations averaged over the whole dataset varied from 0.4 up to over 0.6. The averaged ratio of segmentation

areas by different models ranged from 0.5 up to 1.2, and the average common area covered by all segmentations ranged from 0.6 up to 1.0.

Principles governing collagen framework arrangement in tumorous tissue were assessed by factor analysis and confirmed to be in line with the established tumor-associated collagen signature paradigm. Eight independent factors (with eigenvalues ≥1) explain 86.2% of the variance in the data. Density, fractal, and orientation features from all assessed models aggregate in orthogonally independent factors (with correlation coefficients over 0.7).

Features extracted from the collagen architecture detected by all trained models differed significantly (p-value <0.05) between tumor grade groups. This fact suggests that all segmentation models independently capture aggressive tumor growth patterns by different features.

Given the ambiguity of collagen ground truth in bright-field microscopy images, the biological meaningfulness of collagen segmentations had to be proven by patient prognostication. Morphometric features extracted from collagen segmentations by all trained CNNs achieved reliable prognostic models (with likelihood ratios 14.11-22.99, p-value <0.05), and no established clinicopathological indicators were needed for breast cancer patients' prognostication.

6. MULTIPLE CLASS HISTOPATHOLOGY OBJECT SEGMENTATION FOR TUMOR CLASSIFICATION

Previous chapters touched upon different tumor histology object detection, segmentation, and classification. While Chapter 3 explored the classification of tumorous tissue regions into two major compartments - tumor epithelium and stroma, Chapter 4 introduced immune infiltrate (lymphocyte) detection and precise segmentation, and Chapter 5 added a method to segment and describe fibrous collagen in TME. This chapter is dedicated to exploring the segmentation of multiple histology objects from routine bright-field histology images of breast tumor tissue by an FCNN-based model. The motivation for detailed tumor deconstruction into histology primitives rises from the determination to formulate patient-level medical decision-making by objective, accurate, and standardized phenotyping of the disease's microscopic manifestations.

6.1. Experiment Design

This chapter presents a technique enabling simultaneous segmentation and identification of lymphocytes and dense immune infiltrates, tumor cell nuclei and tumorous tissue area, stromal cell nuclei and stromal tissue compartment, and TME collagen carcass from H&E-stained tumor tissue WSIs.

First, an image sampling strategy is proposed by introducing a tissue detector. A training dataset representing various tissue compartments is created by tissue zoning to train the segmentation model effectively. The training dataset of 256×256 pixel-sized image patches is thoroughly annotated by an expert highlighting four object classes - lymphocyte nuclei, tumor cell nuclei, stromal cell nuclei, and collagen fibers. Annotation masks are stacked to create multichannel ground truth masks. Additional four annotation channels are generated in an automated way - for nuclei of each type (and for all nuclei together), filling gaps between nuclei within the predetermined proximity to each other.

Then, an FCNN-based approach utilizing multichannel GT and multi-layer outputs is considered for the simultaneous segmentation of multiple histologic objects. The base model employed is a modified U-Net (described in detail in Chapter 5.1.3). An ensemble of weighted loss functions is explored to train the model.

Segmented histologic objects are subjected to morphometric analysis to build robust tissue-describing feature space. A set of 20 histology image features (nuclei densities, collagen fiber geometry, orientation, density, and texture) is extracted from segmentation masks.

To analyze the complete tumor tissue captured in a WSI tissue detector is applied, tissue containing region coordinates are acquired, and WSI is analyzed patch by patch. Segmented object morphometric features are aggregated into feature maps. To produce pathology endpoints, ML algorithms always require structured data. Although morphometric maps are very informative and can be appreciated visually, WSIs of different image plane sizes and varying tissue shapes and placement on a slide cannot be considered structured data. Morphometric map as a representation of WSI is not suitable for straightforward classification by ML models. A unified spatial relationship between tissue compartments preserving WSI representation is proposed to tackle the WSI classification problem.

The proposed method was tested in an international challenge. The challenge raised the task to predict specific breast tumor biomarker (HER2) status (pathology endpoint applicable to the whole tumor sample to select patients reliable for targeted therapy) for a set of routine H&E-stained breast tumor tissue WSIs. In a diagnostic pathology workup, this endpoint is only available by additional and special tissue processing, which means that human experts cannot reliably infer HER2 biomarker status from tissue morphology captured in routine H&E slides.

For each WSI in training and testing sets, WSI projections are generated. To predict the HER2 status deep neural network model (Xception [234] architecture) is trained, and WSIs in a testing set are classified as being HER2-positive or HER2-negative.

6.1.1. Dataset

Images. In this experiment, a set of 510 routine tissue slides (H&E-stained breast cancer tumor tissue WSIs) were used. Slides were obtained from the HEROHE Challenge [235]. Images of H&E-stained tissue slides were scanned at 20× optical magnification and saved in the MIRAX file format. The HEROHE Challenge was organized to promote computational techniques to assess biomarker status in tumor images acquired from routine tissue slides. Organizers provided two WSI datasets – a training set composed of 360 cases (144 biomarker-positive) and a test set composed of

150 cases. Experienced pathologists assessed biomarker status for each case according to the latest guidelines for breast cancer.

Image sampling. An overall scheme for data preparation is given in Figure 6.1. Firstly, a tissue segmentation map is created with three tissue zones: deep tumor, deep stroma, and an intermediate zone (roughly corresponding to IM). To achieve this tissue zoning an average pooling is applied to an original image (Figure 6.1, box 1) by sliding a 256×256 window. The resulting thumbnail image (Figure 6.1, box 2) is subjected to create a thumbnail representation in an artificial stain color space (Figure 6.1, box 3) by converting the color space from RGB to HED stain colors (Haematoxylin, Eosin, DAB) using the skimage library in Python [225]. Thumbnail HED representation is thresholded and normalized to the unit interval [0, 1], the DAB channel is discarded. Finally, tissue detection and zoning are achieved by k-means clustering (number of clusters = 4) on H and E channels of HED representation. Each pixel in a tissue segmentation map (Figure 6.1, box 4) corresponds to a 256×256 pixel-sized patch in an original WSI (Figure 6.1, box 5).
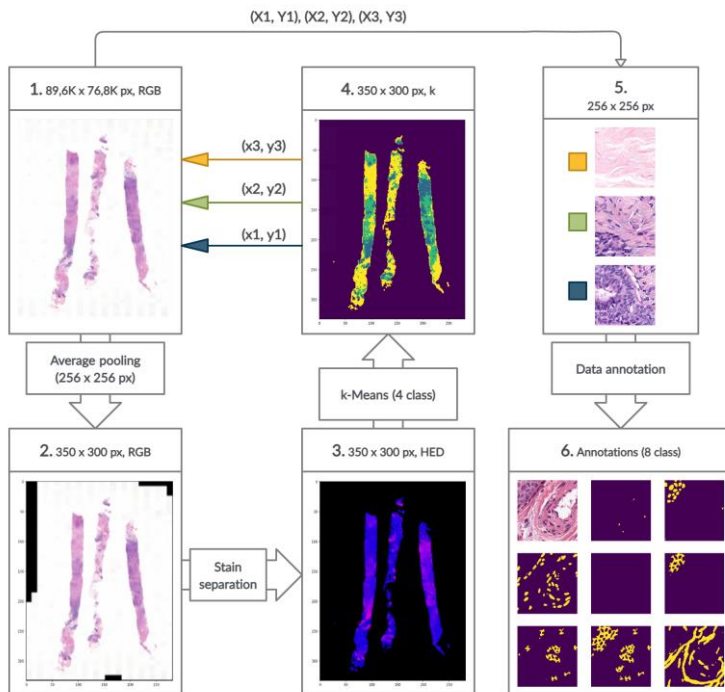

Figure 6.1 Data preparation scheme.

All nonzero pixels in the tissue segmentation map can be used to sample patches for WSI analysis. A set of 126 random 256×256 pixel-sized image patches is sampled from six WSIs to create a training dataset for the segmentation model (42 patches per tissue zone). All nonzero pixels in the tissue segmentation map are used to sample patches for WSI analysis. The training dataset of image patches is subjected to expert annotations (Figure 6.1, box 6).

Ground truth masks. The segmentation dataset was thoroughly annotated by an expert highlighting four object classes – lymphocyte nuclei, tumor cell nuclei, stromal cell nuclei, and collagen fibers. Additional four annotation layers were generated in an automated way – filling gaps for nuclei in close proximity to each other.
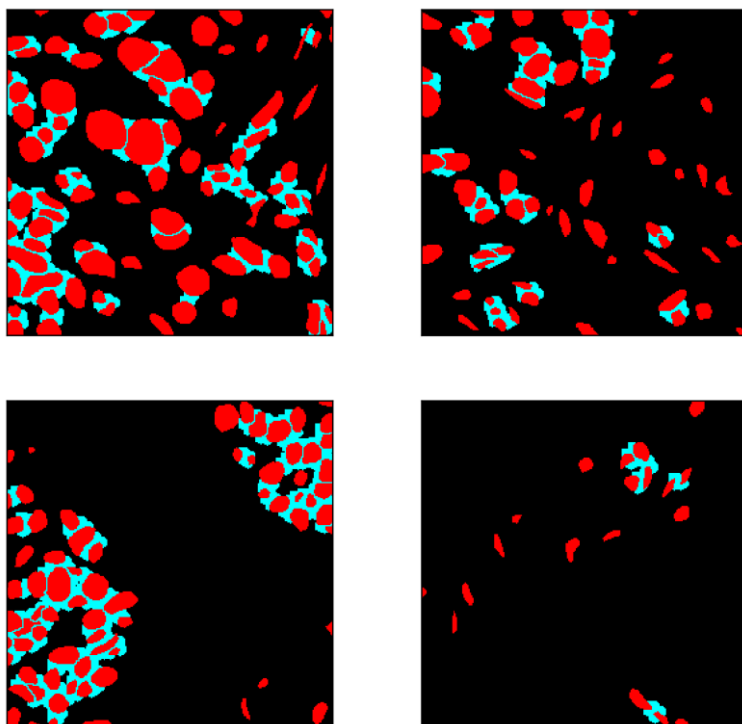

Figure 6.2 Nuclei in annotation masks in close proximity to each other were identified automatically and the inter-nuclear spaces were filled, creating a separate layer of annotations.

Nuclei are analyzed in pairs by comparing every nucleus against all others present in an annotation mask. Contours for both nuclei in a pair are detected by OpenCV module findContours in Python [236]. Points on the

contours of both nuclei within the predefined distance are saved to the proximity mask. Morphological dilation (with 8×8 pixel elliptical kernel) is applied to fill in the gap between saved contour points. Finally, the nuclei annotation mask is subtracted from the proximity mask to ensure that the nuclei mask does not overlap the proximity mask. Both nuclei and the resulting proximity masks are saved to the multi-channel annotation array as separate layers (see Figure 6.2). The proximity cutoff was set to 8 pixels (selected by a careful calibration). The gap-filling procedure is applied to masks of nuclei of each type (lymphocytes, tumor cells, stromal cells) separately, resulting in three additional layers of GT. One more layer of GT is produced by applying gap filling to the total nuclei mask.

6.1.2. U-Net Segmentation Model

A modified U-Net-based model (described in Chapter 5.1.3) was trained to segment targeted histologic objects. The network was modified to output an 8-layered segmentation map (one segmentation layer for each manual annotation class and one for each class generated by gap-filling). The model was set to minimize an ensemble loss function (see formula 6.2) – a combination of different weighted loss functions (intersection over union loss (see formula in 6.1), binary cross-entropy loss, mean square error loss, total variance loss [210, 237]) with adaptive moment estimation using default parameters provided in the original method [204].:

$$IoUL = 1 - \frac{TP}{FP+TP+FN} \qquad (6.1) \, ,$$

$$loss = w1 * BCL + w2 * MSE + w3 * TVL + w4 * IoUL \qquad (6.2)$$

where *BCL* is binary cross-entropy loss, *MSE* is mean square error, *TVL* is total variance loss, *IoUL* is intersection over union loss.

The model trained on single patch batches, and the dataset of annotated patches was split into training subset (50%) and validation subset (50%) to complicate the learning by moving the stress to the validation step. The algorithm was set to save model weights after each improvement in validation loss, and terminate the training phase after validation loss did not improve for 100 consecutive epochs or after 200 epochs passed.

The optimal combination of weights for an ensemble loss function was found by training the model within a predefined range of weights – $w1 \in$ [1...6, 1], $w2 \in$ [0...2, 1], $w3 \in$ [0...0.1, 0.1], $w4 \in$ [0...2, 1].

During training, the highest averaged multi-class segmentation accuracy 0.6415 by *IoU* was reached by a model with the following set of weights: $w1 = 2$, $w2 = 1$, $w3 = 0.1$, $w4 = 2$. This configuration was retrained for a longer period (set to terminate the training phase after validation loss did not improve for 100 consecutive epochs or after 600 epochs passed), and the model converged after 493 epochs reaching the averaged multi-class segmentation accuracy of 0.6849 by *IoU*.

The trained segmentation U-Net model generates 256×256×8 output for each 256×256×3 input. For further analysis, WSIs are segmented patch-by-patch following an image sampling map (Figure 6.1 box 4) covering the whole tissue area captured in WSI.

6.1.3. Tissue Morphometry

Morphometry was applied directly to the U-Net output (see Figure 6.3), yielding a set of 20 histology image features such as nuclei densities, collagen fiber density, collagen fiber straightness, and others (see Table 6.1).
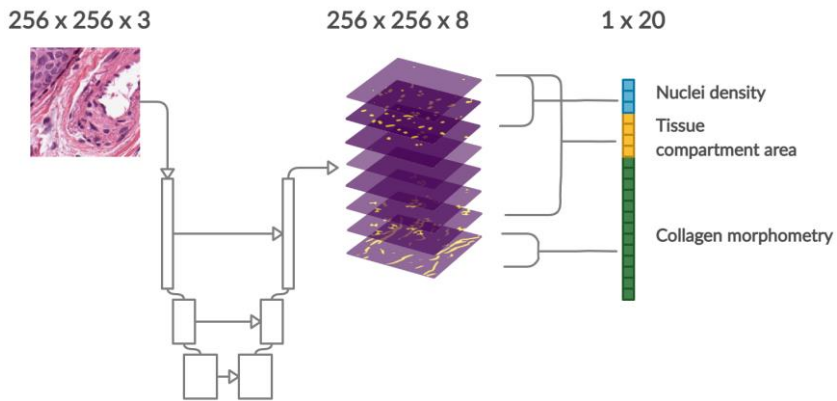

Figure 6.3 Morphometry of segmented histologic objects.

This feature space greatly overlaps with the one proposed in Chapter 5.1.4 (for collagen-related features please refer to Table 5.3). To extract collagen texture correlation and entropy Python computer vision and image processing library Mahotas [195] was used.

Table 6.2 The list of morphometric features used to describe U-Net segmentation outputs.

Cell nuclei density	Source (U-Net output layer)
Lymphocyte nuclei density	Lymphocyte mask
Tumor cell nuclei density	Tumor cell nuclei mask
Stromal cell nuclei density	Stromal cell nuclei mask
Tissue area	
Immune infiltrate area	Lymphocyte mask, inter-nuclear space mask for lymphocytes
Tumorous tissue area	Tumor cell nuclei mask, inter-nuclear space mask for tumor cell nuclei
Stromal tissue area	Stromal cell nuclei mask, inter-nuclear space mask for stromal cell nuclei
Tissue area	Combined mask of all types of nuclei and inter-nuclear space
Collagen fiber orientation	
Circular variance	Collagen carcass mask
Circular standard deviation	
Mean magnitude	
Standard deviation of the magnitude	
Collagen fiber morphometry	
Mean fiber length	Collagen carcass mask
Mean fiber path	
Mean fiber straightness	
Mean fiber width	
Collagen fiber density	
Number of non-zero pixels	Collagen carcass mask
Number of endpoints	
Mean distance between fiber endpoints	
Collagen fiber texture	
Correlation	Collagen carcass mask
Entropy	

Morphometry features from WSI are aggregated into morphometric maps whose 1 pixel corresponds to a 256×256 pixel-sized patch in an original WSI (see Figure 6.4). Morphometric maps can be assembled into RGB images purely for visualization purposes. Different combinations of up to three maps combined into an RGB image can reveal distinctive tissue section properties. Figure 6.4 shows morphometric maps of TME-related components.
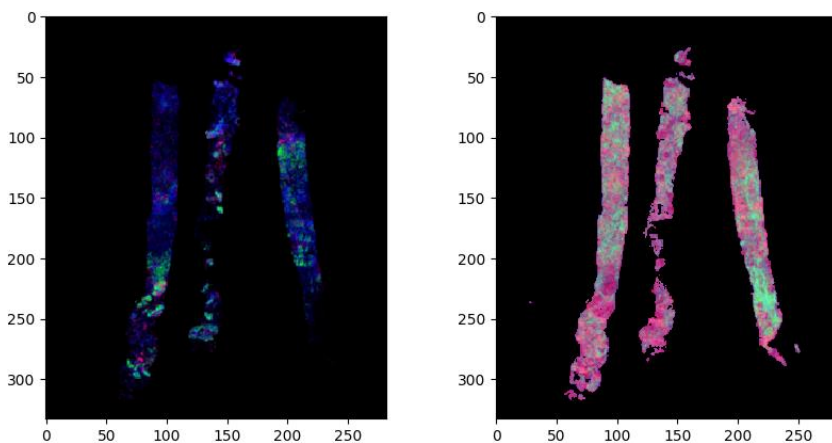
Figure 6.4 Morphometric maps. In the left panel of the figure, the green color highlights tumor cell nuclei abundant areas, the blue color highlights tissue areas with high fibroblast densities, and the red corresponds to immune infiltrate rich areas. In the right panel of the figure, the red color indicates areas with higher collagen fiber orientation variance, the green indicates higher fiber orientation magnitude, and the blue indicates higher fiber straightness.

Both stromal cells and lymphocytes are components of TME and can be regarded with respect to tumor cells in the left panel of Figure 6.4. The proximity of red and green can be noted, indicating inflammation around the tumor cell islands. TME-collagen fiber morphometry is visualized in the left panel of Figure 6.4. It can be noted that the light green color depicts areas outside tumor cell islands, indicating straightened and uniform distribution of collagen fibers.

6.1.4. WSI Classification

To be able to produce pathology insights from complete WSIs, straightforward WSI classification is considered. A projection into a fixed size (also reasonably low-sized) representation is considered for a tumor tissue sample captured in WSI. The proposed WSI projection is based on a co-occurrence matrix principle. Each point in a morphometric map corresponds to a particular area in the tissue that can be defined by a proportion of the tumorous tissue (t%) it contains and an average proportion of stromal tissue (s%) surrounding it. Since t% and s% are a percentage, a projection will always be a 100×100 array, and t% and s% define a position of a point in a projection. Embedding a large-sized WSI in a low-sized

representation comes at the cost of dimensionality increase. A projection is populated layer-by-layer with values from each feature layer of a morphometric map. Points with identical (t%, s%) combinations are aggregated into WSI projection by the mean, median, and standard deviation. This way, WSI is represented by a 100×100×60-dimension projection. The scheme of projection generation is given in Figure 6.5.
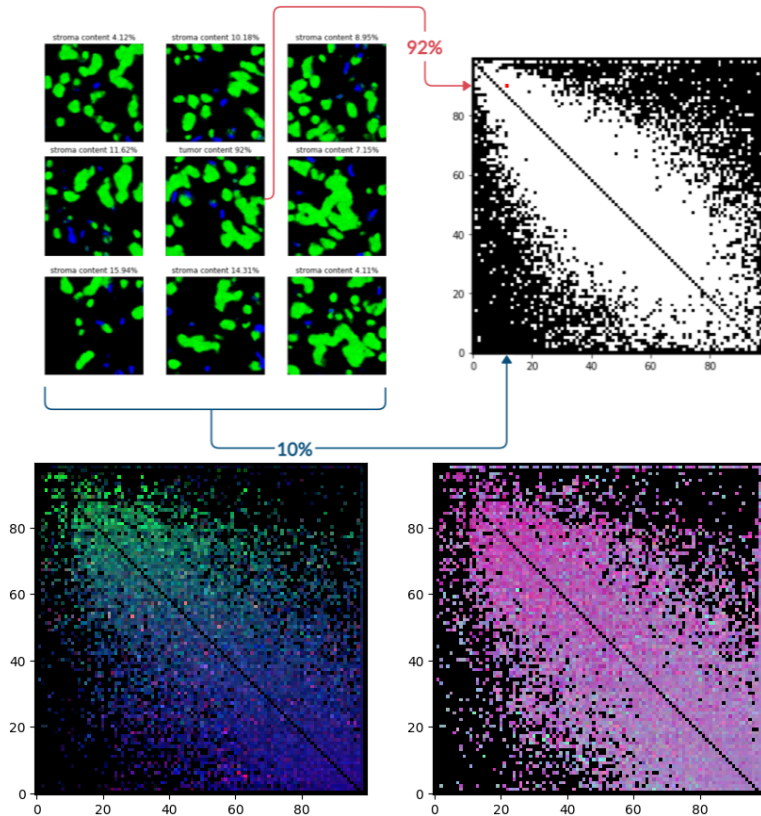

Figure 6.5 The WSI projection. The scheme of projection generation is given on top. The green color corresponds to the tumor area (tumor nuclei merged with inter-tumoral nuclear space), blue corresponds to the stromal area (fibroblasts merged with corresponding inter-nuclear space). The proportion of these tissue compartments in the target image and its surroundings defines its coordinates in the projection space. Bottom: examples of projections generated from the morphometric maps of Figure 6.4.

WSI projections are still directly interpretable and essentially retain the visual appreciation of morphometric maps. In the projection given on the left

panel of Figure 6.5, red dots corresponding to lymphocyte density stay close to the green cluster of dense tumor cells (↑t%, ↓s%) but do not penetrate deep inside it and are mainly dispersed among blue dots corresponding to stromal cells (↓t%, ↑s%). Notably, this representation forces differently sized WSIs to be structured identically with fixed dimensions. Therefore, WSI projections enable straightforward WSI classification by virtually any ML classifier model.

The Xception [234] model was trained to predict tumor HER2 biomarker status. The training dataset was randomly split into training subset (80%) and validation subset (20%) and the model was trained on single sample batches. The objective of the challenge was to produce both soft and hard predictions about the biomarker status of a specimen. Therefore binary cross-entropy loss was used to guide the training. The algorithm was set to save model weights after each improvement in validation loss and terminate the training phase after validation loss did not improve for 20 consecutive epochs.

For DL TensorFlow framework in Python was used [198]. Full training of the model was performed on a high-performance graphical processing unit (Nvidia GeForce GTX1080).

Feature extraction and quantification were implemented using the computer vision and image processing libraries scikit-image [225], Mahotas [195] and OpenCV [236] in Python.

6.2. Results

To predict the HER2 status of the tumor at the WSI level, WSIs were processed by the method presented in this chapter. For each WSI in training and testing sets, morphometric feature maps were generated as described in Chapter 6.1.3. To predict the HER2 status WSI projections were generated as described in Chapter 6.1.4. The deep neural network model (Xception [234] architecture) was trained, and WSIs in a testing set were classified as being HER2-positive or HER2-negative.

6.2.1. WSI Segmentation

The image sampling strategy presented in Chapter 6.1.1 (Fig. 6.1) was applied to select a set of 126 random 256×256 pixel-sized image patches from 6 WSIs from the testing set to create a training dataset for the

segmentation model. Image patches were annotated to obtain the ground truth as described in Chapter 6.1.1, and the model was trained as described in Chapter 6.1.2. The trained segmentation model learned to output segmentation masks for eight object classes.

Table 6.3 Segmentation network performance metrics.

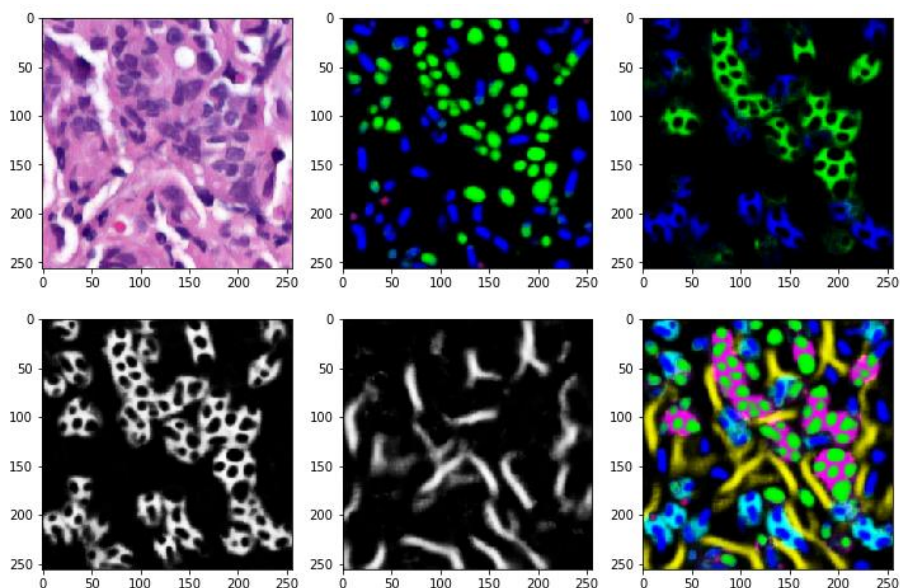|	Accuracy	Precision	Recall	F1-score	*IoU*
lymphocytes	0.9970	0.8770	0.7251	0.7827	0.6642
tumor cells	0.9942	0.8652	0.9357	0.8743	0.8264
stromal cells	0.9807	0.8322	0.8177	0.8182	0.7029
collagen fibers	0.9309	0.5060	0.8891	0.6127	0.4715

Figure 6.6 WSI segmentation. For every patch sampled from WSI, the U-Net model outputs 8-class segmentation masks. H&E image is decomposed (lower right corner panel) into a tumor (green) and stromal (blue) cell nuclei, lymphocytes (red), tumor area (magenta), stroma area (light blue), and collagen fibers (yellow) (dense immune infiltrate is not present in this image, hence not shown).

Additional 20 patches were sampled and annotated to test the segmentation performance. A visual example of segmentation masks can be appreciated in Figure 6.6, and the segmentation performance metrics for the four manually annotated object classes is given in Table 6.3.

6.2.2. WSI Classification

For each WSI in training and testing sets, morphometric feature maps were generated and used to transform WSIs into WSI projections. The Xception model was trained to predict tumor HER2 biomarker status using a training set composed of 360 cases (144 HER2-positive). The training dataset was randomly split into training subset (280 WSIs, 80%) and validation subset (80 WSIs, 20%), and the model was tested by training with three optimizers (see Figure 6.7) - stochastic gradient descent (SGD [238]), Adam [204], and Adadelta [239] with default parameter values provided in the original method (available in Keras API [199]).
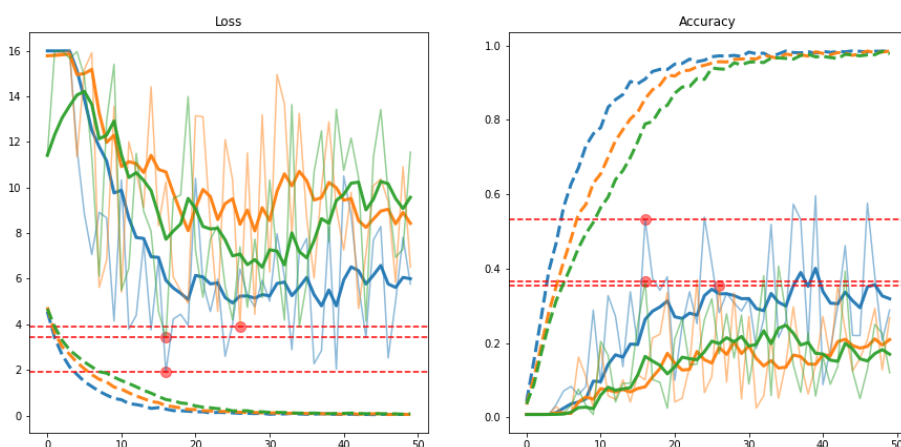
Figure 6.7 Classifier training metrics. Dashed line depicts training phase, continuous line depicts validation phase (bold lines for validation data are shown as exponentially smoothed moving average to highlight the trend). Red dots indicate the point of convergence (last improvement of validation loss). Blue lines - SGD, green lines - Adam, orange - Adadelta.

The Xception model trained with SGD optimizer achieved higher validation accuracy (0.5327, after 16 epochs) than with Adam (0.3645, after 16 epochs) or Adadelta (0.3556, after 26 epochs) optimizers (see Figure 6.7).

6.2.3. Evaluation

A test set composed of 150 unknown HER2 status cases was analyzed as presented in this chapter and the results were submitted for evaluation.

Out of 863 participants, only 21 were able to return the results indicating that the problem of patient-level biomarker status prediction directly from images is not trivial. The proposed algorithm was ranked 6th by precision (0.5349), 10th by AUC (0.6276), and only 17th by recall (0.3833), and 16th by F1-score (0.4466).

Table 6.4 Challenge results*. The number of teams registered for the challenge – 863; results were submitted by 21 teams.

Rank	Team	AUC	Precision	Recall	F1-score
1	Macaroon	0.7056	0.5682	0.8333	0.6757
2	MITEL	0.7443	0.5803	0.7833	0.6667
3	Piaz	0.8439	0.7674	0.5500	0.6408
4	Dratur	0.7478	0.5676	0.7000	0.6269
5	irisai	0.6668	0.5797	0.6667	0.6202
6	Arontier_HYY	0.7217	0.5238	0.7333	0.6111
7	KDE	0.6209	0.5114	0.7500	0.6081
8	joangibert14	0.6606	0.4845	0.7833	0.5987
9	visilab	0.6268	0.5058	0.7333	0.5986
10	MIRL	0.5000	0.4000	1.0000	0.5714
11	aetherAI	0.6604	0.4938	0.6667	0.5674
12	NCIC	0.6267	0.5211	0.6167	0.5649
13	biocenas	0.5741	0.4638	0.5333	0.4961
14	HEROH	0.5926	0.4571	0.5333	0.4923
15	Reza_Mohebbian	0.6058	0.5098	0.4333	0.4685
16	**mindmork**	**0.6276**	**0.5349**	**0.3833**	**0.4466**
17	Institute_of_Pathology_Graz	0.6257	0.5000	0.3833	0.4340
18	katherandco	0.4415	0.4423	0.4035	0.4220
19	QUILL	0.6315	0.5000	0.3333	0.4000
20	HEROHE_Challenge	0.4833	0.3721	0.2667	0.3107
21	uc_csse	0.4732	0.3137	0.2667	0.2883

* - https://ecdp2020.grand-challenge.org/RESULTS/

6.3. Chapter Conclusions

This chapter described the integration of tumor-centric and TME-centric segmentation algorithms utilizing experience and knowledge gained in previous experiments.

An aggregated segmentation method was presented. Segmentation of multiple histologic objects in a single FCNN-based model was achieved by leveraging multichannel ground truth and multilayer outputs of the model. During training, the model reached an averaged multi-class segmentation accuracy of 0.6849 as assessed by *IoU*.

The transformation of a WSI was proposed to enable deep neural network training regardless of WSI size while keeping spatial relationships between tissue compartments. The proposed transformation allows achieving competitive biomarker status prediction results of AUC score 0.6276 and F1-score 0.4466.

GENERAL CONCLUSIONS

Literature analysis revealed that tumor microenvironment related object segmentation and classification is somewhat neglected in digital pathology, especially when analysing commonly in routine pathology diagnostics H&E-stained tissue WSI scans.

A superpixel-based annotation approach of H&E-stained tissue WSI data for tumor epithelium-stroma classification was introduced. Conventional classifiers such as support vector machine, random decision forest, and multilayer perceptron showed quite similar performance ranging from AUC 0.9533 to 0.9666. The best result was obtained by a multilayer perceptron. Color space has an impact on superpixel classification accuracy. Adding superpixel color features allows an increase of classification accuracy in terms of AUC from 0.9542 up to 0.9666 when compared to texture features only. However, the best AUC of 0.9895 was obtained by the CNN classifier trained on patched image data and showed the best generalization properties among investigated classifiers.

A lightweight method having good generalization properties for cell nuclei segmentation and consecutive lymphocyte classification in H&E-stained breast and colorectal cancer WSIs was proposed.
- The modified shallow U-Net architecture supplemented with multiple-input layers and the introduced convolutional texture blocks allowed to obtain a lower model complexity than original U-Net and Micro-Net models and achieved higher nuclei segmentation Dice accuracy reaching 0.80 compared to those 0.78 and 0.79 obtained by the U-Net and Micro-Net models respectively while training on nuclei masks only. Further the architecture performance was increased to 0.81 when trained on nuclei masks supplemented with an active contour layer.
- Multilayer perceptron produced the best results among the tested lymphocytes classifiers with a classification accuracy of 0.78 – higher than those obtained by the random forest classifier and CNN producing accuracy of 0.77 and 0.76 respectively.
- The proposed method for nuclei segmentation and classification by modified U-Net architecture was tested on a public dataset and showed good generalization properties. The obtained 0.71 lymphocyte classification accuracy was even more increased up to

0.81 by introducing stain normalization procedure. The obtained results are comparable to the state-of-the-art lymphocyte detection methods but provide an additional lymphocyte segmentation capability.

A deep neural network architecture was introduced for tumor microenvironment collagen segmentation.
- Independent instances of models were trained on highly differing annotations and reached consensus by producing highly concordant collagen segmentation masks as assessed by *IoU* (0.4 – 0.6), the ratio of segmentation areas (0.5 – 1.2), and the common area covered by all segmentations (0.6 – 1.0). The analysis revealed that tumor grade, a feature of a tumor that in routine practice is only inferred visually by a human expert, can be determined by collagen features. Trained models independently captured aggressive tumor growth patterns by significantly emphasizing different collagen features as determined by the analysis of collagen feature variance between tumor grade groups with ANOVA test having *p*-value <0.05. Accomplished factor analysis confirmed collagen arrangement governing principles after the segmentation step.
- Collagen features such as fiber orientation and morphometry currently available only by specialized tissue imaging techniques were extracted from collagen segmentation maps produced by the proposed method and were confirmed to be reliable by prognostic modeling with obtained likelihood ratio interval 14.11-22.99, at *p*-value <0.05. The results suggest that the above-mentioned features after careful analysis have the potential to be implemented in routine pathology diagnostics.

A modified U-Net architecture proposed for collagen segmentation was further generalized to segment eight tumorous tissue components from routine H&E-stained breast tissue WSIs at the same step by utilizing multi-channel ground truth masks. The trained model achieved a reasonably accurate multi-class segmentation *IoU* of 0.6849. A whole-slide image transformation that retains spatial relationships between the segmented tumor tissue components was introduced by constructing an image feature space based on explicit morphometry rules applied to the eight segmented object classes of the tumorous tissue. The introduced transformation embeds a whole-slide image into a projection of fixed dimensions that allows any

machine learning classifier that works on predefined input data sizes to be trained on complete whole-slide images of arbitrary sizes. The complete workflow consisting of a generalized multi-class segmentation model, proposed WSI transformation, and a trained WSI projection classifier achieved competitive tumor biomarker prediction results having AUC and F1 scores 0.6276 and 0.4466 respectively.

REFERENCES

[1]   A. T. Feldman and D. Wolfe, "Tissue Processing and Hematoxylin and Eosin Staining," in *Histopathology: Methods and Protocols*, C. E. Day Ed. New York, NY: Springer New York, pp. 31-43, 2014.

[2]   E. R. Malone, M. Oliva, P. J. B. Sabatini, T. L. Stockley, and L. L. Siu, "Molecular profiling for precision cancer therapies," *Genome Medicine,* vol. 12, no. 1, p. 8, 2020, doi: 10.1186/s13073-019-0703-1.

[3]   S. Brassart-Pasco, S. Brezillon, B. Brassart, L. Ramont, J. B. Oudart, and J. C. Monboisse, "Tumor Microenvironment: Extracellular Matrix Alterations Influence Tumor Progression," *Frontiers in Oncology,* Mini Review vol. 10, no. 397, p. 397, 2020, doi: 10.3389/fonc.2020.00397.

[4]   R. Baghban *et al.*, "Tumor microenvironment complexity and therapeutic implications at a glance," *Cell Communication and Signaling,* vol. 18, no. 1, p. 59, 2020, doi: 10.1186/s12964-020-0530-4.

[5]   A. Labani-Motlagh, M. Ashja-Mahdavi, and A. Loskog, "The Tumor Microenvironment: A Milieu Hindering and Obstructing Antitumor Immune Responses," *Frontiers in Immunology,* Review vol. 11, no. 940, p. 940, 2020, doi: 10.3389/fimmu.2020.00940.

[6]   B. Allard *et al.*, "Immuno-oncology-101: overview of major concepts and translational perspectives," *Seminars in Cancer Biology,* vol. 52, no. Pt 2, pp. 1-11, 2018, doi: 10.1016/j.semcancer.2018.02.005.

[7]   K. C. Valkenburg, A. E. de Groot, and K. J. Pienta, "Targeting the tumour stroma to improve cancer therapy," *Nature Reviews: Clinical Oncology,* vol. 15, no. 6, pp. 366-381, 2018, doi: 10.1038/s41571-018-0007-1.

[8]   R. R. Somani and U. V. Bhanushali, "Targeting angiogenesis for treatment of human cancer," *Indian Journal of Pharmaceutical Sciences,* vol. 75, no. 1, pp. 3-10, 2013, doi: 10.4103/0250-474X.113529.

[9]   S. Y. Gun, S. W. L. Lee, J. L. Sieow, and S. C. Wong, "Targeting immune cells for cancer therapy," *Redox Biology,* vol. 25, p. 101174, 2019, doi: 10.1016/j.redox.2019.101174.

[10]   J. Galon *et al.*, "Cancer classification using the Immunoscore: a worldwide task force," *Journal of Translational Medicine,* vol. 10, no. 1, p. 205, 2012, doi: 10.1186/1479-5876-10-205.

[11]   J. Saltz *et al.*, "Spatial Organization and Molecular Correlation of Tumor-Infiltrating Lymphocytes Using Deep Learning on Pathology Images," *Cell Reports,* vol. 23, no. 1, pp. 181-193 e187, 2018, doi: 10.1016/j.celrep.2018.03.086.

[12]   A. N. Basavanhally *et al.*, "Computerized image-based detection and grading of lymphocytic infiltration in HER2+ breast cancer histopathology," *IEEE Transactions on Biomedical Engineering,* vol. 57, no. 3, pp. 642-653, 2010, doi: 10.1109/TBME.2009.2035305.

[13]   J. Chen and C. Srinivas, "Automatic Lymphocyte Detection in H&E Images with Deep Neural Networks," *ArXiv,* vol. abs/1612.03217, 2016.

[14]   A. Mouelhi, H. Rmili, J. B. Ali, M. Sayadi, R. Doghri, and K. Mrad, "Fast unsupervised nuclear segmentation and classification scheme for automatic allred cancer scoring in immunohistochemical breast tissue images," *Computer Methods and Programs in Biomedicine,* vol. 165, pp. 37-51, 2018, doi: 10.1016/j.cmpb.2018.08.005.

[15]   M. Veta, P. J. van Diest, R. Kornegoor, A. Huisman, M. A. Viergever, and J. P. Pluim, "Automatic nuclei segmentation in H&E stained breast cancer histopathology images," *PloS One,* vol. 8, no. 7, p. e70221, 2013, doi: 10.1371/journal.pone.0070221.

[16]   T. M. Bauman *et al.*, "Characterization of fibrillar collagens and extracellular matrix of glandular benign prostatic hyperplasia nodules," *PloS One,* vol. 9, no. 10, p. e109102, 2014, doi: 10.1371/journal.pone.0109102.

[17]   M. Wolman and F. H. Kasten, "Polarized light microscopy in the study of the molecular structure of collagen and reticulin," *Histochemistry,* vol. 85, no. 1, pp. 41-49, 1986, doi: 10.1007/BF00508652.

[18]   K. A. Wegner, A. Keikhosravi, K. W. Eliceiri, and C. M. Vezina, "Fluorescence of Picrosirius Red Multiplexed With Immunohistochemistry for the Quantitative Assessment of Collagen in Tissue Sections," *Journal of Histochemistry and Cytochemistry,* vol. 65, no. 8, pp. 479-490, 2017, doi: 10.1369/0022155417718541.

[19]   C. Saillard *et al.*, "Predicting Survival After Hepatocellular Carcinoma Resection Using Deep Learning on Histological Slides," *Hepatology,* vol. 72, no. 6, pp. 2000-2013, 2020, doi: 10.1002/hep.31207.

[20]   R. Yamashita, J. Long, A. Saleem, D. L. Rubin, and J. Shen, "Deep learning predicts postsurgical recurrence of hepatocellular carcinoma from digital histopathologic images," *Scientific Reports,* vol. 11, no. 1, p. 2047, 2021, doi: 10.1038/s41598-021-81506-y.

[21]   R. R. Rawat *et al.*, "Deep learned tissue "fingerprints" classify breast cancers by ER/PR/Her2 status from H&E images," *Scientific Reports,* vol. 10, no. 1, p. 7275, 2020, doi: 10.1038/s41598-020-64156-4.

[22]   P. C. Nowell, "The clonal evolution of tumor cell populations," *Science,* vol. 194, no. 4260, pp. 23-28, 1976, doi: 10.1126/science.959840.

[23]   A. Fortunato, A. Boddy, D. Mallo, A. Aktipis, C. C. Maley, and J. W. Pepper, "Natural Selection in Cancer Biology: From Molecular Snowflakes to Trait Hallmarks," *Cold Spring Harbor Perspectives in Medicine,* vol. 7, no. 2, p. a029652, 2017, doi: 10.1101/cshperspect.a029652.

[24]   L. Koch, "Cancer genomics: The driving force of cancer evolution," *Nat Rev Genet,* vol. 18, no. 12, p. 703, 2017, doi: 10.1038/nrg.2017.95.

[25]   T. Goto, Y. Hirotsu, K. Amemiya, H. Mochizuki, and M. Omata, "Understanding Intratumor Heterogeneity and Evolution in NSCLC and Potential New Therapeutic Approach," *Cancers,* vol. 10, no. 7, p. 212, 2018, doi: 10.3390/cancers10070212.

[26]   M. Greaves and C. C. Maley, "Clonal evolution in cancer," *Nature,* vol. 481, no. 7381, pp. 306-313, 2012, doi: 10.1038/nature10762.

[27]   M. Casas-Selves and J. Degregori, "How cancer shapes evolution, and how evolution shapes cancer," *Evolution (N Y),* vol. 4, no. 4, pp. 624-634, 2011, doi: 10.1007/s12052-011-0373-y.

[28]   D. Hanahan and R. A. Weinberg, "The hallmarks of cancer," *Cell,* vol. 100, no. 1, pp. 57-70, 2000, doi: 10.1016/s0092-8674(00)81683-9.

[29]   E. Solary and L. Laplane, "The role of host environment in cancer evolution," *Evolutionary Applications,* vol. 13, no. 7, pp. 1756-1770, 2020, doi: 10.1111/eva.13039.

[30]   D. Hanahan and R. A. Weinberg, "Hallmarks of cancer: the next generation," *Cell,* vol. 144, no. 5, pp. 646-674, 2011, doi: 10.1016/j.cell.2011.02.013.

[31]   H. Peinado *et al.*, "Pre-metastatic niches: organ-specific homes for metastases," *Nature Reviews: Cancer,* vol. 17, no. 5, pp. 302-317, 2017, doi: 10.1038/nrc.2017.6.

[32]   S. Paget, "The Distribution of Secondary Growths in Cancer of the Breast," *The Lancet,* vol. 133, no. 3421, pp. 571-573, 1889, doi: 10.1016/s0140-6736(00)49915-0.

[33]   R. Virchow, "Cellular pathology. As based upon physiological and pathological histology. Lecture XVI--Atheromatous affection of arteries. 1858," *Nutrition Reviews,* vol. 47, no. 1, pp. 23-25, 1989, doi: 10.1111/j.1753-4887.1989.tb02747.x.

[34]   M. A. Morse, S. Chui, A. Hobeika, H. K. Lyerly, and T. Clay, "Recent developments in therapeutic cancer vaccines," *Nature Clinical Practice: Oncology,* vol. 2, no. 2, pp. 108-113, 2005, doi: 10.1038/ncponc0098.

[35]   K. M. Hargadon, C. E. Johnson, and C. J. Williams, "Immune checkpoint blockade therapy for cancer: An overview of FDA-approved immune checkpoint inhibitors," *International Immunopharmacology,* vol. 62, pp. 29-39, 2018, doi: 10.1016/j.intimp.2018.06.001.

[36]   B. L. Brucher and I. S. Jamall, "Cell-cell communication in the tumor microenvironment, carcinogenesis, and anticancer treatment," *Cellular Physiology and Biochemistry,* vol. 34, no. 2, pp. 213-243, 2014, doi: 10.1159/000362978.

[37]   T. Liu *et al.*, "Cancer-associated fibroblasts: an emerging target of anti-cancer immunotherapy," *Journal of Hematology & Oncology,* vol. 12, no. 1, p. 86, 2019, doi: 10.1186/s13045-019-0770-1.

[38]   P. Dobosz and T. Dzieciatkowski, "The Intriguing History of Cancer Immunotherapy," *Frontiers in Immunology,* vol. 10, p. 2965, 2019, doi: 10.3389/fimmu.2019.02965.

[39]   M. M. Bui *et al.*, "Digital and Computational Pathology: Bring the Future into Focus," *Journal of Pathology Informatics,* vol. 10, p. 10, 2019, doi: 10.4103/2153-3539.255259.

[40]   E. Abels *et al.*, "Computational pathology definitions, best practices, and recommendations for regulatory guidance: a white paper from the Digital Pathology Association," *Journal of Pathology,* vol. 249, no. 3, pp. 286-294, 2019, doi: 10.1002/path.5331.

[41]   L. Barisoni, K. J. Lafata, S. M. Hewitt, A. Madabhushi, and U. G. J. Balis, "Digital pathology and computational image analysis in nephropathology," *Nat Rev Nephrol,* vol. 16, no. 11, pp. 669-685, 2020, doi: 10.1038/s41581-020-0321-6.

[42]   M. Cui and D. Y. Zhang, "Artificial intelligence and computational pathology," *Laboratory Investigation,* vol. 101, no. 4, pp. 412-422, 2021, doi: 10.1038/s41374-020-00514-0.

[43]   L. Breiman, J. Friedman, C. J. Stone, and R. A. Olshen, *Classification and regression trees*. CRC press, 1984.

[44]   D. E. Rumelhart, G. E. Hinton, and J. L. McClelland, "A general framework for parallel distributed processing," *Parallel distributed processing: Explorations in the microstructure of cognition,* vol. 1, no. 45-76, p. 26, 1986.

[45]   D. E. Rumelhart, G. E. Hinton, and R. J. Williams, "Learning representations by back-propagating errors," *Nature,* vol. 323, no. 6088, pp. 533-536, 1986, doi: 10.1038/323533a0.

[46]   B. E. Boser, I. M. Guyon, and V. N. Vapnik, "A training algorithm for optimal margin classifiers," presented at the Proceedings of the fifth annual workshop on Computational learning theory - COLT '92, Pittsburgh, Pennsylvania, USA, 1992. [Online]. Available: https://doi.org/10.1145/130385.130401.

[47] H. Tin Kam, "Random decision forests," in *Proceedings of 3rd International Conference on Document Analysis and Recognition*, 1995, vol. 1, pp. 278-282 vol.271, doi: 10.1109/ICDAR.1995.598994.

[48] L. Breiman, "Random forests," *Machine Learning,* vol. 45, no. 1, pp. 5-32, 2001, doi: Doi 10.1023/A:1010933404324.

[49] D. C. Ciresan, U. Meier, J. Masci, L. M. Gambardella, and J. Schmidhuber, "Flexible, high performance convolutional neural networks for image classification," in *Twenty-second international joint conference on artificial intelligence*, 2011.

[50] A. Krizhevsky, I. Sutskever, and G. E. Hinton, "Imagenet classification with deep convolutional neural networks," *Advances in Neural Information Processing Systems,* vol. 25, pp. 1097-1105, 2012.

[51] M. H. Galea, R. W. Blamey, C. E. Elston, and I. O. Ellis, "The Nottingham Prognostic Index in primary breast cancer," *Breast Cancer Research and Treatment,* vol. 22, no. 3, pp. 207-219, 1992, doi: 10.1007/BF01840834.

[52] D. F. Gleason, "Classification of prostatic carcinomas," *Cancer Chemotherapy Reports. Part 1,* vol. 50, no. 3, pp. 125-128, 1966. [Online]. Available: https://www.ncbi.nlm.nih.gov/pubmed/5948714.

[53] C. W. Elston and I. O. Ellis, "Pathological prognostic factors in breast cancer. I. The value of histological grade in breast cancer: experience from a large study with long-term follow-up," *Histopathology,* vol. 19, no. 5, pp. 403-410, 1991, doi: 10.1111/j.1365-2559.1991.tb00229.x.

[54] S. Petushi, F. U. Garcia, M. M. Haber, C. Katsinis, and A. Tozeren, "Large-scale computations on histology images reveal grade-differentiating parameters for breast cancer," *BMC Medical Imaging,* vol. 6, p. 14, 2006, doi: 10.1186/1471-2342-6-14.

[55] T. M. Cover, "Geometrical and Statistical Properties of Systems of Linear Inequalities with Applications in Pattern Recognition," *IEEE Transactions on Electronic Computers,* vol. EC-14, no. 3, pp. 326-334, 1965, doi: 10.1109/pgec.1965.264137.

[56] S. Doyle, S. Agner, A. Madabhushi, M. Feldman, and J. Tomaszewski, "Automated grading of breast cancer histopathology using spectral clustering with textural and architectural image features," in *2008 5th IEEE International Symposium on Biomedical Imaging: From Nano to Macro*, 2008, pp. 496-499, doi: 10.1109/ISBI.2008.4541041.

[57] I. Fogel and D. Sagi, "Gabor filters as texture discriminator," *Biological Cybernetics,* vol. 61, no. 2, pp. 103-113, 1989, doi: 10.1007/bf00204594.

[58]   R. M. Haralick, "Statistical and structural approaches to texture," *Proceedings of the IEEE,* vol. 67, no. 5, pp. 786-804, 1979, doi: 10.1109/proc.1979.11328.

[59]   F. Aurenhammer, "Voronoi Diagrams - a Survey of a Fundamental Geometric Data Structure," *Computing Surveys,* vol. 23, no. 3, pp. 345-405, 1991, doi: 10.1145/116873.116880.

[60]   D. T. Lee and B. J. Schachter, "Two algorithms for constructing a Delaunay triangulation," *International Journal of Computer & Information Sciences,* vol. 9, no. 3, pp. 219-242, 1980, doi: 10.1007/bf00977785.

[61]   J. B. Kruskal, "On the shortest spanning subtree of a graph and the traveling salesman problem," *Proceedings of the American Mathematical society,* vol. 7, no. 1, pp. 48-50, 1956.

[62]   J. Dalle, W. K. Leow, D. Racoceanu, A. E. Tutac, and T. C. Putti, "Automatic breast cancer grading of histopathological images," in *2008 30th Annual International Conference of the IEEE Engineering in Medicine and Biology Society*, 2008, pp. 3052-3055, doi: 10.1109/IEMBS.2008.4649847.

[63]   M. Karaman, L. Goldmann, and T. Sikora, *A new segmentation approach using Gaussian color model and temporal information* (Electronic Imaging 2006). SPIE, 2006.

[64]   S. Naik, S. Doyle, M. Feldman, J. Tomaszewski, and A. Madabhushi, "Gland segmentation and computerized gleason grading of prostate histology by integrating low-, high-level and domain specific information," in *MIAAB workshop*, pp. 1-8, 2007.

[65]   N. Friedman, D. Geiger, and M. Goldszmidt, "Bayesian network classifiers," *Machine Learning,* vol. 29, no. 2-3, pp. 131-163, 1997, doi: Doi 10.1023/A:1007465528199.

[66]   P. Bankhead *et al.*, "QuPath: Open source software for digital pathology image analysis," *Scientific Reports,* vol. 7, no. 1, p. 16878, 2017, doi: 10.1038/s41598-017-17204-5.

[67]   P. Bankhead *et al.*, "Integrated tumor identification and automated scoring minimizes pathologist involvement and provides new insights to key biomarkers in breast cancer," *Laboratory Investigation,* vol. 98, no. 1, pp. 15-26, 2018, doi: 10.1038/labinvest.2017.131.

[68]   H. Irshad, A. Veillard, L. Roux, and D. Racoceanu, "Methods for nuclei detection, segmentation, and classification in digital histopathology: a review-current status and future potential," *IEEE Reviews in Biomedical Engineering,* vol. 7, pp. 97-114, 2014, doi: 10.1109/RBME.2013.2295804.

[69]   J. B. T. M. Roerdink and A. Meijster, "The Watershed Transform: Definitions, Algorithms and Parallelization Strategies," *Fundamenta*

Informaticae, vol. 41, no. 1,2, pp. 187-228, 2000, doi: 10.3233/fi-2000-411207.

[70] J. Canny, "A computational approach to edge detection," *IEEE Trans Pattern Anal Mach Intell,* vol. 8, no. 6, pp. 679-698, 1986, doi: 10.1109/TPAMI.1986.4767851.

[71] R. O. Duda and P. E. Hart, "Use of the Hough transformation to detect lines and curves in pictures," *Communications of the ACM,* vol. 15, no. 1, pp. 11-15, 1972, doi: 10.1145/361237.361242.

[72] Y. Wang, Q. Guo, and Y. Zhu, "Medical Image Segmentation Based On Deformable Models And Its Applications," in *Deformable Models: Theory and Biomaterial Applications*, J. S. Suri and A. A. Farag Eds. New York, NY: Springer New York, pp. 209-260, 2007.

[73] M. A. Guevara, A. Silva, H. Oliveira, M. de Lourdes Pereira, and F. Morgado, "Segmentation and Morphometry of Histological Sections Using Deformable Models: A New Tool for Evaluating Testicular Histopathology," in *Progress in Pattern Recognition, Speech and Image Analysis*, Berlin, Heidelberg, A. Sanfeliu and J. Ruiz-Shulcloper, Eds., Springer Berlin Heidelberg, pp. 282-290, 2003.

[74] Y. L. Li and Y. Shen, "Fuzzy c-means clustering based on spatial neighborhood information for image segmentation," *Journal of Systems Engineering and Electronics,* vol. 21, no. 2, pp. 323-328, 2010, doi: 10.3969/j.issn.1004-4132.2010.02.024.

[75] X. Xu *et al.*, "Automated Brain Region Segmentation for Single Cell Resolution Histological Images Based on Markov Random Field," *Neuroinformatics,* vol. 18, no. 2, pp. 181-197, 2020, doi: 10.1007/s12021-019-09432-z.

[76] R. Azmi and N. Norozi, "A New Markov Random Field Segmentation Method for Breast Lesion Segmentation in MR images," *J Med Signals Sens,* Article vol. 1, no. 3, pp. 156-164, 2011, doi: 10.4103/2228-7477.95284.

[77] J. Xu, J. P. Monaco, R. Sparks, and A. Madabhushi, "Connecting Markov random fields and active contour models: application to gland segmentation and classification," *J Med Imaging (Bellingham),* vol. 4, no. 2, p. 021107, 2017, doi: 10.1117/1.JMI.4.2.021107.

[78] A. B. Ashraf, S. C. Gavenonis, D. Daye, C. Mies, M. A. Rosen, and D. Kontos, "A multichannel Markov random field framework for tumor segmentation with an application to classification of gene expression-based breast cancer recurrence risk," *IEEE Transactions on Medical Imaging,* vol. 32, no. 4, pp. 637-648, 2013, doi: 10.1109/TMI.2012.2219589.

[79] H. Erfankhah, M. Yazdi, M. Babaie, and H. R. Tizhoosh, "Heterogeneity-Aware Local Binary Patterns for Retrieval of

Histopathology Images," *IEEE Access,* vol. 7, pp. 18354-18367, 2019, doi: 10.1109/access.2019.2897281.

[80] R. Alomari, S. Ghosh, V. Chaudhary, and O. Al-Kadi, *Local binary patterns for stromal area removal in histology images* (SPIE Medical Imaging). SPIE, 2012.

[81] R. Peyret, A. Bouridane, F. Khelifi, M. A. Tahir, and S. Al-Maadeed, "Automatic classification of colorectal and prostatic histologic tumor images using multiscale multispectral local binary pattern texture features and stacked generalization," *Neurocomputing,* vol. 275, pp. 83-93, Jan 2018, doi: 10.1016/j.neucom.2017.05.010.

[82] Rahmadwati, G. Naghdy, M. Ros, C. Todd, and E. Norahmawati, "Cervical Cancer Classification Using Gabor Filters," in *2011 IEEE First International Conference on Healthcare Informatics, Imaging and Systems Biology*, 2011, pp. 48-52, doi: 10.1109/HISB.2011.15.

[83] O. S. Al-Kadi, "A gabor filter texture analysis approach for histopathological brain tumor subtype discrimination," *arXiv preprint arXiv:1704.05122,* 2017.

[84] G. Lu *et al.*, "Histopathology Feature Mining and Association with Hyperspectral Imaging for the Detection of Squamous Neoplasia," *Scientific Reports,* vol. 9, no. 1, p. 17863, 2019, doi: 10.1038/s41598-019-54139-5.

[85] J. Diamond, N. H. Anderson, P. H. Bartels, R. Montironi, and P. W. Hamilton, "The use of morphological characteristics and texture analysis in the identification of tissue composition in prostatic neoplasia," *Human Pathology,* vol. 35, no. 9, pp. 1121-1131, 2004, doi: 10.1016/j.humpath.2004.05.010.

[86] L. He, L. R. Long, S. Antani, and G. R. Thoma, "Histology image analysis for carcinoma detection and grading," *Computer Methods and Programs in Biomedicine,* vol. 107, no. 3, pp. 538-556, 2012, doi: 10.1016/j.cmpb.2011.12.007.

[87] A. D. Belsare, M. M. Mushrif, M. A. Pangarkar, and N. Meshram, "Breast histopathology image segmentation using spatio-colour-texture based graph partition method," *Journal of Microscopy,* vol. 262, no. 3, pp. 260-273, 2016, doi: 10.1111/jmi.12361.

[88] J. Galaro, A. R. Judkins, D. Ellison, J. Baccon, and A. Madabhushi, "An integrated texton and bag of words classifier for identifying anaplastic medulloblastomas," in *2011 Annual International Conference of the IEEE Engineering in Medicine and Biology Society*, 2011, pp. 3443-3446, doi: 10.1109/IEMBS.2011.6090931.

[89] Y. Zhou, H. Chang, K. Barner, P. Spellman, and B. Parvin, "Classification of Histology Sections via Multispectral Convolutional Sparse Coding," *Conf Comput Vis Pattern Recognit*

Workshops, vol. 2014, pp. 3081-3088, 2014, doi: 10.1109/CVPR.2014.394.

[90]   L. Shamir, N. Orlov, D. M. Eckley, T. Macura, J. Johnston, and I. G. Goldberg, "Wndchrm - an open source utility for biological image analysis," *Source Code for Biology and Medicine,* vol. 3, no. 1, p. 13, 2008, doi: 10.1186/1751-0473-3-13.

[91]   A. Sethi *et al.*, "Empirical comparison of color normalization methods for epithelial-stromal classification in H and E images," *Journal of Pathology Informatics,* Research Article vol. 7, no. 1, p. 17, 2016, doi: 10.4103/2153-3539.179984.

[92]   B. Ehteshami Bejnordi *et al.*, "Automated Detection of DCIS in Whole-Slide H&E Stained Breast Histopathology Images," *IEEE Transactions on Medical Imaging,* vol. 35, no. 9, pp. 2141-2150, 2016, doi: 10.1109/TMI.2016.2550620.

[93]   Y. Huang, H. Zheng, C. Liu, X. Ding, and G. K. Rohde, "Epithelium-Stroma Classification via Convolutional Neural Networks and Unsupervised Domain Adaptation in Histopathological Images," *IEEE journal of biomedical and health informatics,* vol. 21, no. 6, pp. 1625-1632, 2017, doi: 10.1109/JBHI.2017.2691738.

[94]   G. Litjens *et al.*, "Deep learning as a tool for increased accuracy and efficiency of histopathological diagnosis," *Scientific Reports,* vol. 6, no. 1, p. 26286, 2016, doi: 10.1038/srep26286.

[95]   J. Xu, X. Luo, G. Wang, H. Gilmore, and A. Madabhushi, "A Deep Convolutional Neural Network for segmenting and classifying epithelial and stromal regions in histopathological images," *Neurocomputing,* vol. 191, pp. 214-223, 2016, doi: 10.1016/j.neucom.2016.01.034.

[96]   Y. Song, L. Zhang, S. Chen, D. Ni, B. Lei, and T. Wang, "Accurate Segmentation of Cervical Cytoplasm and Nuclei Based on Multiscale Convolutional Network and Graph Partitioning," *IEEE Transactions on Biomedical Engineering,* vol. 62, no. 10, pp. 2421-2433, 2015, doi: 10.1109/TBME.2015.2430895.

[97]   Y. Xu *et al.*, "Large scale tissue histopathology image classification, segmentation, and visualization via deep convolutional activation features," *BMC Bioinformatics,* vol. 18, no. 1, p. 281, 2017, doi: 10.1186/s12859-017-1685-x.

[98]   J. Long, E. Shelhamer, and T. Darrell, "Fully convolutional networks for semantic segmentation," in *Proceedings of the IEEE conference on computer vision and pattern recognition*, pp. 3431-3440, 2015.

[99]   O. Ronneberger, P. Fischer, and T. Brox, "U-Net: Convolutional Networks for Biomedical Image Segmentation," in *Medical Image Computing and Computer-Assisted Intervention – MICCAI 2015*,

Cham, N. Navab, J. Hornegger, W. M. Wells, and A. F. Frangi, Eds., Springer International Publishing, pp. 234-241, 2015.

[100]   Y. Xu *et al.*, "Gland Instance Segmentation Using Deep Multichannel Neural Networks," *IEEE Transactions on Biomedical Engineering,* vol. 64, no. 12, pp. 2901-2912, 2017, doi: 10.1109/TBME.2017.2686418.

[101]   L. Bi, J. Kim, A. Kumar, M. Fulham, and D. G. Feng, "Stacked fully convolutional networks with multi-channel learning: application to medical image segmentation," *Visual Computer,* vol. 33, no. 6-8, pp. 1061-1071, 2017, doi: 10.1007/s00371-017-1379-4.

[102]   B. Gecer, S. Aksoy, E. Mercan, L. G. Shapiro, D. L. Weaver, and J. G. Elmore, "Detection and classification of cancer in whole slide breast histopathology images using deep convolutional networks," *Pattern Recognition,* vol. 84, pp. 345-356, 2018, doi: 10.1016/j.patcog.2018.07.022.

[103]   R. R. Rawat, D. Ruderman, P. Macklin, D. L. Rimm, and D. B. Agus, "Correlating nuclear morphometric patterns with estrogen receptor status in breast cancer pathologic specimens," *NPJ Breast Cancer,* vol. 4, p. 32, 2018, doi: 10.1038/s41523-018-0084-4.

[104]   S. E. A. Raza *et al.*, "Micro-Net: A unified model for segmentation of various objects in microscopy images," *Medical Image Analysis,* vol. 52, pp. 160-173, 2019, doi: 10.1016/j.media.2018.12.003.

[105]   P. Bandi, M. Balkenhol, B. van Ginneken, J. van der Laak, and G. Litjens, "Resolution-agnostic tissue segmentation in whole-slide histopathology images with convolutional neural networks," *PeerJ,* vol. 7, p. e8242, 2019, doi: 10.7717/peerj.8242.

[106]   J. T. Pontalba, T. Gwynne-Timothy, E. David, K. Jakate, D. Androutsos, and A. Khademi, "Assessing the Impact of Color Normalization in Convolutional Neural Network-Based Nuclei Segmentation Frameworks," *Frontiers in bioengineering and biotechnology,* vol. 7, p. 300, 2019, doi: 10.3389/fbioe.2019.00300.

[107]   J. C. Caicedo *et al.*, "Nucleus segmentation across imaging experiments: the 2018 Data Science Bowl," *Nature Methods,* vol. 16, no. 12, pp. 1247-1253, 2019, doi: 10.1038/s41592-019-0612-7.

[108]   Z. Zhou, M. M. R. Siddiquee, N. Tajbakhsh, and J. Liang, "UNet++: Redesigning Skip Connections to Exploit Multiscale Features in Image Segmentation," *IEEE Transactions on Medical Imaging,* vol. 39, no. 6, pp. 1856-1867, 2020, doi: 10.1109/TMI.2019.2959609.

[109]   G. Huang, Z. Liu, L. V. D. Maaten, and K. Q. Weinberger, "Densely Connected Convolutional Networks," in *2017 IEEE Conference on Computer Vision and Pattern Recognition (CVPR)*, pp. 2261-2269, 2017, doi: 10.1109/CVPR.2017.243.

[110]   R. Girshick, J. Donahue, T. Darrell, and J. Malik, "Rich Feature Hierarchies for Accurate Object Detection and Semantic

123

Segmentation," in *2014 IEEE Conference on Computer Vision and Pattern Recognition*, pp. 580-587, 2014, doi: 10.1109/CVPR.2014.81.

[111]   Y. Z. Ding, Q. Y. Tao, L. H. Wang, D. X. Li, and M. Zhang, "Image-based localisation using shared-information double stream hourglass networks," *Electronics Letters,* vol. 54, no. 8, pp. 496-497, 2018, doi: 10.1049/el.2017.3205.

[112]   S. Ren, K. He, R. Girshick, and J. Sun, "Faster R-CNN: Towards Real-Time Object Detection with Region Proposal Networks," *IEEE transactions on pattern analysis and machine intelligence,* vol. 39, no. 6, pp. 1137-1149, 2017, doi: 10.1109/TPAMI.2016.2577031.

[113]   K. He, G. Gkioxari, P. Dollár, and R. Girshick, "Mask R-CNN," in *2017 IEEE International Conference on Computer Vision (ICCV)*, pp. 2980-2988, 2017, doi: 10.1109/ICCV.2017.322.

[114]   M. Sebai, X. Wang, and T. Wang, "MaskMitosis: a deep learning framework for fully supervised, weakly supervised, and unsupervised mitosis detection in histopathology images," *Medical and Biological Engineering and Computing,* vol. 58, no. 7, pp. 1603-1623, 2020, doi: 10.1007/s11517-020-02175-z.

[115]   S. Yousefi and Y. Nie, "Transfer Learning from Nucleus Detection to Classification in Histopathology Images," *2019 IEEE 16th International Symposium on Biomedical Imaging (Isbi 2019),* pp. 957-960, 2019, doi: 10.1101/530113.

[116]   A. Nugaliyadde *et al.*, "RCNN for Region of Interest Detection in Whole Slide Images," in *Neural Information Processing*, Cham, H. Yang, K. Pasupa, A. C.-S. Leung, J. T. Kwok, J. H. Chan, and I. King, Eds., Springer International Publishing, pp. 625-632, 2020.

[117]   P. F. Felzenszwalb and D. P. Huttenlocher, "Efficient graph-based image segmentation," *International Journal of Computer Vision,* vol. 59, no. 2, pp. 167-181, 2004, doi: 10.1023/B:Visi.0000022288.19776.77.

[118]   A. Momeni, M. Thibault, and O. Gevaert, "Deep Recurrent Attention Models for Histopathological Image Analysis," *bioRxiv,* p. 438341, 2018, doi: 10.1101/438341.

[119]   R. Awan and N. Rajpoot, "Deep Autoencoder Features for Registration of Histology Images," in *Medical Image Understanding and Analysis*, Cham, M. Nixon, S. Mahmoodi, and R. Zwiggelaar, Eds., Springer International Publishing, pp. 371-378, 2008.

[120]   L. Hou *et al.*, "Sparse Autoencoder for Unsupervised Nucleus Detection and Representation in Histopathology Images," *Pattern Recognition,* vol. 86, pp. 188-200, 2019, doi: 10.1016/j.patcog.2018.09.007.

[121]   X. Y. Li, M. Radulovic, K. Kanjer, and K. N. Plataniotis, "Discriminative Pattern Mining for Breast Cancer Histopathology

Image Classification via Fully Convolutional Autoencoder," *IEEE Access,* vol. 7, pp. 36433-36445, 2019, doi: 10.1109/Access.2019.2904245.

[122]   Y. Feng, L. Zhang, and J. Mo, "Deep Manifold Preserving Autoencoder for Classifying Breast Cancer Histopathological Images," *IEEE/ACM Transactions on Computational Biology and Bioinformatics,* vol. 17, no. 1, pp. 91-101, 2020, doi: 10.1109/TCBB.2018.2858763.

[123]   Y. W. Jin, S. Jia, A. B. Ashraf, and P. Hu, "Integrative Data Augmentation with U-Net Segmentation Masks Improves Detection of Lymph Node Metastases in Breast Cancer Patients," *Cancers,* vol. 12, no. 10, p. 2934, 2020, doi: 10.3390/cancers12102934.

[124]   M. T. Shaban, C. Baur, N. Navab, and S. Albarqouni, "Staingan: Stain Style Transfer for Digital Histological Images," in *2019 IEEE 16th International Symposium on Biomedical Imaging (ISBI 2019)*, pp. 953-956, 2019, doi: 10.1109/ISBI.2019.8759152.

[125]   J. Wei *et al.*, "Generative Image Translation for Data Augmentation in Colorectal Histopathology Images," *Proceedings of machine learning research,* vol. 116, pp. 10-24, 2019. [Online]. Available: https://www.ncbi.nlm.nih.gov/pubmed/33912842.

[126]   Y. R. Van Eycke, A. Foucart, and C. Decaestecker, "Strategies to Reduce the Expert Supervision Required for Deep Learning-Based Segmentation of Histopathological Images," *Frontiers in Medicine,* vol. 6, p. 222, 2019, doi: 10.3389/fmed.2019.00222.

[127]   M. E. Tschuchnig, G. J. Oostingh, and M. Gadermayr, "Generative Adversarial Networks in Digital Pathology: A Survey on Trends and Future Potential," *Patterns (N Y),* vol. 1, no. 6, p. 100089, 2020, doi: 10.1016/j.patter.2020.100089.

[128]   S. Mannor, D. Peleg, and R. Rubinstein, "The cross entropy method for classification," presented at the Proceedings of the 22nd international conference on Machine learning - ICML '05, Bonn, Germany, 2005. [Online]. Available: https://doi.org/10.1145/1102351.1102422.

[129]   T. Y. Lin, P. Goyal, R. Girshick, K. He, and P. Dollar, "Focal Loss for Dense Object Detection," *IEEE transactions on pattern analysis and machine intelligence,* vol. 42, no. 2, pp. 318-327, 2017, doi: 10.1109/TPAMI.2018.2858826.

[130]   H. Li, X. Liu, S. Boumaraf, X. Gong, D. Liao, and X. Ma, "Deep Distance Map Regression Network with Shape-Aware Loss for Imbalanced Medical Image Segmentation," Cham, Springer International Publishing, in Machine Learning in Medical Imaging, pp. 231-240, 2020.

[131]   J. Clough, N. Byrne, I. Oksuz, V. A. Zimmer, J. A. Schnabel, and A. King, "A Topological Loss Function for Deep-Learning based

Image Segmentation using Persistent Homology," *IEEE transactions on pattern analysis and machine intelligence,* vol. PP, p. 1, 2020, doi: 10.1109/TPAMI.2020.3013679.

[132]   F. Caliva, C. Iriondo, A. M. Martinez, S. Majumdar, and V. Pedoia, "Distance map loss penalty term for semantic segmentation," *arXiv preprint arXiv:1908.03679,* 2019.

[133]   H. Kvamme, O. Borgan, and I. Scheel, "Time-to-Event Prediction with Neural Networks and Cox Regression," *Journal of Machine Learning Research,* vol. 20, 2019. [Online]. Available: https://jmlr.org/papers/volume20/18-424/18-424.pdf.

[134]   N. Ing *et al.*, "A novel machine learning approach reveals latent vascular phenotypes predictive of renal cancer outcome," *Scientific Reports,* vol. 7, no. 1, p. 13190, 2017, doi: 10.1038/s41598-017-13196-4.

[135]   F. Yi *et al.*, "Microvessel prediction in H&E Stained Pathology Images using fully convolutional neural networks," *BMC Bioinformatics,* vol. 19, no. 1, p. 64, 2018, doi: 10.1186/s12859-018-2055-z.

[136]   L. R. Heij *et al.*, "Nerve Fibers in the Tumor Microenvironment Are Co-Localized with Lymphoid Aggregates in Pancreatic Cancer," *Journal of Clinical Medicine,* vol. 10, no. 3, p. 490, 2021, doi: 10.3390/jcm10030490.

[137]   G. L. Beatty and W. L. Gladney, "Immune escape mechanisms as a guide for cancer immunotherapy," *Clinical Cancer Research,* vol. 21, no. 4, pp. 687-692, 2015, doi: 10.1158/1078-0432.CCR-14-1860.

[138]   R. Zappasodi, T. Merghoub, and J. D. Wolchok, "Emerging Concepts for Immune Checkpoint Blockade-Based Combination Therapies," *Cancer Cell,* vol. 33, no. 4, pp. 581-598, 2018, doi: 10.1016/j.ccell.2018.03.005.

[139]   J. McLaughlin *et al.*, "Quantitative Assessment of the Heterogeneity of PD-L1 Expression in Non-Small-Cell Lung Cancer," *JAMA Oncology,* vol. 2, no. 1, pp. 46-54, 2016, doi: 10.1001/jamaoncol.2015.3638.

[140]   M. R. Dunne *et al.*, "HLA-DR expression in tumor epithelium is an independent prognostic indicator in esophageal adenocarcinoma patients," *Cancer Immunology, Immunotherapy,* vol. 66, no. 7, pp. 841-850, 2017, doi: 10.1007/s00262-017-1983-1.

[141]   H. Panayiotou *et al.*, "The prognostic significance of tumour-stroma ratio in endometrial carcinoma," *BMC Cancer,* vol. 15, no. 1, p. 955, 2015, doi: 10.1186/s12885-015-1981-7.

[142]   L. A. Emens, "Breast Cancer Immunotherapy: Facts and Hopes," *Clinical Cancer Research,* vol. 24, no. 3, pp. 511-520, 2018, doi: 10.1158/1078-0432.CCR-16-3001.

[143]   H. Ahammer, J. M. Kropfl, C. Hackl, and R. Sedivy, "Image statistics and data mining of anal intraepithelial neoplasia," *Pattern Recognition Letters,* vol. 29, no. 16, pp. 2189-2196, 2008, doi: 10.1016/j.patrec.2008.08.008.

[144]   N. Linder *et al.*, "Identification of tumor epithelium and stroma in tissue microarrays using texture analysis," *Diagnostic Pathology,* vol. 7, no. 1, p. 22, 2012, doi: 10.1186/1746-1596-7-22.

[145]   F. Bianconi, A. Alvarez-Larran, and A. Fernandez, "Discrimination between tumour epithelium and stroma via perception-based features," *Neurocomputing,* vol. 154, no. C, pp. 119-126, 2015, doi: 10.1016/j.neucom.2014.12.012.

[146]   F. Bunyak, A. Hafiane, Z. Al-Milaji, I. Ersoy, A. Haridas, and K. Palaniappan, "A segmentation-based multi-scale framework for the classification of epithelial and stromal tissues in H&E images," in *2015 IEEE International Conference on Bioinformatics and Biomedicine (BIBM)*, pp. 450-453, 2015, doi: 10.1109/BIBM.2015.7359726.

[147]   R. Nava, G. González, J. Kybic, and B. Escalante-Ramírez, "Classification of Tumor Epithelium and Stroma in Colorectal Cancer Based on Discrete Tchebichef Moments," in *Clinical Image-Based Procedures. Translational Research in Medical Imaging*, Cham, C. Oyarzun Laura *et al.*, Eds., Springer International Publishing, pp. 79-87, 2016.

[148]   N. Harder *et al.*, "Tissue Phenomics for prognostic biomarker discovery in low- and intermediate-risk prostate cancer," *Scientific Reports,* vol. 8, no. 1, p. 4470, 2018, doi: 10.1038/s41598-018-22564-7.

[149]   A. Rasmusson *et al.*, "Immunogradient Indicators for Antitumor Response Assessment by Automated Tumor-Stroma Interface Zone Detection," *American Journal of Pathology,* vol. 190, no. 6, pp. 1309-1322, 2020, doi: 10.1016/j.ajpath.2020.01.018.

[150]   J. W. Huh, J. H. Lee, and H. R. Kim, "Prognostic significance of tumor-infiltrating lymphocytes for patients with colorectal cancer," *Archives of Surgery,* vol. 147, no. 4, pp. 366-372, 2012, doi: 10.1001/archsurg.2012.35.

[151]   R. Turkki, N. Linder, P. E. Kovanen, T. Pellinen, and J. Lundin, "Antibody-supervised deep learning for quantification of tumor-infiltrating immune cells in hematoxylin and eosin stained breast cancer samples," *Journal of Pathology Informatics,* Research Article vol. 7, no. 1, p. 38, 2016, doi: 10.4103/2153-3539.189703.

[152]   N. Linder *et al.*, "Deep learning for detecting tumour-infiltrating lymphocytes in testicular germ cell tumours," *Journal of Clinical Pathology,* vol. 72, no. 2, pp. 157-164, 2019, doi: 10.1136/jclinpath-2018-205328.

[153]   K. Sirinukunwattana, S. E. Ahmed Raza, T. Yee-Wah, D. R. Snead, I. A. Cree, and N. M. Rajpoot, "Locality Sensitive Deep Learning for Detection and Classification of Nuclei in Routine Colon Cancer Histology Images," *IEEE Transactions on Medical Imaging,* vol. 35, no. 5, pp. 1196-1206, 2016, doi: 10.1109/TMI.2016.2525803.

[154]   S. Graham *et al.*, "Hover-Net: Simultaneous segmentation and classification of nuclei in multi-tissue histology images," *Medical Image Analysis,* vol. 58, p. 101563, 2019, doi: 10.1016/j.media.2019.101563.

[155]   A. Janowczyk and A. Madabhushi, "Deep learning for digital pathology image analysis: A comprehensive tutorial with selected use cases," *Journal of Pathology Informatics,* Original Article vol. 7, no. 1, p. 29, 2016, doi: 10.4103/2153-3539.186902.

[156]   M. Alom *et al.*, "Advanced Deep Convolutional Neural Network Approaches for Digital Pathology Image Analysis: a comprehensive evaluation with different use cases," *ArXiv,* vol. abs/1904.09075, 2019.

[157]   P. P. Provenzano, K. W. Eliceiri, J. M. Campbell, D. R. Inman, J. G. White, and P. J. Keely, "Collagen reorganization at the tumor-stromal interface facilitates local invasion," *BMC Medicine,* vol. 4, no. 1, p. 38, 2006, doi: 10.1186/1741-7015-4-38.

[158]   F. Fereidouni *et al.*, "Dual-mode emission and transmission microscopy for virtual histochemistry using hematoxylin- and eosin-stained tissue sections," *Biomedical Optics Express,* Article vol. 10, no. 12, pp. 6516-6530, 2019, doi: 10.1364/BOE.10.006516.

[159]   Y. Chen, Q. Yu, and C.-B. Xu, "A convenient method for quantifying collagen fibers in atherosclerotic lesions by ImageJ software," 2017.

[160]   G. Brianezi, F. Grandi, E. Bagatin, M. M. Enokihara, and H. A. Miot, "Dermal type I collagen assessment by digital image analysis," *Anais Brasileiros de Dermatologia,* vol. 90, no. 5, pp. 723-727, 2015, doi: 10.1590/abd1806-4841.20153331.

[161]   T. J. Dekker *et al.*, "Disorganised stroma determined on pre-treatment breast cancer biopsies is associated with poor response to neoadjuvant chemotherapy: Results from the NEOZOTAC trial," *Molecular Oncology,* vol. 9, no. 6, pp. 1120-1128, 2015, doi: 10.1016/j.molonc.2015.02.001.

[162]   H. Jung *et al.*, "Integration of Deep Learning and Graph Theory for Analyzing Histopathology Whole-slide Images," *2018 IEEE Applied Imagery Pattern Recognition Workshop (Aipr),* pp. 1-5, 2018.

[163]   A. Keikhosravi, B. Li, Y. Liu, M. W. Conklin, A. G. Loeffler, and K. W. Eliceiri, "Non-disruptive collagen characterization in clinical histopathology using cross-modality image synthesis,"

Communications biology, vol. 3, no. 1, p. 414, 2020, doi: 10.1038/s42003-020-01151-5.

[164]   A. Cruz-Roa *et al.*, *Automatic detection of invasive ductal carcinoma in whole slide images with convolutional neural networks* (SPIE Medical Imaging). SPIE, 2014.

[165]   Z. Jia, X. Huang, E. I. Chang, and Y. Xu, "Constrained Deep Weak Supervision for Histopathology Image Segmentation," *IEEE Transactions on Medical Imaging,* vol. 36, no. 11, pp. 2376-2388, 2017, doi: 10.1109/TMI.2017.2724070.

[166]   O. Maron and A. L. Ratan, "Multiple-instance learning for natural scene classification," in *ICML*, vol. 98, pp. 341-349, 1998.

[167]   M. Lerousseau *et al.*, "Weakly Supervised Multiple Instance Learning Histopathological Tumor Segmentation," in *Medical Image Computing and Computer Assisted Intervention – MICCAI 2020*, Cham, A. L. Martel *et al.*, Eds., Springer International Publishing, pp. 470-479, 2020.

[168]   C. Mercan, S. Aksoy, E. Mercan, L. G. Shapiro, D. L. Weaver, and J. G. Elmore, "Multi-Instance Multi-Label Learning for Multi-Class Classification of Whole Slide Breast Histopathology Images," *IEEE Transactions on Medical Imaging,* vol. 37, no. 1, pp. 316-325, 2018, doi: 10.1109/TMI.2017.2758580.

[169]   J. Li *et al.*, "A multi-resolution model for histopathology image classification and localization with multiple instance learning," *Computers in Biology and Medicine,* vol. 131, p. 104253, 2021, doi: 10.1016/j.compbiomed.2021.104253.

[170]   K. He, X. Zhang, S. Ren, and J. Sun, "Deep Residual Learning for Image Recognition," in *2016 IEEE Conference on Computer Vision and Pattern Recognition (CVPR)*, pp. 770-778, doi: 10.1109/CVPR.2016.90, 2016.

[171]   J. Deng, W. Dong, R. Socher, L. Li, L. Kai, and F.-F. Li, "ImageNet: A large-scale hierarchical image database," in *2009 IEEE Conference on Computer Vision and Pattern Recognition*, pp. 248-255, 2009, doi: 10.1109/CVPR.2009.5206848.

[172]   W. Bulten *et al.*, "Automated deep-learning system for Gleason grading of prostate cancer using biopsies: a diagnostic study," *Lancet Oncology,* vol. 21, no. 2, pp. 233-241, 2020, doi: 10.1016/S1470-2045(19)30739-9.

[173]   S. Svagzdys, V. Lesauskaite, D. Pavalkis, I. Nedzelskiene, D. Pranys, and A. Tamelis, "Microvessel density as new prognostic marker after radiotherapy in rectal cancer," *BMC Cancer,* vol. 9, no. 1, p. 95, 2009, doi: 10.1186/1471-2407-9-95.

[174]   A. Laurinavicius, A. Laurinaviciene, V. Ostapenko, D. Dasevicius, S. Jarmalaite, and J. Lazutka, "Immunohistochemistry profiles of breast ductal carcinoma: factor analysis of digital image analysis

data," *Diagnostic Pathology,* vol. 7, no. 1, p. 27, 2012, doi: 10.1186/1746-1596-7-27.

[175] A. Laurinaviciene *et al.*, "Digital immunohistochemistry platform for the staining variation monitoring based on integration of image and statistical analyses with laboratory information system," *Diagnostic Pathology,* vol. 9 Suppl 1, no. 1, p. S10, 2014, doi: 10.1186/1746-1596-9-S1-S10.

[176] A. Laurinavicius *et al.*, "Ki67/SATB1 ratio is an independent prognostic factor of overall survival in patients with early hormone receptor-positive invasive ductal breast carcinoma," *Oncotarget,* vol. 6, no. 38, pp. 41134-41145, 2015, doi: 10.18632/oncotarget.5838.

[177] B. Plancoulaine *et al.*, "Digital immunohistochemistry wizard: image analysis-assisted stereology tool to produce reference data set for calibration and quality control," *Diagnostic Pathology,* vol. 9 Suppl 1, no. 1, p. S8, 2014, doi: 10.1186/1746-1596-9-S1-S8.

[178] A. Kriščiukaitis *et al.*, "Quantitative evaluation of morphologic changes in histologic samples by means of mathematical mor-phology," in *7th International Workshop" Data analysis methods for software systems"–DAMSS: Druskininkai, Lithuania, December 3-5, 2015/Lithuanian Computer Society. Vilnius University Institute of Mathematics and Informatics. Lithuanian Academy of Sciences. Druskininkai: Vilnius University,* 2015.

[179] R. Petrolis *et al.*, "Digital imaging of colon tissue: method for evaluation of inflammation severity by spatial frequency features of the histological images," *Diagnostic Pathology,* vol. 10, no. 1, p. 159, 2015, doi: 10.1186/s13000-015-0389-7.

[180] D. Daunoravicius *et al.*, "Quantification of myocardial fibrosis by digital image analysis and interactive stereology," *Diagnostic Pathology,* vol. 9, no. 1, p. 114, 2014, doi: 10.1186/1746-1596-9-114.

[181] R. Asoklis, A. Kadziauskiene, R. Paulaviciene, D. Petroska, and A. Laurinavicius, "Quantitative histopathological assessment of ocular surface squamous neoplasia using digital image analysis," *Oncology Letters,* vol. 8, no. 4, pp. 1482-1486, 2014, doi: 10.3892/ol.2014.2366.

[182] B. Plancoulaine *et al.*, "A methodology for comprehensive breast cancer Ki67 labeling index with intra-tumor heterogeneity appraisal based on hexagonal tiling of digital image analysis data," *Virchows Archiv,* vol. 467, no. 6, pp. 711-722, 2015, doi: 10.1007/s00428-015-1865-x.

[183] J. Besusparis *et al.*, "Impact of tissue sampling on accuracy of Ki67 immunohistochemistry evaluation in breast cancer," *Diagnostic Pathology,* vol. 11, no. 1, p. 82, 2016, doi: 10.1186/s13000-016-0525-z.

[184] A. Laurinavicius *et al.*, "Bimodality of intratumor Ki67 expression is an independent prognostic factor of overall survival in patients with invasive breast carcinoma," *Virchows Archiv,* vol. 468, no. 4, pp. 493-502, 2016, doi: 10.1007/s00428-016-1907-z.

[185] R. Petrolis, R. Ramonaitė, G. Kiudelis, G. Varkalaitė, L. Kupčinskas, and A. Kriščiukaitis, "Implementation of image analysis techniques in gastric cancer cell motility analysis," in *Human and Nature Safety: Proceedings of the 22nd international scientific-practice conference" Human and nature safety 2016"*, Kaunas, Lithuania/Aleksandro Stulginskio universitetas, 2016.

[186] R. Petrolis, R. Ramonaite, D. Jocevicius, G. Kiudelis, L. Kupcinskas, and A. Kriščiukaitis, "Characterization of gastrointestinal cancer cells invasiveness by estimation of their motility," *Biomedical Engineering 2016,* vol. 20, no. 1, 2017.

[187] R. Ramonaite *et al.*, "Mathematical morphology-based imaging of gastrointestinal cancer cell motility and 5-aminolevulinic acid-induced fluorescence," *Biomedizinische Technik,* vol. 64, no. 6, pp. 711-720, 2019, doi: 10.1515/bmt-2018-0197.

[188] M. Lukashevich and V. Starovoitov, "An Approach to Cell Nuclei Counting in Histological Image Analysis," Cham, Springer International Publishing, in Computer Information Systems and Industrial Management, pp. 139-147, 2016.

[189] A. Paulauskaite-Taraseviciene, K. Sutiene, J. Valotka, V. Raudonis, and T. Iesmantas, "Deep Learning-based Detection of Overlapping Cells," presented at the Proceedings of the 2019 3rd International Conference on Advances in Artificial Intelligence, Istanbul, Turkey, 2019. [Online]. Available: https://doi.org/10.1145/3369114.3369120.

[190] D. Zilenaite *et al.*, "Independent Prognostic Value of Intratumoral Heterogeneity and Immune Response Features by Automated Digital Immunohistochemistry Analysis in Early Hormone Receptor-Positive Breast Carcinoma," *Frontiers in Oncology,* Original Research vol. 10, no. 950, p. 950, 2020, doi: 10.3389/fonc.2020.00950.

[191] A. Nestarenkaite *et al.*, "Immuno-Interface Score to Predict Outcome in Colorectal Cancer Independent of Microsatellite Instability Status," *Cancers,* vol. 12, no. 10, p. 2902, 2020, doi: 10.3390/cancers12102902.

[192] T. Fawcett, "An introduction to ROC analysis," *Pattern Recognition Letters,* vol. 27, no. 8, pp. 861-874, 2006, doi: 10.1016/j.patrec.2005.10.010.

[193] R. Achanta, A. Shaji, K. Smith, A. Lucchi, P. Fua, and S. Susstrunk, "SLIC superpixels compared to state-of-the-art superpixel methods,"

IEEE transactions on pattern analysis and machine intelligence, vol. 34, no. 11, pp. 2274-2282, 2012, doi: 10.1109/TPAMI.2012.120.

[194]   C. Kanan and G. W. Cottrell, "Color-to-grayscale: does the method matter in image recognition?," *PloS One,* vol. 7, no. 1, p. e29740, 2012, doi: 10.1371/journal.pone.0029740.

[195]   L. P. Coelho, "Mahotas: Open source software for scriptable computer vision," *arXiv preprint arXiv:1211.4907,* 2012.

[196]   I. T. Jolliffe, "Principal Component Analysis and Factor Analysis," in *Principal Component Analysis*, (Springer Series in Statistics. New York, NY: Springer New York, Chapter 7, pp. 115-128, 1986.

[197]   F. Pedregosa *et al.*, "Scikit-learn: Machine Learning in Python," *Journal of Machine Learning Research,* vol. 12, pp. 2825-2830, 2011.

[198]   M. Abadi *et al.*, "TensorFlow: Large-Scale Machine Learning on Heterogeneous Distributed Systems," *CoRR,* vol. abs/1603.04467, 2015. [Online]. Available: http://download.tensorflow.org/paper/whitepaper2015.pdf.

[199]   F. Chollet, "Keras: The python deep learning library," *Astrophysics Source Code Library,* p. ascl: 1806.1022, 2018.

[200]   C. Cortes and V. Vapnik, "Support-Vector Networks," *Machine Learning,* vol. 20, no. 3, pp. 273-297, 1995, doi: 10.1023/A:1022627411411.

[201]   Y.-W. Chang, C.-J. Hsieh, K.-W. Chang, M. Ringgaard, and C.-J. Lin, "Training and Testing Low-degree Polynomial Data Mappings via Linear SVM," *Journal of Machine Learning Research,* vol. 11, pp. 1471–1490, 2010.

[202]   C. Nwankpa, W. Ijomah, A. Gachagan, and S. Marshall, "Activation Functions: Comparison of trends in Practice and Research for Deep Learning," *ArXiv,* vol. abs/1811.03378, 2018.

[203]   R. Malouf, "A Comparison of Algorithms for Maximum Entropy Parameter Estimation," in *COLING-02: The 6th Conference on Natural Language Learning 2002 (CoNLL-2002)*, 2002.

[204]   D. P. Kingma and J. Ba, "Adam: A method for stochastic optimization," *arXiv preprint arXiv:1412.6980,* 2014.

[205]   R. L. Grossman *et al.*, "Toward a Shared Vision for Cancer Genomic Data," *New England Journal of Medicine,* vol. 375, no. 12, pp. 1109-1112, 2016, doi: 10.1056/NEJMp1607591.

[206]   K. Zuiderveld, "Contrast Limited Adaptive Histogram Equalization," in *Graphics Gems*, P. S. Heckbert Ed.: Academic Press, pp. 474-485, 1994.

[207]   A. C. Ruifrok and D. A. Johnston, "Quantification of histochemical staining by color deconvolution," *Analytical and Quantitative Cytology and Histology,* vol. 23, no. 4, pp. 291-299, 2001. [Online]. Available: https://www.ncbi.nlm.nih.gov/pubmed/11531144.

[208]   D.-A. Clevert, T. Unterthiner, and S. Hochreiter, "Fast and Accurate Deep Network Learning by Exponential Linear Units (ELUs)," 2016. [Online]. Available: http://arxiv.org/abs/1511.07289.

[209]   K. H. Zou *et al.*, "Statistical validation of image segmentation quality based on a spatial overlap index," *Academic Radiology,* vol. 11, no. 2, pp. 178-189, 2004, doi: 10.1016/s1076-6332(03)00671-8.

[210]   S. Jadon, "A survey of loss functions for semantic segmentation," in *2020 IEEE Conference on Computational Intelligence in Bioinformatics and Computational Biology (CIBCB)*, pp. 1-7, 2020, doi: 10.1109/CIBCB48159.2020.9277638.

[211]   M. Feurer, A. Klein, K. Eggensperger, J. T. Springenberg, M. Blum, and F. Hutter, "Auto-sklearn: Efficient and Robust Automated Machine Learning," in *Automated Machine Learning: Methods, Systems, Challenges*, F. Hutter, L. Kotthoff, and J. Vanschoren Eds. Cham: Springer International Publishing, pp. 113-134, 2019.

[212]   A. A. Taha and A. Hanbury, "Metrics for evaluating 3D medical image segmentation: analysis, selection, and tool," *BMC Medical Imaging,* vol. 15, p. 29, 2015, doi: 10.1186/s12880-015-0068-x.

[213]   L. Hamers *et al.*, "Similarity measures in scientometric research: The Jaccard index versus Salton's cosine formula," *Information Processing & Management,* vol. 25, no. 3, pp. 315-318, 1989, doi: 10.1016/0306-4573(89)90048-4.

[214]   E. Reinhard, N. Ashikhmin, B. Gooch, and P. Shirley, "Color transfer between images," *IEEE Computer Graphics and Applications,* vol. 21, no. 5, pp. 34-41, 2001, doi: 10.1109/38.946629.

[215]   C. R. Harris *et al.*, "Array programming with NumPy," *Nature,* vol. 585, no. 7825, pp. 357-362, 2020, doi: 10.1038/s41586-020-2649-2.

[216]   D. G. Altman and J. M. Bland, "Measurement in Medicine: The Analysis of Method Comparison Studies," *The Statistician,* vol. 32, no. 3, pp. 307-317, 1983, doi: 10.2307/2987937.

[217]   D. Giavarina, "Understanding Bland Altman analysis," *Biochemia Medica: Casopis Hrvatskoga Drustva Medicinskih Biokemicara,* vol. 25, no. 2, pp. 141-151, 2015, doi: 10.11613/BM.2015.015.

[218]   N. Dalal and B. Triggs, "Histograms of oriented gradients for human detection," in *2005 IEEE Computer Society Conference on Computer Vision and Pattern Recognition (CVPR'05)*, vol. 1, pp. 886-893, 2005, doi: 10.1109/CVPR.2005.177.

[219]   E. L. Kaplan and P. Meier, "Nonparametric estimation from incomplete observations," *Journal of the American statistical association,* vol. 53, no. 282, pp. 457-481, 1958.

[220]   F. Yan, M. Robert, and Y. Li, "Statistical methods and common problems in medical or biomedical science research," *International Journal of Physiology, Pathophysiology and Pharmacology,* vol. 9,

no. 5, pp. 157-163, 2017. [Online]. Available: https://www.ncbi.nlm.nih.gov/pubmed/29209453.

[221] B. George, S. Seals, and I. Aban, "Survival analysis and regression models," *Journal of Nuclear Cardiology,* vol. 21, no. 4, pp. 686-694, 2014, doi: 10.1007/s12350-014-9908-2.

[222] N. Kanopoulos, N. Vasanthavada, and R. L. Baker, "Design of an image edge detection filter using the Sobel operator," *IEEE Journal of Solid-State Circuits,* vol. 23, no. 2, pp. 358-367, 1988, doi: 10.1109/4.996.

[223] N. S. Nikolaidis, I. N. Nikolaidis, and C. C. Tsouros, "A Variation of the Box-Counting Algorithm Applied to Colour Images," p. arXiv:1107.2336, 2011. [Online]. Available: https://ui.adsabs.harvard.edu/abs/2011arXiv1107.2336N

[224] C. Rushing, A. Bulusu, H. I. Hurwitz, A. B. Nixon, and H. Pang, "A leave-one-out cross-validation SAS macro for the identification of markers associated with survival," *Computers in Biology and Medicine,* vol. 57, pp. 123-129, 2015, doi: 10.1016/j.compbiomed.2014.11.015.

[225] S. van der Walt *et al.*, "scikit-image: image processing in Python," *PeerJ,* vol. 2, p. e453, 2014, doi: 10.7717/peerj.453.

[226] J. Budczies *et al.*, "Cutoff Finder: a comprehensive and straightforward Web application enabling rapid biomarker cutoff optimization," *PloS One,* vol. 7, no. 12, p. e51862, 2012, doi: 10.1371/journal.pone.0051862.

[227] T. Therneau, "A Package for Survival Analysis in R. R package version 3.2-3," 2020. [Online]. Available: https://CRAN.R-project.org/package=survival.

[228] M. W. Conklin *et al.*, "Aligned collagen is a prognostic signature for survival in human breast carcinoma," *American Journal of Pathology,* vol. 178, no. 3, pp. 1221-1232, 2011, doi: 10.1016/j.ajpath.2010.11.076.

[229] J. S. Bredfeldt, Y. Liu, M. W. Conklin, P. J. Keely, T. R. Mackie, and K. W. Eliceiri, "Automated quantification of aligned collagen for human breast carcinoma prognosis," *Journal of Pathology Informatics,* Research Article vol. 5, no. 1, p. 28, 2014, doi: 10.4103/2153-3539.139707.

[230] M. W. Conklin *et al.*, "Collagen Alignment as a Predictor of Recurrence after Ductal Carcinoma In Situ," *Cancer Epidemiology, Biomarkers and Prevention,* vol. 27, no. 2, pp. 138-145, 2018, doi: 10.1158/1055-9965.EPI-17-0720.

[231] K. Esbona *et al.*, "The Presence of Cyclooxygenase 2, Tumor-Associated Macrophages, and Collagen Alignment as Prognostic Markers for Invasive Breast Carcinoma Patients," *American Journal*

of Pathology, vol. 188, no. 3, pp. 559-573, 2018, doi: 10.1016/j.ajpath.2017.10.025.

[232]   C. R. Drifka *et al.*, "Highly aligned stromal collagen is a negative prognostic factor following pancreatic ductal adenocarcinoma resection," *Oncotarget,* vol. 7, no. 46, pp. 76197-76213, 15 2016, doi: 10.18632/oncotarget.12772.

[233]   Z. H. Zhou, C. D. Ji, H. L. Xiao, H. B. Zhao, Y. H. Cui, and X. W. Bian, "Reorganized Collagen in the Tumor Microenvironment of Gastric Cancer and Its Association with Prognosis," *Journal of Cancer,* vol. 8, no. 8, pp. 1466-1476, 2017, doi: 10.7150/jca.18466.

[234]   F. Chollet, "Xception: Deep Learning with Depthwise Separable Convolutions," *30th IEEE Conference on Computer Vision and Pattern Recognition (Cvpr 2017),* pp. 1800-1807, 2017, doi: 10.1109/Cvpr.2017.195.

[235]   "The HEROHE Challenge." [Online]. Available: https://ecdp2020.grand-challenge.org/.

[236]   G. Bradski, "The OpenCV library," *Dr Dobbs Journal,* vol. 25, no. 11, p. 120, 2000.

[237]   M. Javanmardi, M. S. M. Sajjadi, T. Liu, and T. Tasdizen, "Unsupervised Total Variation Loss for Semi-supervised Deep Learning of Semantic Segmentation," *ArXiv,* vol. abs/1605.01368, 2016.

[238]   J. Kiefer and J. Wolfowitz, "Stochastic Estimation of the Maximum of a Regression Function," *The Annals of Mathematical Statistics,* vol. 23, no. 3, pp. 462-466, 1952. [Online]. Available: http://www.jstor.org/stable/2236690.

[239]   M. D. Zeiler, "Adadelta: an adaptive learning rate method," *arXiv preprint arXiv:1212.5701,* 2012.

135

ACKNOWLEDGEMENTS

AMDG

Mindaugas Morkūnas

DEVELOPMENT OF TUMOR MICROENVIRONMENT-ORIENTED DIGITAL PATHOLOGY METHODS FOR WHOLE SLIDE IMAGE SEGMENTATION AND CLASSIFICATION

DOCTORAL DISSERTATION
Technological Sciences
Informatics Engineering (T 007)
Editor Zuzana Šiušaitė

NOTES

NOTES